2019

INFLUENCE OF MICRO-NUCLEATE BOILING ON ANNULAR FLOW REGIME HEAT TRANSFER COEFFICIENT VALUES AND FLOW PARAMETERS – FOR HIGH HEAT-FLUX FLOW BOILING OF WATER

Soroush Sepahyar
Michigan Technological University, ssepahya@mtu.edu

Recommended Citation

Sepahyar, Soroush, "INFLUENCE OF MICRO-NUCLEATE BOILING ON ANNULAR FLOW REGIME HEAT TRANSFER COEFFICIENT VALUES AND FLOW PARAMETERS – FOR HIGH HEAT-FLUX FLOW BOILING OF WATER", Open Access Dissertation, Michigan Technological University, 2019.
https://doi.org/10.37099/mtu.dc.etdr/832

INFLUENCE OF MICRO-NUCLEATE BOILING ON ANNULAR FLOW REGIME HEAT TRANSFER COEFFICIENT VALUES AND FLOW PARAMETERS – FOR HIGH HEAT-FLUX FLOW BOILING OF WATER

By

Soroush Sepahyar

A DISSERTATION

Submitted in partial fulfillment of the requirements for the degree of

DOCTOR OF PHILOSOPHY

In Mechanical Engineering-Engineering Mechanics

MICHIGAN TECHNOLOGICAL UNIVERSITY

2019

This dissertation has been approved in partial fulfillment of the requirements for the Degree of DOCTOR OF PHILOSOPHY in Mechanical Engineering- Engineering Mechanics.

Department of Mechanical Engineering- Engineering Mechanics

Dissertation Advisor:	*Amitabh Narain*
Committee Member:	*Jamal Yagoobi*
Committee Member:	*Hassan Masoud*
Committee Member:	*Sunil S. Mehendale*
Committee Member:	*Radheshyam Tewari*
Committee Member:	*Ezequiel F. Medici*
Department Chair:	*William W. Predebon*

TABLE OF CONTENTS

LIST OF FIGURES

LIST OF TABLES

PREFACE

This thesis arises from the goals of a larger NSF project. My thesis's hypotheses and their experimental verification have been a part of Dr. Narain's NSF support (Grant #: CBET-1402702).

My significant and original contributions to this thesis are listed first. (i) Besides my role in leading the development (with the help of a senior design team) of the major new hardware from ground zero (including design, manufacturing, purchasing and assembling for the associated components) for this flow-loop facility, I was solely responsible for developing novel strategies associated with feedback flow-control that were needed to modify the hardware and the sensors associated with the exit plenum of the test-section. (ii) I provided sole leadership on all operational, modifications, debugging and testing aspects of the flow-loop and test-section (including changes in the hardware after its initial version was acquired with the help of a team), including data acquisition and flow-control which involved iterative development and testing of numerous LabVIEW programs. (iii) Leadership in obtaining the results, error estimates and doing post processing, modeling/interpretation work (with numerous MATLAB and execution, under guidance from Dr. Narain) that are reported in the "Results and Discussions" chapter of this thesis.

On the experimental/hardware parts of this thesis, I received enabling support from Dr. Michael T. Kivisalu (a co-author on the paper being submitted) and other valuable supports from Dr. Patcharapol Gorgitrattanagul (when he was a student), and a 5-member Team 52 (a Senior Undergraduate Design Team taking MEEM 4901/MEEM 4911 over Spring and Fall semester of 2016). On LabVIEW works, I received useful support from Dr. Jason Sommerville.

With regard to the unique modeling-experiments synthesis, I received help from Harsha Sathi (an MS student, who developed and executed the algorithm and ANSYS Fluent code – with my involvement – and produced, for Dr. Narain and this thesis, a written report as a part of a Special Topics course MEEM 5990). This work is reported in section B of Appendix-B. For helping me integrate the hypotheses and experiments with the reported modeling, I thank Dr. Narain and his works with his earlier students (Dr. Patcharapol Gorgitrattanagul and Hrishikesh Rangaprasad). A summary of these earlier works are reported (as background knowledge) and cited (which includes a forthcoming paper from that work) in Chapter 2 of this thesis. Also, as a result, the Introduction in section 1 has many verbatim passages from a published review article ([reference [10] of section 1) and forthcoming articles related to References ([8] and [11] of section 1). Also, I wish to acknowledge Dr. Narain's help in organizing and writing this thesis.

ACKNOWLEDGEMENTS

This thesis arises from the goals of a larger NSF project. First, I thank Dr. Narain's NSF support that made the reported experimental investigations possible. Next, for my own financial support, I thank MEEM for five academic years (Spring & fall) of TA support and MTU's Grad School for one Summer semester of Finishing Fellowship support.

On the experimental/hardware side, I received valuable support and guidance at MTU. For this, I wish to thank: Dr. Michael T. Kivisalu, Dr. Patcharapol Gorgitrattanagul (when he was a student), and a 5-member Team 52 (Michael Kostick, Taylor Hoensheid, John Ware, Jonah Kimmes and Jessica Hutchings who were the Senior Undergraduate Design Team for MEEM 4901/MEEM 4911). On LabVIEW related works, I wish to acknowledge help from Dr. Jason Sommerville.

With regard to the unique modeling-experiments synthesis presented here, I am indebted to the significant help I received help from Harsha Sathi (an MS student, who developed the algorithm and implemented it on ANSYS Fluent – with my involvement – as a part of a Special Topics course 5990 under Dr. Narain's guidance). For helping me integrate the hypotheses and experiments with the reported modeling, I thank Dr. Narain and his earlier students' background work reported in Chapter 2 of this thesis. The earlier students are Dr. Patcharapol Gorgitrattanagul and MS student Hrishikesh Rangaprasad. Also, I thank Dr. Narain for helping me organize and write this thesis – as well as forthcoming papers that result from it. In addition to the above, I am thankful for the support I have received from MEEM's technicians and Engineers Martin Toth, Steve Lehman and Safety supervisor Robert Page. I would also like to thanks Divya Pandya for his help on removing formatting issues on this dissertation.

I am also thankful for support of my dearest friends, Aref Majdara, Hossein Tavakoli, Ali Aghdaei, Mojtaba Bahramgiri, Avishan Arabshomali, Robert Richards, Kosar Khaksari, Mehdi Jafari, Maryam Fakhr Hoisseini, Khatereh Kashmari, Barzin Moridian, Behnam Azmoon, Aliihsan Koca, Foad Yousef, Mitch Dzikowicz, Bahram Sanaei Moghadam and Farshid Torabi.

Most importantly, I am most thankful of my beloved mother, Nahid Khanaki and beloved father Mahmood Sepahyar, my dear brothers, Sepehr Sepahyar and Soheil Sepahyar for all the support they have provided me over the years. Last but not least, I should thank for my girlfriend, Nazanin Nahrjou, for all her love and support through these years.

ABSTRACT

Analysis of results from steady and steady-in-the-mean high heat-flux (15 - 70 W/cm^2, with water as working fluid) shear driven annular flow-boiling experiments presented here - and low heat-flux (0.1- 1 W/cm^2, with FC-72 as working fluid) experiments presented elsewhere – together lead to a key conclusion. The conclusion is that heat carrying nucleation rates go often undetected by the typically used visualization approaches for flow boiling – as such flows often involve µm- to sub- µm scale bubble diameters in millimeter-scale ducts. These nucleation rates play a significant role in most of the so-called convective annular regimes (of liquid thicknesses greater than 100 microns) of flow boiling. The perspective associated with conventional classifications of nucleate and convective (plug-slug, annular, etc.) regimes are based on flow-regime classifications that depend on: (i) the larger and detected liquid-vapor interface configurations at tube diameter levels, and (ii) heat-flux dependency in heat-transfer coefficient (HTC) correlations. Various reliable syntheses of experiments with simulations and/or correlations establish, as reported here, that thin film annular regime flow boiling at high heat-flux values yield experimentally measured heat-flux or HTC values that are significantly greater (often by 80-90%) than those associated with the assumption of no nucleate boiling contributions. This leads to following the new stricter definition of convective boiling. The stricter convective flow boiling regime definition is absence or near absence of heat carrying nucleation rates. The results reported here are for experiments done in the horizontal rectangular channel of height 5 mm and width 10 mm, with the length being 14 cm in the direction of water flow. Non-zero inlet quality (between 0.4 0.7), arranged by introducing, at the inlet, separate flows of nearly saturated liquid and vapor phases – at mass flow rates consistent with imposed heat-fluxes – ensure annularity over the entire length of the horizontal boiling-surface at the bottom of the test section. Results from a separate work dealing with a newly patented breakthrough – which is referenced here – supports the basic result that significant increases in the typically undetected nucleation rates (with the help of novel approaches) can lead to significant increases in boiling HTC.

1 Introduction

In-tube boiling flows, a subset of the area of phase-change heat transfer, has been a subject of scientific studies – involving experiments, modeling, computations, and analysis – since the early 1900s. As engineering support for boiler and condenser operations in macro-scale applications (as in power generations sector, heating ventilation and air conditioning refrigeration, waste heat recovery, steam generation, etc.) have matured, new challenges have emerged in the area of high heat flux (50-1000 W/cm^2 or greater) cooling for data centers, supercomputers, laser weapons, and other devices. One of these challenges is smallness of available space for device cooling (that must employ flow-boilers). The space restrictions and low pumping power needs often limit hydraulic diameter $\mathrm{D_h}$ of the boiler/condenser tubes to be small – but not too small (e.g. 200 μm $\leq \mathrm{D_h} \leq$ 8 mm). Furthermore, safety and cost-effectiveness issues restrict pure fluids to available refrigerants and/or water.

Another challenge in addressing electronic cooling needs is a restriction on allowed boiling surface temperatures. For example, typically, 75-85 °C is the maximum allowed temperature for the boiler tube surfaces connected to cold plates used in electronic cooling (Kandlikar and Hayner 2009 [1]). Besides high heat removal capabilities at high heat-fluxes require high mass-fluxes, and this necessitates demands for improved effectiveness (ratio of heat removal rates to consumed pumping power – at duct and associated system levels) of such in-tube millimeter-scale boilers. Therefore, effectiveness often requires low pumping power consumption through manageable pressure drops – and, in case of a stack of high heat-flux flow-boilers, it may also mean an ability to recover large amounts of mechanical power available (associated with higher exiting vapor speeds from mm-scale ducts) and thermal power (available through condensation of the exiting vapor) at the exit. This means; besides flow-boiling, considerations must be given to development of suitable and innovative thermal system designs ([2]-[3]), particularly for the operations of next-generation computers, server-racks, and data centers.

Heat-exchange effectiveness also requires avoidance of vapor compressibility related choking effects (Ghiaasiaan 2007 [4]) and this, in turn, may require modest mass-fluxes

(G) in tubes of modest hydraulic diameters $D_h \equiv 4A/P_F$, where typically A and P_F respectively represent the cross-sectional area and wetted (either by liquid or vapor) perimeter of the tube. Based on available experimental studies and experiences, modest G ($\sim 10 \leq G \leq 500$ kg/m^2.s) means avoiding high G >500 kg/m^2.s and modest D_h (~ 100 μm $\leq D_h \leq$ 8 mm) means tube diameters that are neither too small (e.g., $D_h \geq$100 μm) nor too large (e.g., $D_h \leq$ 8 mm). This would mean, according to some popular naming conventions (Ghiaasiaan 2007 [4]; Kandlikar and Grande 2003 [5]; Mehendale et al. 2000 [6]), that effectiveness considerations may restrict one to mini-channels (~ 100 μm $\leq D_h \leq$ 1 mm) and a subset of macro-channels (~ 1 mm $\leq D_h \leq$ 8 mm) – excluding micro-channels (~ 10 μm $\leq D_h \leq$ 100 μm) as well as large diameter ($D_h \geq$ 8 mm) macro channels.

This thesis's focus is on steady annular flow-boiling of water in a rectangular cross-section horizontal duct (depth w = 1 cm, height h = 5 mm, and length L = 14 cm), at high heat-fluxes ($10\frac{\mathrm{W}}{\mathrm{cm}^2} \leq \bar{q}''_w \leq 80\frac{\mathrm{W}}{\mathrm{cm}^2}$) and near atmospheric pressure conditions. This is part of an effort to better understand and reinforce rather surprising results – about dominance of nucleate boiling in what is, conventionally, believed to be a convective regime – being implied by MTU group's earlier low heat-flux experiments ([7-9]) and review-based analyses of implications that follow from existing results ([10]). The other motivation to better understand the surprising new results is to contribute to the development of new flow-boiling technologies [11] and associated new thermal systems ([2]-[3]).

Standard reasons given for flow-boiling investigations is the recognition ([12]-[14]) that the current industry practices and trends with regard to heat-sinks being used in servers and server racks – which have just started shifting from air-cooled to more efficient warm-water cooled approaches ([15]-[16]) is such that it cannot keep up with exponentially rising cooling demands. And flow-boiling based heat sinks are the best candidates ([17]-[18]) for further developments that address next generation needs. This is also because more established technologies, such as an array of small diameter heat pipes or their Capillary and Looped heat pipe variations (Faghri 1995 [19]), are not appropriate solutions for the increasing high heat-flux and heat-load needs of these applications (Agostini et al. 2007 [13]; Ball 2012 [14]). *Direct use* of heat pipes do not work well because of the limitations arising from: (i) necessarily large vapor speeds involved, (ii) wicking limits that do not allow for large distances between boilers and condensers, and (iii) a need to effectively couple the new heat-sinks to the remaining parts of conventional thermal system designs.

The earlier low heat-flux investigations also showed a potential of achieving high heat-exchange efficiencies by restricting flow-boiling operations to the annular regimes ([7-9],[20-21]) and then improving the efficiencies further by superposing pulsatile operations on top of the steady ones. This thesis however limited itself to steady annular boiling alone. This is because of the earlier mentioned surprising finding ([7-10]) of the dominance of nucleate boiling in the low heat-flux annular regimes which are conventionally classified as convective. This is believed to be due to ([7-10]) the fact that invisible (below sensing capability of the instrument used) or visible nucleating bubbles and their nucleation rates (from inception to growth to departure back to inception again) play a significant role in all regimes of flow-boiling. That is, whether the regimes are plug-slug or annular and termed “convective” – or is actually the nucleate regime of flow-boiling. This is because nucleate and convective regime classifications – popular in flow-boiling literature (see [21-25])– are based on whether the respective regime-based *local* heat transfer coefficient (HTC) values/correlations *do* or *do not* exhibit a significant dependence on the values of the local heat-flux at the boiling-surface. This classification is different from the one considered and reviewed in section-2 of this thesis. Here *convective regimes* are defined to be ones for which actual contributions to the local boiling-surface heat-flux values arising from the rate at which bubbles nucleate – are negligible. This definition led us to put on hold the high heat-flux pulsatile flow-boiling investigations (for water) for thin liquid-film annular flow-regimes (involving 100 – 350 μm thin films attained by *innovative* operations [7] – where inlet quality remained above 0.4 or so). This is because earlier results [7-9] establish that more than 80% of the heat is still being carried by small, often invisible (perhaps in the range of 100 nm – 5 μm effective diameter range), nucleating bubbles. Here invisibly small means that bubble sizes are below the resolution available for direct or indirect observations – and *nucleate* and *convective regime* classifications based on image analysis approach ([26]) of presenting “nucleation site density versus distance/quality” results are less reliable and conclusive. Because of greater confidence in these newly established results ([7-9]), it is concluded that there is hardly any thin film "convective" advantages associated with operations in the annular flow-boiling regime (except in the suppressed nucleation annular regimes that are typically very thin, for most experimental conditions [7-9], about 5-40 micrometers in film thickness). With regard to investigating the dominance of nucleation rates in flow-boiling, it is further noted that there is some useful understanding and information available ([26]-[27]), particularly for pool-boiling cases, on bubble ebullition cycles for bubble-departure diameters of micrometer or larger sizes (> 1 μm if the instrument and experiment can resolve such diameters). However, for the smaller nano-meter to micro-meter ranges of bubble-diameters, the growth, departure, and collapse mechanisms – as well as heat carrying capabilities – are poorly understood [28] and likely very different. Because of the above-discussed reasons after further establishing recent findings ([7-10]), it is important to address next-generation cooling needs [11] by recognizing that nucleation rates are always important – as heat carrying mechanisms – in almost all flow boiling regimes.

Recognizing the above, this thesis's focus shifted to further establishing and *quantifying* the dominant role of nucleation rates in the steady annular boiling that was being experimentally investigated. As a part of this quantification focus, besides developing an experimental set-up and data acquisition approaches, it became necessary to analyze and relate the experimentally obtained results on local heat transfer coefficients (HTC) h_x to existing and relevant knowledge of models/correlations:

- Heat transfer coefficient h_x or its non-dimensional form termed Nusselt number Nu_x.
- Defining flow-regime maps with distance "x" or quality "X(x)" with the help of curves identifying flow-regime transitions – defined by critical values of quality X_{cr} as a function of other non-dimensional parameters characterizing the flows' realizations.
- Void-fraction ϵ and its dependence on quality X and fluid properties.
- Pressure-gradient and/or pressure-drop values.

- Obtaining different critical heat-flux (CHF) values and associated qualities X_{CHF} that are relevant to the mechanisms by which such unstable conditions arise.

Towards integrating this thesis's analyses with the above-described modeling/correlation needs, an overview is undertaken in [10] and in relevant parts of the next section.

REFERENCES

1. Kandlikar SG, Hayner CN (2009) Liquid Cooled Cold Plates for Industrial High-Power Electronic Devices—Thermal Design and Manufacturing Considerations. Heat Transfer Engineering, 30**:** 918-930.
2. Nikhil Shinde, MSME from MTU. "Innovative Fin-tubes for a Standard Staggered-bundle Family Leading to Significant Reductions in Air-side Thermal and Pressure-drop Resistances for a Popular Heat-exchanger – Quantitative Characterizations based on a Unique Synthesis of Experiments, Modeling, and Reliable Computations." (Fall 2018)
3. Amit Dev Vojini, MSME from MTU. "Innovative Fin-tubes for a Standard Staggered-bundle Family Leading to Significant Reductions in Air-side Thermal and Pressure-drop Resistances for a Popular Heat-exchanger – Modeling and Analysis in the Context of its Deployment Advantages in the Energy-sector." (Fall 2018)
4. Ghiaasiaan SM (2007). Two-phase flow, boiling, and condensation: in conventional and miniature systems. Cambridge University Press.
5. Kandlikar SG, Grande WJ (2003) Evolution of Microchannel Flow Passages--Thermohydraulic Performance and Fabrication Technology. Heat Transfer Engineering, 24: 3-17.

6. Mehendale S, Jacobi A, Shah R (2000) Fluid flow and heat transfer at micro-and meso-scales with application to heat exchanger design. Applied Mechanics Reviews, 53: 175-193.
7. Patcharapol Gorgitrattanugul, Ph.D. from MTU. “Experimental Investigation of temperature controlled innovative annular flow-boiling of FC-72 in millimeter scale ducts-steady and enhanced pulsatile realizations.” (2017).
8. Narain, A., H. Ranga Prasad, Gorgitrattanagul, P, S. Sepahyar and Mehendale, S, “Significant Role of Heat carrying Micro-scale Nucleation Rates for Steady Annular Flow boiling (Traditionally termed Convective Regime), Part I: Modeling/Simulations Support for Assessments of Experimental Data.” To be submitted.
9. Gorgitrattanagul, P., A. Narain, R. Kumar*, S.Sepahyar, and D. Pandya, “Significant Role of Heat carrying Micro-scale Nucleation Rates for Steady Annular Flow boiling (Traditionally termed Convective Regime), Part II: Experiments and Results for Low Heat-flux Operations with FC-72 as a Working Fluid.” To be submitted.
10. Narain, A., Ranga Prasad, H. and Koca, A., “Internal Annular Flow Condensation and Flow Boiling: Context, Results, and Recommendations.” In: Kulacki FA (ed.) Handbook of Thermal Science and Engineering, 2018, vol. 3, pages 2075-2162. Springer, Cham. Invited Article.
11. Narain, A. and V. Vivek (Inventors). Piezos-enhanced flow-boiling (Piezo Transducer). Provisional patent filed by Michigan Technological University. November 12, 2018. Attorney Docket #: 066040-9957-US01. The final patent being filed (support from Ahern Energy) in December 2018.
12. Avgerinou, Maria, Paolo Bertoldi, and Luca Castellazzi. "Trends in data centre energy consumption under the European code of conduct for data centre energy efficiency." *Energies* 10, no. 10 (2017): 1470.
13. Agostini B, Fabbri M, Park JE, Wojtan L, Thome JR, Michel B (2007) State of the art of high heat flux cooling technologies. Heat Transfer Engineering, 28: 258-281.
14. Ball P (2012) Computer engineering: Feeling the heat. Nature, 492: 174-176.

15. Parida, Pritish R., Milnes David, Madhusudan Iyengar, Mark Schultz, Michael Gaynes, Vinod Kamath, Bejoy Kochuparambil, and Timothy Chainer. "Experimental investigation of water cooled server microprocessors and memory devices in an energy efficient chiller-less data center." In Semiconductor Thermal Measurement and Management Symposium (SEMI-THERM), 2012 28th Annual IEEE, pp. 224-231. IEEE, 2012.
16. Campbell, Steve. “Is Liquid Cooling Ready to Go Mainstream?” URL: https://www.hpcwire.com/2017/02/13/liquid-cooling-ready-go-mainstream/
17. Lasance, C.J. and R.E. Simons, *Advances in high-performance cooling for electronics.* Electronics Cooling, 2005. **11**(4).
18. Wilson, J., *Electronics Cooling Depends on Innovative Approaches to Thermal Management.* Military & Aerospace Electronics, 2009. **3**.
19. Faghri A (1995). Heat Pipe Science and Technology. Taylor and Francis, Washington D. C.
20. Kivisalu MT (2015) Experimental investigation of certain internal condensing and boiling flows: Their sensitivity to pressure fluctuations and heat transfer enhancements. Ph. D, Michigan Technological University.
21. Kivisalu MT, Gorgitrattanagul P, Narain A (2014) Results for high heat-flux flow realizations in innovative operations of milli-meter scale condensers and boilers. International Journal of Heat and Mass Transfer, 75**:** 381-398.
22. Kim S-M, Mudawar I (2013c) Universal approach to predicting saturated flow boiling heat transfer in mini/micro-channels – Part II. Two-phase heat transfer coefficient. International Journal of Heat and Mass Transfer, 64: 1239-1256.
23. Klimenko, V. V. "A generalized correlation for two-phase forced flow heat transfer." International Journal of heat and mass transfer 31, no. 3 (1988): 541-552.
24. Kandlikar, Satish G. "A general correlation for saturated two-phase flow boiling heat transfer inside horizontal and vertical tubes." Journal of heat transfer 112, no. 1 (1990): 219-228.

25. Dorao, Carlos A., Oscar Blanco Fernandez, and Maria Fernandino. "Experimental Study of Horizontal Flow Boiling Heat Transfer of R134a at a Saturation Temperature of 18.6 C." Journal of Heat Transfer 139, no. 11 (2017): 111510.
26. Kuo, Chih-Jung, Ali Kosar, Yoav Peles, Steven Virost, Chandan Mishra, and Michael K. Jensen. “Bubble dynamics during boiling in enhanced surface microchannels.” Journal of Microelectromechanical Systems 15, no. 6 (2006): 1517-1527.
27. Mchale JP, Garimella SV (2010) Bubble nucleation characteristics in pool boiling of a wetting liquid on smooth and rough surfaces. International Journal of Multiphase Flow*,* 36 (4)**:** 249-260.
28. Agarwal, Ashutosh, Wun Jern Ng, and Yu Liu. "Principle and applications of microbubble and nanobubble technology for water treatment." Chemosphere 84, no. 9 (2011): 1175-1180.

2 Relationship to Prior MTU Research and Basic Background Knowledge

2.1 Earlier Results

The investigative answers sought here for steady high heat-flux (15 - 70 W/cm^2) annular flow boiling in millimeter-scale ducts are guided by hypotheses based on earlier results ([1]-[4]) that have been obtained for steady low heat-flux (0.1 - 1 W/cm^2) annular flow boiling in millimeter-scale ducts.

The experimental data for the earlier low heat-flux flow boiling experiments ([1]-[3]) were acquired with FC-72 as working fluid in horizontal test section (see Figure 2.1) of rectangular cross-section (Depth w = 1.5 cm, Height h = 2 mm, and Length L = 50 cm in Figure 2.1).

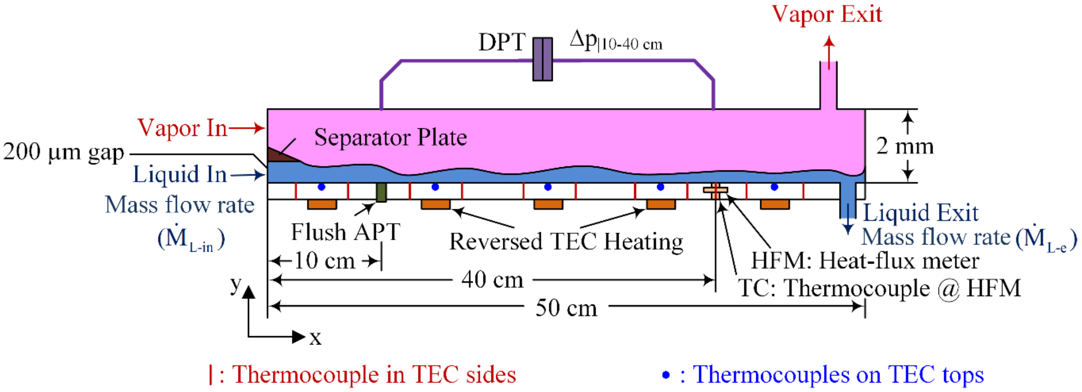

Figure 2-1 A side view schematic of an instrumented test-section that has a 15 mm width (in a direction out of the figure plane). The inlet is at x = 0 and one-dimensional flow-boiling modeling is done for the downstream flow location $0 \le x \le L$. The test-section is for low heat-flux flow boiling investigation with FC-72 as the working fluid.

The temperature controlled local heating "levels" are characterized by the local temperature difference $\Delta T(x) \equiv [T_w(x) - T_{sat}(p_0)]$, where $T_w(x)$ is the local temperature and $T_{sat}(p_0)$ is the saturation temperature at representative inlet pressure p_0. Also, let $q''_w(x)$ be the local heat-flux, Δx be the local film thickness, and fluid properties (Density ρ, Viscosity μ, Specific Heat Cp, and thermal conductivity k) be denoted with subscript "I" (I = "L" or "V" - with "L" for liquid-phase and "V" for vapor-phase). Furthermore, It is assumed that $\Delta T(x) > \Delta T|_{ONB}$ and/or $q''_w(x) > q''_w|_{ONB}$ at the location where nucleate boiling is occurring - where $\Delta T|_{ONB}$ and $q''_w|_{ONB}$ are certain lower bounds (termed ONB, Onset of Nucleate Boiling) for temperature difference $\Delta T(x)$ or heat-flux $q''_w(x)$ that cause phase change (See [5],[6]).

The local HTC h_x is defined as

$$q''_w(x) \equiv h_x . \Delta T(x) \tag{2.1}$$

The film thickness involved in this earlier investigation, as estimated by experiments-modeling synthesis [1-2], [7] were typically thin - in 50 to 100 μm range - and conditions were such that convective component of heat-flux (q''_{w-cb}) or heat transfer coefficient (HTC, $h_{x\text{-}cb}$) could be assessed. This was done by establishing the validity and quite rigorously [10] for laminar vapor and laminar liquid number of the following well known simple formula that defines to thin film convective boiling annular to conditions correspond to for which there is a near absence of significant heat transfer contributions from nucleating bubbles:

$$q''_{w-cb} = h_{x-cb} . \Delta T(x) \cong k_L . [\Delta T(x)/\Delta(x)] \tag{2.2}$$

Since turbulent vapor and laminar thin film liquid flow condition also often occur for low heat flux conditions [1-2], [7] and, this thesis's high heat flux data, Equation (2.2) remains valid. This is become (see [7]-[10]) thinnest of liquid film ensure transverse heat condition across the film followed by phase change intersection is the model of heat transfer despite enabling forward motion of the liquid and the vapor. And although the interfacial shear model can be used to provide estimates of convective HTC, to obtain estimate of film thickness $\Delta(x)$ (See [11]-[13]), this thesis presents - in later section - a simpler but reliable void-fraction model-based approach (Also see [7]) for estimating $\Delta(x)$ and $h_{x\text{-}cb}$.

For this work, we define convective boiling condition differently (denoting correct local HTC as $h_x|_{cb}$) than the classical/traditional (C/T) definition of local HTC, which is denoted as $h_x|_{cb\text{-}C/T}$. This classical/traditional definition of convective boiling and the practice of using the analogy between adiabatic annular two-phase flows (air-water type) and annular flow-boiling - for obtaining various correlation-based estimates for flow-boiling - are briefly reviewed in section 2.2 below.

Using the definition of local values of total heat flux and HTC as in Equation (2.1), in [1]-[3], experimentally measured values of local heat flux and HTC are obtained and denoted as $q''_w(x) = q''_w|_{Expt}(x)$ and $h_x = h_x|_{Expt}$. Using convective boiling to mean near absence of heat transfer contribution from nucleating bubbles and the definition in Equation (2.2), Nucleate boiling contribution (Often undetected or undetectable in most experiments) to local heat-flux and HTC, denoted as q''_{w-nb} and $h_{x\text{-}nb}$ ($\equiv q''_{w-nb}/\Delta T(x)$) respectively, are defined through the decompositions:

$$\begin{gathered} q''_w|_{Expt} \equiv q''_w|_{cb} + q''_w|_{nb} \\ h_x|_{Expt} \equiv h_x|_{cb} + h_x|_{nb} \end{gathered} \tag{2.3}$$

For experimental conditions in [1]-[3], It is found that for low heat flux thin-film annular boiling conditions, micron or submicron nucleation (likely undetectable) dominates as heat transfer mechanism in the sense that they carry away more than 90% of the heat that is:

$$q''_w|_{nb} \text{ or } h_x|_{nb} > O(0.9) \text{ of } q''_w|_{Expt} \text{ or } h_x|_{Expt} \tag{2.4}$$

The experiment results leading to Equation (2.4) are also in order of magnitude agreement with numerous correlation-based estimates [7], [12]-[15] for $h_x|_{Expt}$ and $h_x|_{cb}$ and some presented here for $h_x|_{cb}$ (under a revised definition of what is meant by the convective regime). These additional results also support the new results regarding significant dominance of Equation (2.3). These dominance results are at variance with classical decomposition based on a classical/traditional understanding of what constitutes nucleate vs. convective regimes. The classical/traditional definition are reviewed below in sub-section 2.2.1.

2.2 Basic Background Knowledge

This sub-section discusses further and critical background knowledge for better understanding of the contribution of this thesis.

2.2.1 The classical/traditional approach to the distinction between nucleate and connective regimes

The classical definition of nucleate and convective (Plug-slug, annular, etc.) regimes are based on two types of flow regime classifications that depends on: (i) The larger, contiguous, and detected (Often to naked eye) liquid-vapor interface configuration at tube diameter levels, as shown in Figure 2.2 (a); and (ii) Heat-flux dependency trends in heat transfer coefficient (HTC) results/correlations, as shown in Figure 2.3.

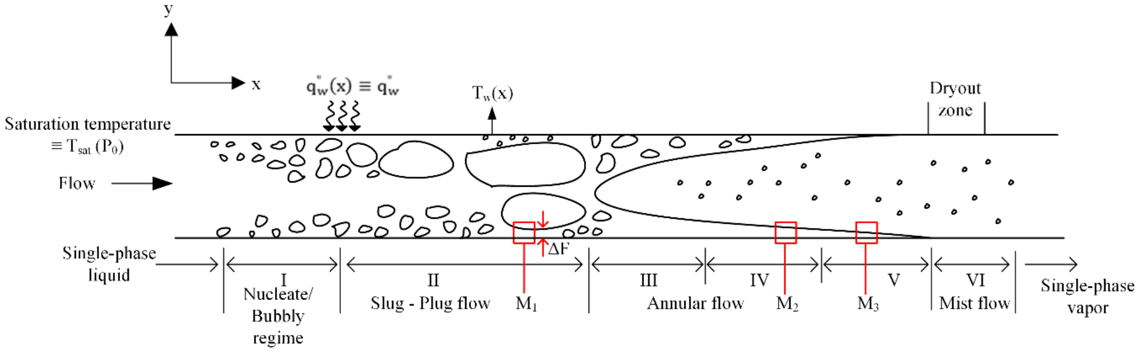

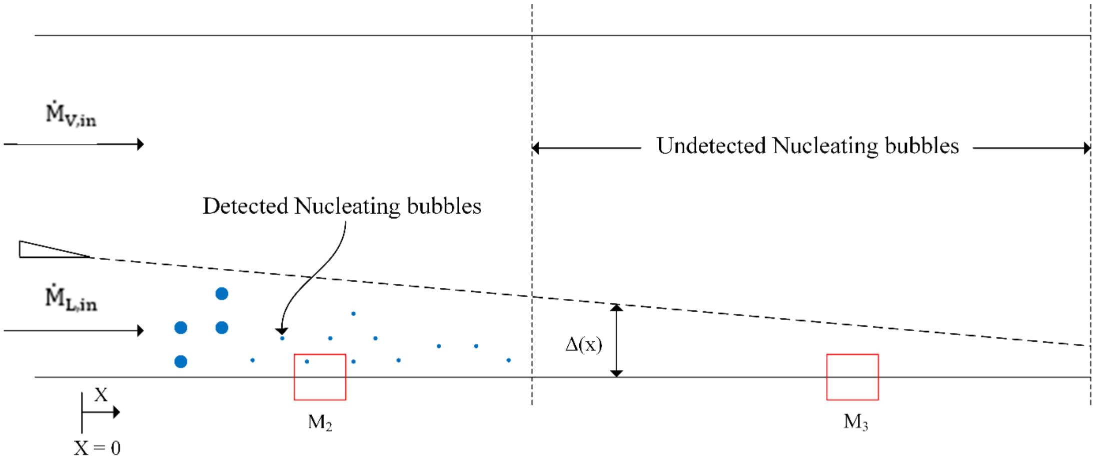

(a)

(b)

Figure 2-2 (a) Typical tube-diameter level flow-visualization resolution lead to depicted classification of flow-regimes. The illustrated case is for saturated flow-boiling in - a horizontal tube - with uniform heat-flux (q''_w) heating and given heat-flux value G (below a certain threshold) Location such as M1, M2, and M3 - underneath a vapor plug slug or in the liquid thin film region of an annular regime - indicate locations where micron to sub-micron bubbles may go undetected. **(b)** As shown, Locations such as M$_2$ and M$_3$, after sufficient magnification in suitable experiments, may or may not detect nucleating bubbles at sub-micron levels. This could be due to limitation related to visualization accuracy or available magnification or due to special and unknown ebullition cycles of nm to µm sized bubbles.

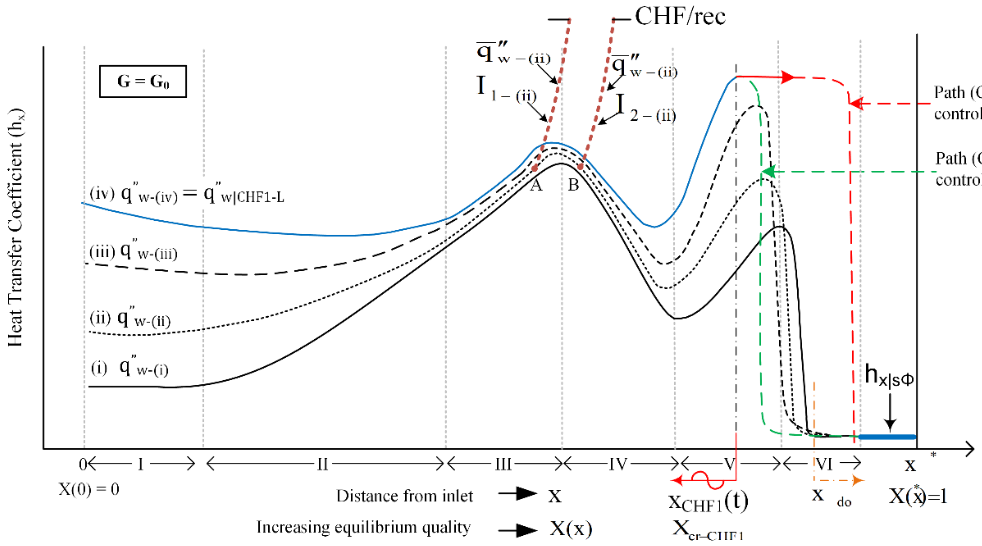

Figure 2-3 For the regimes depicted in Figure 2.2(a) and a certain means-flux G = G₀, the expected and typically observed qualitative variation in local values of HTC (h_x) with distance $0 \le X(x) \le 1$ are shown as curves (i)-(iv). These curves are increasing values of heat-flux $\bar{q}''_w$ variation within a certain interval $\bar{q}''_{w1} \le \bar{q}''_w \le \bar{q}''_{w3}$. For a representative curve (i), the flow traverses multiple flow-regime I-VI in Figure 2.2(a). Other details of the figure are discussed next and in [9].

The larger and contiguous liquid/vapor interface configuration, as observed at tube diameter resolution scale, and shown in Figure 2.2(a), define different liquid-vapor patterns/morphologies that correspond to different names (Nucleate/bubbly, Plug-Slug, annular, etc.) given to different patterns. For liquid film close to the boiling surface and in the plug-slug and annular regimes, one typically does not observe nucleating bubbles. However, in principle, if suitable magnification and flow visualization arrangements are made available. One may able to see (M_1) or may (M_2) be sub-micron to micron diameter (Say 100 nm - 10 μm) bubbles - and this is indicated in Figure 2.2(b). For various reason that limit detection of sub-micron bubbles in existing literature, the classical distinction between nucleate and convective regimes [14]-[17], with few attempted exception [23], depends on flow regimes defined in Figure 2.2(a) and heat-flux dependency trends for HTC results/correlation of the type shown in Figure 2.3. (Also see [7], [21-22]).

For the saturated flow-boiling realization in Figure 2.2, the increasing distance or quality from the inlet are also marked - see zones I-VI - on the horizontal axis of Figure 2.3. The marked zone boundaries in Figure 2.2(a) and 2.3 are for a representative curve (i) associated with specific heat-flux values $\bar{q}''_w \equiv \bar{q}''_{w-(i)}$. This curve changes to curves (ii)-(iv) for increasing values of $\bar{q}''_w$. The marked zones along the x-axis respectively denoted the following regimes: micro-scale and/or nucleate boiling (I), for which bubble sizes are detectable, by a visualization approach can resolve images up to hydraulic tube diameter (D_h) scales; plug-slug regime associated with coalesced bubbles (II); annular liquid film zone(III) associated with increasing values of local HTC h_x - a measure of increasing boiling efficiency; annular liquid film zone (IV) associated with decreasing values of local HTC h_x - perhaps after liquid film thickness goes below a certain threshold; and another very thin film annular zone (V) that suppresses nucleation - at almost all heat carrying bubbly diameter - for which hx increases with further reduction in film thicknesses because transverse conduction alone is the heat removal mechanism in the thin layer (as for Equation (2.2), except that absence of nucleation is not hypothesis); and regimes with stable liquid dry-out conditions where the boiling-surface is exposed to vapor (VI). The near inlet downstream nucleate boiling flow-regime (I) in Figure 2.2(a) consists of millimeter to sub-millimeter scale bubbles if D_h is millimeter scale. In this regime, the heat flux dependent h_x values (See [21-22], [25-26], etc.) in Figure 2.3 may increase or decrease with distance x (at a fixed $\bar{q}''_w$). The same zone (I) in Figure 2.3 has increasing values of h_x across curves - with increasing $\bar{q}''_w$ - and this is likely associated with increasing per unit ΔT_w effectiveness in removing heat through millimeter or sub-millimeter scale nucleating bubbles in tubes of millimeter-scale D_h.

However, besides zone I (the traditional nucleate boiling regime), zones II-III (the traditional convective regimes) may also have significant contribution from nucleating bubbles - though they may reach different departure diameter in different zones (mm to sub-mm in zone I, if tube-diameter is mm scale and μm to sub-μm in zones II and III) regardless of size.

Note that heat removed per bubble of departure diameter D_b (modeled as a sphere) is $\left({}^{\pi D_b^3}\!/_{6}\right).\rho_v.h_{fg}$, where $\left\{\left({}^{\pi D_b^3}\!/_{6}\right).\rho_v\right\}$ is the vaporized mass per bubble, and h_{fg} is the latent heat of vaporization (J/kg in SI). If "$n''(D_b) * dD_b$" represents the number of nucleation sites per unit area of the boiling surface associated with bubble departure diameter in the range of D_b to $D_b + dD_b$, and $f_e = f_l(D_b)$ represents the frequency associated with bubble ebullition cycles associated with bubble departure diameter D_b whose sizes are typically less than liquid film thickness Δ_F available above the nucleation site (see in Δ_F the plug-slug regimes of Figure 2.2(a) - and assign $\Delta F \cong D_h$ in zone I and $\Delta F \cong \Delta(x)$ in the annular regimes of Figure 2.2(a-b)), The heat-flux $q_w''(x)|_{nb}$ associated with nucleating bubbles in a tube of diameter D_h is given by:

$$
\begin{aligned}
q_w''(x)|_{nb} &\equiv \int_0^{\Delta F} n''(D_b).\left\{\left(\frac{\pi D_b^3}{6}\right).\rho_v\right\} h_{fg}.f(D_b).dD_b \\
&\cong \left[n_{av}''(D_b^*) * \Delta_F\right]\left\{\left(\frac{\pi D_b^3}{6}\right).\rho_v\right\} h_{fg}.f(D_b^*)
\end{aligned}
\tag{2.5}
$$

Where D_b^* defines the average bubble departure diameter through the second equality in equation (2.5). $N'' = [n_{av}''(D_b^*) * \Delta_F]$ is the representative nucleation site number per unit area at a location where liquid thickness is Δ_F ($\Delta_F \leq D_h$).

In Equation (2.5) above, $n''(D_b)$ is the spectral density function with respect to departure diameter in a statistical processing of a number of nucleation sites that correlate to departure diameter in the range of D_b to $D_b + dD_b$. However various physics issue that determine nucleation site densities include: surface profiles and cavities, wettability and spreadability of the boiling-surface except temperature $T_w(x)$ ($> \Delta T|_{ONB}$), liquid thickness Δ_F between the boiling surface and any adjacent vapor phase (e.g. see Figure 2.2(a)'s plug-slug regime), hydrodynamic and gravity forces acting on the nucleating bubble, etc. Therefore, occasionally, $n''(D_b)$ will also be denoted to highlight its dependence on many other parameters:

$$n''(D_b) = n''(D_b; \Delta T(x), \Delta_F, \text{etc.}) \quad (2.6)$$

In traditional definition of convective regimes is associated with downstream zone II-III of Figure 2.3, Where the dependency of h_x on heat flux parameter is much weaker (see relative coalescence of curves (i)-(iv) in zone III) relative to Zone I (traditionally defined to be the nucleate regime). Because pool boiling (see [27]) h_x is known to be heat-flux dependent whereas single-phase forced-convection h_x is known to be heat-flux independent ([27]) the experimentally obtained trends in Figure 2.3 and associated regimes in Figure 2.2(a) have led to the above described conventional/traditional definition of nucleate and convective regimes (see [13], [16-18], [23-25], etc.). In conventional/traditional terminologies definition, the local HTC h_x (see equation (2.1)) values are decomposed into nucleate (and denoted here as $h_x|_{nb\text{-}C/T}$) and convective (and denoted here as $h_x|_{cb\text{-}C/T}$) parts. Sometimes such decompositions are presented with a clearly defined flow-regime transient boundary (between zone I and zone II-III as shown in Figure 2.2(a) and 2.3) which is explicitly and quantitatively modeled (as in [13-14], [21], etc.) and sometimes - as in [12], [23-24] - single h_x correlation incorporates explicit correlations for the nucleate component $h_x|_{nb\text{-}C/T}$ and the convective for the nucleate component $h_x|_{cb\text{-}C/T}$ with gradually decreasing $h_x|_{nb\text{-}C/T}$ contributes with distance x (i.e. as one transverses from zone I to Zone II-III in Figures 2.2(a) and 2.3).

It should be recalled that the definition adopted by us in the sub-section 2.1, and in the paper [1-3], in this thesis redefine convective regime to correspond to conditions where there is a near absence of significant heat transfer contribution from nucleating bubbles of any size millimeter, micron, or sub-micron. And under this new definition, it is found that micron or sub-micron nucleation rates are dominant even in the so-called convective zones II and III in Figure 2.2(a) and 2.3. This conclusion stems from the fact that the rise in h_x values in zone III of Figure 2.3 - or fall in h_x values in zone IV of Figure 2.3 - both are found in several investigations ([7]-[10]) involving thin film annular flows, to be much larger in magnitude and exhibit trends (up and down) that are inconsistent with results obtained under the assumptions of heat transfer for conditions which involve negligible nucleation rates. For such condition, Equation (2.2) applies and its validity is well established (e.g. for numerous similar thin film boiling ([7], [10], etc.) and condensing ([8]-[9], etc.) flows). It should also be noted that rise and fall of HTC h_x ($\equiv q''_w(x)/\Delta T(x)$) values - which represents some sort of local heat transfer rate efficiency with respect to the temperature difference that drives the flow of heat with respect to distance "x" are related, in a special way, to the "x-dependent" trends of heat-flux $q''_w(x)$ and driving temperature difference $\Delta T_w(x)$. The rise and fall of h_x values - over any interval of distance 'x' - is governed, respectively, by positive and negative values of ${}^{dh_x}/_{dx}$ over x-interval of interest. Since $\Delta T_w(x) \geq \Delta T_w|_{ONB} > 0$, this means values of:

$$\Delta T_w(x) * {}^{dh_x}/_{dx} = \left[\frac{dq''_w(x)}{dx} - h_x.\frac{d(T_w(x))}{dx}\right] \qquad (2.7)$$

Are > 0 or < 0 over increasing or decreasing parts of an "h_x versus x" curves (see Figure 2.3).

For example, heat carrying efficiency associated with bubbles, as captured by $h_x|_{nb}$ defined in Equation (2.3) can be given (utilizing Equation (2.5)) as:

$$h_x|_{nb} \equiv \frac{1}{\Delta T_w(x)}\left[n''_{av}\left(D_b^*, \Delta T_w(x)\right).\Delta_F.\left\{\frac{\pi}{6}D_b^{*3}.\rho_v\right\}.h_{fg}.f(D_b^*)\right] \qquad (2.8)$$

Since the definitions in the Equation (2.5) cover nucleating bubbles of all sizes, in the light of the result in Equation (2.4), it is conjectured that relatively coalesced increasing h_x curves in zones II-III of Figure 2.3 correspond to increased heat carrying efficiencies associated with higher frequency (see[26]) micron and sub-micron sized nucleating bubbles associated with Δ_F or $\Delta(x)$ of plug/slug or annular regime whereas the same curves in zone I are dominated by larger and lower frequency ([26]) macro-scale nucleating bubbles. For the set of curves (i) - (iv) in Figure 2.3, as one traverses from zone I to zones II-III , the stronger to weaker dependence on heat-flux values $\bar{q}''_w$ are, therefore, not an indicator of transition to convective boiling (as the name may suggest in the classical/traditional interpretation). It is however, true that smaller liquid film thickness near the boiling-surface, in zones II-III, perhaps have a significant impact on triggering efficient micro-scale nucleation rates in a way that there is a weaker dependence on heat flux parameter $\bar{q}''_w$ - as far as separation among h_x curves (i) – (iv) in Figure 2.3 is concerned. Therefore the conventional-traditional "meaning" of $h_x|_{cb\text{-}C/T}$ ([23-25], etc.) needs to be revised/clarified in the light of the results presented in ([1-3] &[26], [1-3]) and in this thesis/paper. It is however expected that below a certain threshold liquid film-thickness $\Delta_F = \Delta(x)$, the efficient micro-nucleation becomes inefficient ─ and there is a decreasing h_x trend (zone IV in Figure 2.3). After nucleation is effectively suppressed (often for thickness less than 50 μm or so - and close to dryout point), there is a purely convective (which is also conductive from boiling surface to interface) annular zone(V) where h_x increases with distance and then rapidly falls in the dried out zone(VI).

The width of the zones IV - VI in Figure 2.3 Have been exaggerated and are somewhat uncertain – but their presence is expected and widely acknowledged ([10],[28]). Typical experimental data and their graphical presentations considered here belong to zone III and those of others ([12],[23]) cover zones I - III.

2.2.2 Typical non-dimensional correlations for local HTC h_x , interfacial shear, void fraction, and the role played by analogous results for adiabatic flows.

The nomenclature and issues associated with concepts and practices are extensively discussed in [5]. Here the definitions and nomenclatures are briefly recalled and re-written in order to better relate to new experimental/modelling results.

Let the temperature, pressure and velocity fields over the two phases ─ in the steady - in-the-mean flows depicted in the Figures 2.1-2.2 be respectively denoted as T_I, P_I and $\vec{v}_I = u_I\hat{i} + v_I\hat{j}$. Let p_0 be the mean inlet pressure (or inlet pressure at a designated inlet location), h_{fg} be the heat of vaporization at a local interfacial pressure p or associated saturation temperature T_{sat} (p), $\bar{T}_w \equiv \frac{1}{L}\int_0^L T_w(x)\,dx$ be the mean heat-exchange surface temperature associated with steady but spatially varying wall temperature $T_w(x)$. Further, let $\Delta\bar{T}[\bar{T}_w - \bar{T}_{sat}(p_0)]$ be a representative controlling temperature difference between the fluid and the heat exchanger surface, and $\dot{M}_{in}$ be the total steady mass flow rate(kg/s) through the tube. Furthermore, let $\dot{M}_{in}$ consist of liquid mass flow rate $\dot{M}_L(x)$ and vapor mass flow rate $\dot{M}_v(x)$ at any distance "x" from the inlet- i.e $\dot{M}_{in} = \dot{M}_L(x) + \dot{M}_v(x)$. Let $X(x)(\equiv \dot{M}_v(x)/ \dot{M}_{in})$ be the local quality, and G ($\equiv \dot{M}_{in}/A$) be the mass-flux (kg/m^2.s), and let the overall characteristic speed be $U(\equiv G/\rho_v)$. The "method of heating/cooling "for the flows in Figure 2.2-2.3 can be specified by prescribing either the wall temperature values or the heat-flux values. The prescription choice depends on which of the two wall variables is experimentally known or is more conveniently assumed as a tentative prescription. The boiling flows of interest typically have a one-to-one correspondence because of monotonically increasing values of quality X with distance x (or non-dimensional distance $\hat{x}$). It is therefore, possible and common to replace the non-dimensional distance $\hat{x} \equiv x/D_h$ by the local quality $X(\hat{x})$ defined as:

$$X\,(\hat{x}) = \frac{\dot{M}_v(\hat{x})}{\dot{M}_{in}} \tag{2.9}$$

One of several reasons for replacing distance $\hat{x}$ with quality X is the expectation that its use, in place of "$\hat{x}$" will allow more convenient and meaningful characterization of flow-regimes(except near transition boundaries) because of approximate similarities-if G, X and D_h are the same — that are found for certain local quality X(x) dependent variables (such as HTC H_x, void fraction ε, friction fraction f, interiors of different flow regimes in flow-regime maps, etc - (see [5-6], [7], etc.) and those also encountered in corresponding realizations of adiabatic flows (such as ε, f, flow regime map interiors, etc.). It should be noticed that in adiabatic flows, a uniform constant quality $X(x) = X$ (with $0 \leq X \leq 1$) is realized over the entire duct length $L(0 \leq X \leq 1)$. Another advantage of using quality X in place of distance x (or $\hat{x} \equiv x/D_h$) is in developing Nu_x correlation, where

$$Nu_x \equiv \frac{h_x * D_h|_H}{K_L} \tag{2.10}$$

Where $D_h|_H$ and is based on the heated perimeter $P = P_H$ of a duct's cross-section. Here a characteristic length scale D_h typically has two meanings and definitions

$$D_h \equiv \begin{cases} D_h|_H \\ D_h|_F \end{cases} \equiv \begin{cases} 4A/P_H \\ 4A/P_F \end{cases} \tag{2.11}$$

Where A is the cross-sectional area, $P = P_F$ is the wetted (by liquid or vapor) perimeter and $P = P_H$ is the heated perimeter (which may only be a fraction $fr_p \equiv P_H / P_F < 1$ of P_F). For heat-transfer related non-dimensional parameters, such as Nu_x in Equation (2.10), $D_h|_H$ is used and for fluid-flow related parameters (such as friction factor f, liquid Reynolds number Re_L, vapor Reynolds number Re_V etc. defined and discussed in [7]) - typically $D_h|_F$ is used. For circular tubes, $D_h|_F$ is typically the tube diameter (also D or D_h).

Next it is important to define the level of heating and the "method of heating". These "levels" are characterized by either the average temperature difference $\Delta\overline{T}$ or the axially averaged mean wall heat-flux $\bar{q}''_w \equiv \frac{1}{L}\int_0^L q''_w(x)\,dx$. The method of "heating/cooling" is defined as $\theta_w(x)$ or $\Psi_q(x)$ through relations:

$$\Delta T(x) \equiv |T_w(x) - T_{sat}(p_0)| \equiv \Delta\overline{T}.\,\theta_w(x) \tag{2.12}$$

$$q''_w(x) = \bar{q}''_w.\,\Psi_q(x) \tag{2.13}$$

For non-uniform temperature-controlled heating, a specific "method of heating," whereas for uniform temperature heating that specific function is $\theta_w(x) = 1$ over $0 \le x \le L$. Similarly, for a non-uniform wall heat-flux controlled heating, a specific) $\Psi_q(x) \neq 1$ over $0 \le x \le L$ defines a specific "method of heating," whereas for uniform heat-flux heating that specific function is $\Psi_q(x) = 1$ over $0 \le x \le L$.

The local heat transfer coefficient h_x defined through Equation (2.1), depends on the overall flow-specifying geometry and boundary conditions. Once it is assumed that straight ducts and their orientation with respect to gravity are of interest here, the local heat transfer coefficient h_x depends on the following variables(assuming, as needed, an implicit dependence on solid-liquid-vapor interactions related parameters set $\{S^*\}$ that affect nucleation rates) distance "x" from the inlet, tube/duct diameter D_h, inlet mass flow rate $\dot{M}_{in}$, relevant fluid properties, controlling thermodynamic variables for phase-change, the "level" and "method of heating" parameters at the tube walls, values of gravity components g_x and g_y (with X and Y axes as defined in Figure 2.1) for inclined tubes and inlet quality X_{in}. It should be noted that, $g_x \approx 0$ for the horizontal flow configurations of interest in Figures 2.2 - 2.3 and the quality at the inlet ($x = 0$) x^*_{in} is zero for saturated flow-boiling description in Figure 2.2 - 2.3 and $X_{in} > 0$ (with $0 < X_{in} < 1$) is known for the annular flows of the type illustrated in Figure 2.1.

An explicit, minimal, and mutually independence of variables in the parameter set $\{S^*\}$ that characterizes heat transfer rates associated with nucleating bubbles - be it pool ([29]-[33]) or flow ([7], [10-11], [13-14], etc.) boiling - is currently not possible, though many parameters and much about the mechanisms are known (e.g. contact angle, need for a non-dimension characterization of the boiling-surfaces structured or unstructured profile — together with roughness heights, material constants characterizing the solid-liquid-vapor interactions in the "micro-layer" theory ([34], etc.) of bubble ebullition dynamics, etc.). Also , the parameters set $\{S^*\}$ for single-bubble studies ([35]-[36]) are somewhat different with different level of sensitivities leading to a more stochastic response (owing to issues such as oxidation, chemical purity, etc.) as compared to $\{S^*\}$ of interest here - which involves considerations of complex among bubbles of different sizes on a per unit area basis (e.g. variables such as $n''(D_b, \Delta T(x), \{S^*\}, \text{etc.})$ in Equation (2.5)). Therefore $\{S^*\}$ variables influencing local HTC h_x values nucleate boiling component for steady flow boiling in Figures 2.1 - 2.3 — are likely to be lead to greater determinism of h_x than $\{S^*\}$ variables determine a single bubble's ebullition dynamics of [35-36] . And yet the impact of $\{S^*\}$ is expected to lead to a more non-deterministic impact on h_x for steady turbulent duct flow of a pure single phase flow. In the light of new results establishing the significance of micro-nucleation (as outlined in the section of this thesis), the importance of suitably modifying $\{S^*\}$ variables towards beneficially affecting nucleation rates – as in popular passive enhancement techniques involving micro-nano structuring of the boiling surface and affecting variables that control nucleation site densities $n_b''(D_b, \Delta T(x))$ through structural changes in the surface, wettability/spreadability issues ([22], [37-38], etc.) are of technological significance. Active enhancement approaches ([26], [37]-[38]) that also target $\{S^*\}$ variables are also of technological importance – particularly as an "add on" to passive approaches. It is there new technological approaches to enhancement – and addressing of new critical heat flux (CHF) issues related addressing of new critical heat flux (CHF) issues ([39-42) related to new instability mechanisms [7] – both are indicated in Figure 2.3, by curves $I_{1\text{-(ii)}}$ and $I_{2\text{-(ii)}}$ off the regular curve-(ii).

For steady flow boiling situation in Figures 2.1 - 2.2(a), if one allows for the impact of duct orientation with respect to the gravitational acceleration vector $\vec{g}$ - with its x and y components denoted by g_x and g_y - the key variables that affect local HTC $h_x$values can be inferred. The inference follows from above-described discussions with regard to the significant role of $\{S^*\}$ variables that affect hear-carrying mechanism associated with nucleating bubbles at the boiling-surface along with experiences/solutions of rather well known governing equations. ([6-8]) that each phase (L or V) must satisfy in its interior and at their "interior" L-V interfaces. Based on their knowledge, the definition of h_x in the Equation (2.1) - and a given "method of heating ($\theta_w(x)$ or $\Psi_q(x)$)" over $0 \leq x \leq L$ - the following primary functional dependence of h_x on key controlling/ affecting variables are:

$$\begin{aligned} h_x &\cong h_x\left(x, G, D_h, \Delta\bar{T} \text{ or } \bar{q}_w''; \Psi_q(x) \text{ or } \theta_w(x);\ \{S^*\};\ \rho_L, \rho_V, \mu_L, \mu_V, C_{pL}, K_L, h_{fg}, \sigma, g_x, g_y\right) \\ &\cong h_x\left(X(x), G, D_h, \Delta\bar{T} \text{ or } \bar{q}_w'';\ \{S^*\};\ \rho_L, \rho_V, \mu_L, \mu_V, C_{pL}, K_L, h_{fg}, \sigma, g_x, g_y\right) \qquad (2.14) \end{aligned}$$

In Equation (2.14), the simplification in the second equality arises from the fact that "method of heating" - which has a more direct impact on spatial variation of heat-flux and temperature through $\Psi_q(x)$ and $\theta_w(x)$ respectively - typically affects h_x more weakly (see [7] and later results). Also, a replacement for distance x with quality X, as noted in the second equation of Equation (2.14), follows common practices in developing correlation - based on experimental data obtained over suitable parameter space. Utilize the

Nu_xdefinition given in Equation (2.10). Various ways exist for obtaining and listing non-dimensionalized variables on which Nu_x depends. They are all, however, equivalent to the following non-dimensionalized form obtained by using Pi-theorem [43]):

$$Nu_x = Nu_x\left(X(x), Re_T, Ja \text{ or } Bl, Pr_L, We, Fr_x^{-2}, Fr_y^{-2}, \frac{\rho_V}{\rho_L}, \frac{\mu_v}{\mu_L}; \{S_{nd}^*\}\right) \qquad (2.15)$$

In Equation (2.15), for $0 \leq x \leq L, \{S_{nd}^*\}$ represents suitable non-dimensional measures of nucleation controlling parameters $\{S^*\}$, $Re_T \equiv G * \frac{D_h|_F}{\mu_V}$, $Ja = C_{PL} * \Delta\bar{T}/h_{fg}$ or $Bl = \bar{q}''_w/G * h_{fg}$, $Pr_L \equiv \frac{\mu_L C_{pL}}{K_L}$, $Fr_x^{-2} \equiv g_x.\frac{D_h|_F}{U^2}$, $Fr_y^{-2} \equiv g_y.\frac{D_h|_F}{U^2}$, and $We \equiv \rho_L U^2 D_h|_F/\sigma$.

2.2.3 Correlation, 1-D Governing Equations, and Other Modelling Knowledge

Different types of correlations for local (at location "x") values of variables such as HTC h_x, qualify X(x), void fraction $\epsilon(x)$ non-dimensionalized Versions of frictional pressure gradient, flow regime maps' boundaries, etc. exist for steady flow boiling (Figure 2.1 - 2.2), and - with the help of one-dimensional (1-D) balance laws for mass, momentum, and energy - they are often synthesized with information on similar variables (except h_x) for corresponding adiabatic two-phase flows) see Figure 2.4 where mass flux G, quality X, and hydraulic diameter $D_h$are the same.

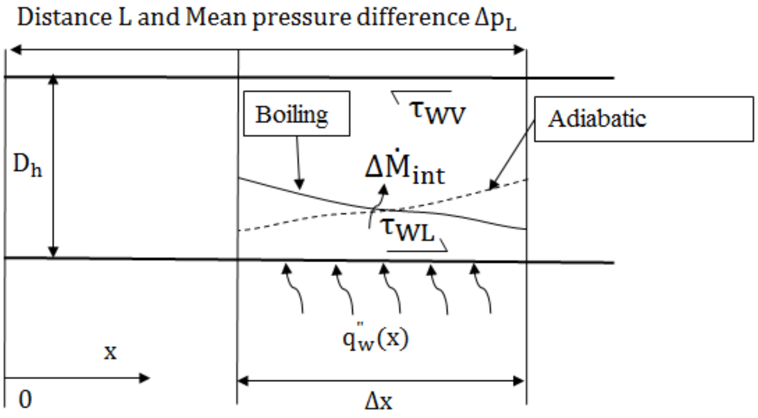

Figure 2-4 The schematic of a channel/tube flow's control-volume between "x" and "x + Δx". The heat-flux arrows, as shown, are positive for boiling. The hydraulic diameter is D_h, perimeter in P, the heated perimeter is P_H, and cross-sectional area in A.

2.2.3.1 HTC correlation for h_x or $Nu_x$and 1-D Balance laws of Mass and Energy Yield Quality X(x) variation.

Known Nu_x correlation ([7], [11-12], [12-15]) of the type (or approximately equivalent to) given in Equation (2.15) combined with 1-D mass and momentum balances for the control-volume (of width "Δx" shown in Figure 2.4. Recall that 1-D mass balance states:

$$\dot{M}_L(x) + \dot{M}_V(x) = \dot{M}_{in} \equiv G.A \tag{2.16}$$

Furthermore 1-D energy balance states:

$$\frac{dX(x)}{dx} = \frac{h_x.\Delta T_w(x).P_H}{G.A * h_{fg}}, 0 \leq k \leq L \tag{2.17}$$

Numerical integration of Equation (2.17), with known $h_x = h_x\,(x, \dots)$ and knowledge of an initial condition yields thermodynamic quality X's variation with the distance "x". Various non-dimensional used versions of Equation (2.17) - suitable for different types of numerical integration depending on what is known about "method of heating" and nature of available h_x correlations are discussed in [7]. The proximity, at any x, of thermodynamic quality X(x) to the mass quality $X(x) \equiv \dot{M}_V(x) / \dot{M}_{in}$ depends on how accurately experimental condition approximate saturated all liquid condition at boiling phase-change occurring over $x > x^*$.

2.2.3.2 Void-fraction, Flow regime Maps, and Momentum balance for a differential control-volume.

Before writing the momentum balance for the control-volume (of width "Δx") shown in Figure 2.4, the following notations are introduced. Let $A_V(x)$ and $A_V(x)$ respectively represent parts of cross-sectional area $A(\equiv A_L(x) + A_V(x))$ that are occupied by the liquid and vapor phases (their time average values for the steady flows in Figure 2.1 and 2.2(a)). Let the corresponding vapor and liquid parts of the perimeter P be denoted as P_V and P_L with $P \equiv P_V + P_L$. The void-fraction $\epsilon(x)$ at any known x in Figure 2.4 where quality is X(x), is given by:

$$\epsilon(x) \equiv \frac{A_V(x).\Delta x}{A.\Delta x} = \frac{A_V(x)}{A} \quad (2.18)$$

The local void-fraction in Figure 2.4 is often considered "similar" to the corresponding adiabatic flows void-fraction in Figure 2.4. Because of this, various correlations in the form of $\epsilon = \epsilon$ (X, non-dimensionalized fluid properties) are widely reported. The approximation assumes that, if $\dot{M}_{int}$ (Phase Change rates in kg/s over Δx in Figure 2.4) is much smaller than $\dot{M}_L(x)$ and $\dot{M}_V(x)$, then the local correspondence between flow-boiling and adiabatic flows should hold.

However, flow-regime maps (see [7], [11-12], etc.) demarcate boundaries between various flow regimes which represent the signature of instabilities that dictate various liquid-vapor configuration - and such boundaries are often different between flow-boiling and adiabatic flows. This is because the cumulative effects of $d\dot{M}_{int}/_{dx} \cong \Delta\dot{M}_{int}/_{\Delta x} > 0$, as an integration from $x = x^*$ (where $X(x^*) \cong U$) to a location of interest $x(> x^*)$, cannot be ignored. As a result of this observation, the papers ([1]-[3]) and the thesis recommend that use of void-fraction correlation ([5], [42-45]) for $\epsilon(x)$ should be subjected to "supplied boundary conditions" from flow-boiling experiments.

For example, by "supplied boundary condition" for a location $x = x^\#$, where $x^\#$ is a location in the steady annular regimes of flow-boiling in Figure 2.1 or 2.2(a), should assert the knowledge of the flow-regime at $x = x^\#$ and the associated quality $X(x^\#)$ as well as the void-fraction $\epsilon^* \equiv \epsilon(X(x^\#))$. For steady annular flows in Figure 2.4, if the ducts correspond to a horizontal 2-D channel formed by two plates (with the boiling-surface being the lower one) of gap h and width w, an assertion of annularity at $x = x^\#$ implies:

$$\epsilon^{\#} = \frac{A_V(x^{\#})}{A(x^{\#})} \cong \frac{\left(h - \Delta(x^{\#})\right).w}{h.w} \cong 1 - \frac{\Delta(x^{\#})}{h} \tag{2.19}$$

Therefore, use of $\epsilon(x)$ correlation ([44]-[48]) should be supplemented with experimental knowledge of annularity at $x = x^{\#}$ as well as an estimate of $\epsilon^{\#}$ (i.e. $\Delta x^{\#}$) in Equation (2.19).

2.2.3.3 One Dimensional Pressure Drop Models

Momentum balance for the differential control-volume in Figure 2.4 can be written - with the assumption of uniform pressures at “x” and “$x + \Delta x$” - as (see [7], [11], etc.):

$$\left(\frac{\partial p}{\partial x}\right) = \left(-\frac{\partial p}{\partial x}\right)_{fric} + \left(-\frac{\partial p}{\partial x}\right)_{g} + \left(-\frac{\partial p}{\partial x}\right)_{acc} \tag{2.20}$$

Where

$$\left(-\frac{\partial p}{\partial x}\right)_{acc} = G^2 \frac{d}{dx}\left[\frac{X(x)^2}{\rho V.\epsilon} + \frac{(1 - X(x))^2}{\rho_L * (1 - \epsilon)}\right] \tag{2.21}$$

$$\left(-\frac{\partial p}{\partial x}\right)_{g} = [\epsilon\, \rho_V + (1 - \epsilon)\rho_L].\, g \sin\Psi \tag{2.22}$$

And non-dimensional correlated forms-based estimates of $\left(-\frac{\partial p}{\partial x}\right)_{fric}$

$$\left(-\frac{\partial p}{\partial x}\right)_{fric} \equiv \frac{1}{A}[\tau_{wv} * P_V + \tau_{wl} * P_L] \tag{2.23}$$

Are available in the literature (see [7]). These correlations can be used through the assumed modeling correspondence between “local” flow-boiling condition and adiabatic flows -as discussed for Figure 2.4.

Use of integrated form of the momentum balance in Equation (2.20) with experimentally measured values of ΔP_L in Figure 2.4, requires that the following be satisfied:

$$\Delta p_L = \int_0^L \left(-\frac{\partial p}{\partial x}\right)_{fric} . dx + \int_0^L \left(-\frac{\partial p}{\partial x}\right)_g . dx + \left(-\frac{\partial p}{\partial x}\right)_{acc} . dx \quad (2.24)$$
$$\equiv (\Delta p)_{fric} + (\Delta p)_g + (\Delta p)_{acc}$$

Use of experimental measured Δp_L in Equation (2.24) along with X(x) estimates from Equation (2.17), void-fraction estimates from Equation (2.19), and correlation for non-dimensional values of $\left(\frac{\partial p}{\partial x}\right)_{fric}$ and void fraction correlation $\in$ (x) can provide for good and consistent 1-D estimates for the engineering design variable of interest.

REFERENCES

1. Narain, A., H. Ranga Prasad, **Gorgitrattanagul, P**, S. Sepahyar and Mehendale, S, "Significant Role of Micro-scale Nucleation Rates as Heat-Carrying Mechanism for Steady Annular Flow boiling (traditionally termed Convective Regime), Part I: Modeling/Simulations Support for Assessments of Experimental Data." **To be submitted**.
2. Gorgitrattanagul, P., **A. Narain,** R. Kumar*, S. Sepahyar, and D. Pandya, "Significant Role of Micro-scale Nucleation Rates as Heat-Carrying Mechanism for Steady Annular Flow boiling (traditionally termed Convective Regime), Part II: Experiments and Results for Low Heat-flux Operations with FC-72 as a Working Fluid." **To be submitted**.
3. Gorgitrattanagul, P., A. Narain, M. T. Kivisalu, and D. Pandya, "Investigations of Temperature Controlled Innovative Annular Flow-boiling of FC-72 in Millimeter Scale Ducts Part IV: Enhanced Pulsatile Cases." International Journal of Heat and Mass Transfer, 2018." **To be submitted.**
4. Soroush Sepahyar, Michael Kivisalu, Harsha Sathi, and Amitabh Narain, "Significant Role of Micro-scale Nucleation Rates as Heat-Carrying Mechanism for Steady Annular Flow boiling (traditionally termed Convective Regime), Part III: Experiments and Results for High Heat-flux Operations with Water as a Working Fluid." **To be submitted**.

5. Carey VP (1992) Liquid-vapor phase-change phenomena. Series in chemical and mechanical engineering. Hemisphere Publishing Corporation, New York.
6. Ghiaasiaan SM (2007) Two-phase flow, boiling, and condensation: in conventional and miniature systems. Cambridge University Press, Cambridge.
7. Narain, A., Ranga Prasad, H. and Koca, A., “Internal Annular Flow Condensation and Flow Boiling: Context, Results, and Recommendations.” *In: Kulacki FA (ed.) Handbook of Thermal Science and Engineering*, 2018, *vol. 3, pages 2075-2162. Springer,* Cham. Invited Article.
8. Naik, R., Narain, A., and Mitra, S., “Steady and unsteady simulations for annular internal condensing flows, part I: algorithm and its accuracy.” *Numerical Heat Transfer,* Part B: Fundamentals. 2016, 69(6), pp. 473-494.
9. Naik, R., Narain, A., “Steady and unsteady simulations for annular internal condensing flows, part II: instability and flow regime transitions.” Numerical Heat Transfer, Part B: Fundamentals. 2016, 69(6), pp. 495-510.
10. Ranga Prasad, H, Narain, A, Bhasme S., Naik, R., “Shear-driven annular flow-boiling in millimeter-scale channels: direct numerical simulations for convective component of the overall heat transfer coefficient.” *International Journal of Transportation Phenomena.* 2017, vol. 15, No. 1, pp 1–35. Invited Paper.
11. Narain, A., “Modeling of Interfacial Shear for Gas Liquid Flows in Annular Film Conden¬sation.” Journal of Applied Mechanics (Transactions of America Society of Mechanical Engineering). 1996, 63(2), pp. 529-538.
12. Kim S-M, Mudawar I (2013c) Universal approach to predicting saturated flow boiling heat transfer in mini/micro-channels – Part II. Two-phase heat transfer coefficient. *International Journal of Heat and Mass Transfer*, 64: 1239-1256.
13. Klimenko, V. V. "A generalized correlation for two-phase forced flow heat transfer." International Journal of heat and mass transfer 31, no. 3 (1988): 541-552.
14. Kandlikar, Satish G. "A general correlation for saturated two-phase flow boiling heat transfer inside horizontal and vertical tubes." *Journal of heat transfer* 112, no. 1 (1990): 219-228.

15. Dorao, Carlos A., Oscar Blanco Fernandez, and Maria Fernandino. "Experimental Study of Horizontal Flow Boiling Heat Transfer of R134a at a Saturation Temperature of 18.6 C." *Journal of Heat Transfer* 139, no. 11 (2017): 111510.
16. S. M. Yih. Modelling heat and mass transport in falling liquid films. *In: Handbook of Heat and Mass Transfer*. Gulf Publishing, Houston. (1986) 134-143.
17. H. Chen, R. S. Jebson. Factors affecting heat transfer in falling film evaporator. Institute of Chemical Engineers. 57 (1997) 111-116.
18. R. Krupiczka, A. Rotkege, Z. Ziobrowski. Heat transfer to evaporating liquid films within a vertical tube. Chemical Engineering and Processing. 41 (2002) 23-38.
19. Bjorn Palm & Joachim Claesson. Plate Heat Exchanger: Calculation Methods for Single and Two-Phase Flow. Heat Transfer Engineering, 27:4 (2006) 88-98. DOI:10.1080/01457630500523949.
20. B. Palm, J. Claesson, Plate heat exchanger: calculation methods for single and two-phase flow, Heat Transfer Engineering. 27 (2006) 88-98.
21. B. Thonon, A. Feldman, L. Margat and C. Marviilet. Transition from nucleate boiling to convective boiling in compact heat exchangers. *International Journal for Refrigeration*. 20:8 (1997) 592-597.
22. Kuo, Chih-Jung, Ali Kosar, Yoav Peles, Steven Virost, Chandan Mishra, and Michael K. Jensen. “Bubble dynamics during boiling in enhanced surface microchannels.” *Journal of Microelectromechanical Systems* 15, no. 6 (2006): 1517-1527.
23. Kenning D, Cooper M (1989) Saturated flow boiling of water in vertical tubes. Int J Heat Mass Transf 32(3):445–458.
24. Chen JC (1966) Correlation for boiling heat transfer to saturated fluids in convective flow. Industrial Engineering Chemistry Process Design and Development, 5(3):322–329.
25. Cooper M (1989) Flow boiling—the ‘apparently nucleate regime. *International Journal of Heat Mass Transfer*, 32(3):459–464.
26. Patcharapol Gorgitrattanugul, Ph.D. from MTU. “Experimental Investigation of temperature controlled innovative annular flow-boiling of FC-72 in millimeter scale ducts-steady and enhanced pulsatile realizations.” (2017).

27. Incropera, Frank P., Adrienne S. Lavine, Theodore L. Bergman, and David P. DeWitt. *Fundamentals of heat and mass transfer*. Wiley, 2007.
28. Ross, H., R. Radermacher, M. Di Marzo, and D. Didion. "Horizontal flow boiling of pure and mixed refrigerants." *International journal of heat and mass transfer,* 30, no. 5 (1987): 979-992
29. Cooper M (1984a) Heat flow rates in saturated nucleate pool boiling-a wide-ranging examination using reduced properties. *Advances in Heat Transfer*, 16:157–239.
30. Cooper M (1984b) Saturation nucleate pool boiling—a simple correlation. Institute of Chemical Engineers. Symp Ser 86(2):785–793.
31. Dhillon NS, Buongiorno J (2017) Effect of surface roughness on the behavior of bubbles growing and departing from a heated surface. In: Summer heat transfer conference SHTC, Bellevue, 9–14 July 2017.
32. Dhir V (1998) Boiling heat transfer. Annu Rev Fluid Mech 30(1):365–401.
33. Dhir V, Liaw S (1989) Framework for a unified model for nucleate and transition pool boiling. *Journal of Heat Transfer*, 111(3):739–746.
34. Kunkelmann C, Ibrahem K, Schweizer N, Herbert S, Stephan P, Gambaryan-Roisman T (2012) The effect of three-phase contact line speed on local evaporative heat transfer: experimental and numerical investigations. *International Journal of Heat Mass Transfer*, 55(7–8):1896–1904.
35. McHale John P., Garimella Suresh V. (2010) Bubble nucleation characteristics in pool boiling of a wetting liquid on smooth and rough surfaces. *International Journal of Multiphase Flow* 36(4):249–260.
36. Bigham, S. and Moghaddam, S., Microscale study of mechanisms of heat transfer during flow boiling in a microchannel. *International Journal of Heat and Mass Transfer*, 2015. 88: p. 111-121.
37. Gorgitrattanagul, P., A. Narain, M. T. Kivisalu, and D. Pandya, "Investigations of Temperature Controlled Innovative Annular Flow-boiling of FC-72 in Millimeter Scale Ducts Part IV: Enhanced Pulsatile Cases." *International Journal of Heat and Mass Transfer*, 2018." **To be submitted.**

38. A. Narain, V. Vivek, D. Pandya, S. Sepahyar, Efficient enhancement of nucleation rates in flow-boiling - by concurrent micro-structuring of the boiling-surface and its judicious energization by Piezoelectric-transducer induced acoustic waves. [November 12, 2018 Provisional Patent: Attorney Docket number: 066040-9957-US01].
39. Katto Y (1994) Critical heat flux. *International Journal for Multiphase Flow*, 20:53–90.
40. Katto Y, Ohno H (1984) An improved version of the generalized correlation of critical heat flux for the forced convective boiling in uniformly heated vertical tubes. *International Journal of Heat and Mass Transfer*, 27(9):1641–1648.
41. Kim S-M, Mudawar I (2013b) Universal approach to predicting saturated flow boiling heat transfer in mini/micro-channels – part I. Dryout incipience quality. *International Journal of Heat and Mass Transfer*, 64:1226–1238.
42. Das PK, Chakraborty S, Bhaduri S (2012) Critical heat flux during flow boiling in mini and microchannel-a state of the art review. *Frontiers in Heat and Mass Transfer*, 3(1).
43. White FM (2003) *Fluid mechanics*. McGraw-Hill, Boston.
44. Zivi S (1964) Estimation of steady-state void fraction by means of principle of minimum energy production. ASME *Journal of Heat Transfer* 86(2):247–252.
45. Steiner D (1993) Heat transfer to boiling saturated liquids VDI-Wärmeatlas (VDI heat atlas). VDI-Gesellschaft Verfahrenstechnik und Chemieingenieurswesen (GCV), Düsseldorf.
46. Thome JR (2004) Engineering data book III. Wolverine Tube Inc, Huntsville.
47. Rouhani SZ, Axelsson E (1970) Calculation of void volume fraction in the subcooled and quality boiling regions. *International Journal of Heat and Mass Transfer,* 13(2):383–393
48. Cioncolini, A., Thome, J.R., 2012. Void fraction prediction in annular two-phase flow. *International Journal of Multiphase Flow* 43, 72-84.

3 Brief Outline of Experimental and Data Processing/ Simulation Approaches and Their Implementations

Results from steady high heat-flux (15-70 W/cm^2, with water as working fluid) shear driven annular flow-boiling experiments presented here required planning and implementation for: (i) experimental test-section, (ii) experimental flow-loop and its control, (iii) data acquisition of measured variables, (iv) simulation experiments synthesis for estimating the values of indirectly measured variables, and (v) assessment of uncertainties associated with directly and indirectly measured variables. These are described below in various sub-section - with their additional details given in referenced Appendices.

3.1 Experimental Test-section and Acquired Data

The results reported here are experiments done in horizontal rectangular cross-section channel of height 5 mm and width 10 mm with the length being 14 cm in the direction of water flow (see Figure 3.1). Non-zero inlet quality (between 0.4 - 0.7) arranged by introducing, at the inlet, separate flows of nearly saturated water and steam (Liquid & Vapor phases) -at mass flow rates consistent with imposed heat-fluxes - ensure annularity over the entire length of the horizontal boiling surface at the bottom of the test section.

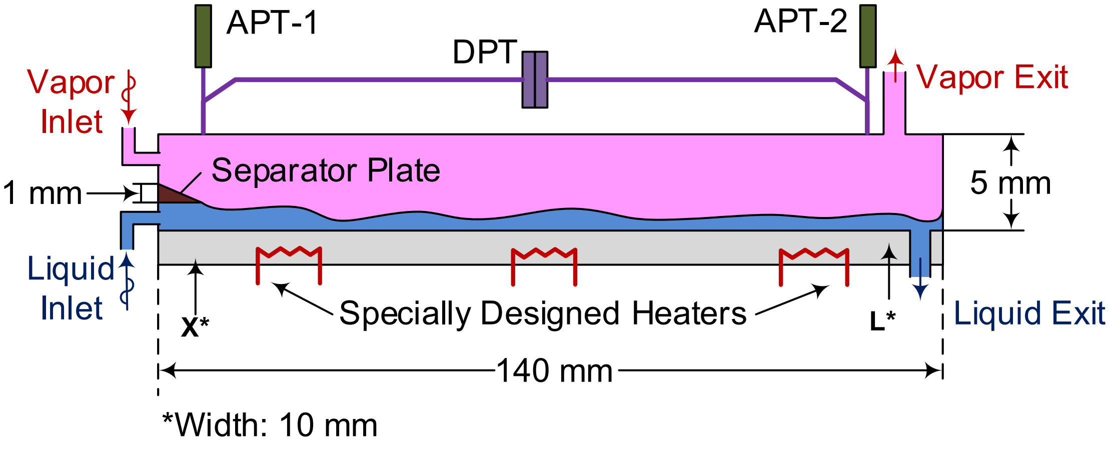

Figure 3-1 A lateral section schematic of the experimental flow channel is shown. The length of the flow channel is 0 < x < 14 cm and total mass flux into the channel is in the

range: $100 < \mathrm{G} < 200 \ {}^{\mathrm{kg}}/_{(\mathrm{m}^2.\,\mathrm{s})}$. Inlet quality X_{in} is arranged to be in the range $0.4 < X_{in} < 0.75$. In the figure, x^* indicates the approximate location downstream of the inlet where bulk mean temperature approaches saturation temperature and nucleate-boiling contribution start within annular flow-regimes. The location L^* near the outlet is where flow-boiling ends and stagnation-zone begins. The x^* and L^* values change slightly for different test cases, slightly changing the actual heated length of interest: $x^* < x < L^*$.

Before reaching the milestone leading to the data reported in Tables 1-2 and Figure 3.2(a), analysis based understanding was used to modify and improve the working hardware to a point where results were validated and made consistent with the supporting theory and computational results. For the current hardware arrangement, the location L^* near the outlet in Figure 3.1 is a location up to which ($x \leq L^*$) the upstream flow can determine by itself the needed exit condition (i.e. information primarily flows from upstream to downstream locations). But between location L^* and the stagnation-chamber (including its walls and exit ports), the flows has recirculation and is likely affected by both upstream and downstream conditions - which is, in the language of flow-simulation, an “elliptic” zone. Once this physics fact was clearly understood and established, separate vapor and liquid flows through the Figure 3.1 ports marked, respectively, vapor exit on the top and liquid exit on the bottom were maintained with the same control .This was accomplished by ensuring that the existing liquid flow rate in Figure 3.1 was controlled and kept at a value that was consistent with the overall energy balance for the test-section. This liquid exit flow rate control on LabVIEW required a Coriolis meter and a controllable pump further downstream of the existing liquid port in Figure 3.1. This control helped in two ways: (i) a test-section re-design where existing liquid and vapor are separated in a different chamber downstream of the test-section exit, and (ii) an ability to separate heat-transfer related phase-change effects from the predominantly adiabatic liquid entrainment effects (for some cases involving misty annular flows).

Table 1-A Selected Flow Variables from a Set of Steady Run Cases Whose "Method of Heating" is Defined by Function in Figure 3.2(a)

DATA SET - 1

Case	P_{in}	P_{out}	ΔP	$\dot{M}_{L_{in}}$	$\dot{M}_{V_{in}}$	$\dot{M}_{L_{out}}$	$\dot{M}_{V_{out}}$	$T_{Sat(P_o)}$	$\overline{T}_W$	ΔT	$\dot{M}_{Total}$	G	X_{in}	X_{out}	$\bar{q}''_W$
abs error (δx)	3.50	3.50	0.57	0.00247	0.023	0.00206	0.0232	0.83	0.53	0.98	0.0231	0.972	0.0047	0.0055	1.0567
Max relative error (δx/x)	0.0329	0.0352	0.0103	0.0010	0.0050	0.0010	0.0058	0.0082	0.0048	0.1113	0.0039	0.0069	0.0063	0.007	0.0150
% relative error	±3.29%	±3.52%	±1.03%	±0.10%	±0.50%	±0.10%	±0.58%	±0.82%	±0.48%	±11.13%	±0.39%	±0.69%	±0.63%	±0.7%	±2.98%
Unit	[kPa]	[kPa]	[kPa]	[g/s]	[g/s]	[g/s]	[g/s]	[°C]	[°C]	[°C]	[g/s]	[kg/s/m^2]	-	-	[W/cm^2]
1	106.5	99.4	7.1	1.54	4.54	1.28	4.8	101.37	110.84	9.46	6.08	121.73	0.75	0.79	21.16
2	109.6	102	7.6	1.72	4.58	1.4	4.9	102.19	118.98	16.78	6.3	126.11	0.72	0.77	32.81
3	111.5	104.2	7.3	1.82	4.25	1.42	4.65	102.68	123.43	20.75	6.07	121.52	0.7	0.76	40
4	113.8	106.5	7.4	2.22	3.69	1.89	4.02	103.28	123.97	20.7	5.91	118.27	0.62	0.68	42.83
5	118	110.3	7.6	2.26	4.56	1.87	4.95	104.3	127.97	23.67	6.82	136.57	0.67	0.72	47.6
6	119.1	111.5	7.7	2.47	4.36	2.06	4.77	104.58	127.68	23.1	6.83	136.72	0.64	0.7	46.96
7	120.6	113	7.6	2.47	4.6	2.06	5	104.94	131.8	26.85	7.07	141.38	0.65	0.71	57.26
Min	106.5	99.4	7.1	1.54	3.69	1.28	4.02	101.37	110.84	9.46	5.91	118.27	0.62	0.68	21.16
Max	120.6	113	7.7	2.47	4.6	2.06	5	104.94	131.8	26.85	7.07	141.38	0.75	0.79	57.26

Table 1-B Selected Flow Variables from a Set of Steady Run Cases Whose “Method of Heating” is Defined by Function in Figure 3(b)

Case	$\bar{h}$	$\overline{Nu}$	X_{in}	$Re_{L_{in}}$	$Re_{V_{in}}$	Re_{Total}	Ja	Pr_L	ρ_V/ρ_L	μ_V/μ_L	$\delta\bar{h}/\bar{h}$	$\delta\overline{Nu}/\overline{Nu}$	h_x
abs error	2545.23	25.71	0.0059174	39.69	1649.08	2451.21	0.006817	0.0357	0.0000104	0.0006350	-	-	-
Max relative error	±11.42%	±11.86%	±0.79%	±3.39%	±3.39%	±3.30%	±11.22%	±1.73%	±1.41%	±1.41%	±11.42%	±11.86%	-
Unit	[W/m^2.°C]	-	-	-	-	-	-	-	-	-	-	-	See to figure 4.1
8	22284	216.82	0.75	614	48354	64757	0.01981	2.0613	0.000654	0.0374	11.421	0.1185	
9	24334	236.65	0.72	734.89	48645	66903	0.04743	1.92	0.000672	0.0403	-	-	
10	23206	225.62	0.7	758	45171	64484	0.06076	1.97	0.000683	0.0392	4.976	0.0507	
11	24968	242.67	0.62	1039.5	39217	62768	0.04066	1.75	0.000697	0.0441	-	-	
12	25269	245.73	0.67	1054.5	48141	72046	0.04574	1.76	0.000722	0.0441	-	-	
13	24859	241.44	0.64	1170.8	46061	72128	0.04322	1.73	0.000728	0.0449	4.376	0.0448	
14	26417	256.52	0.6495	1170.4	48289	74348	0.04983	1.73	0.000737	0.0449	3.255	0.0340	
Max	26417	256.52	0.75	1170.8	48645	74348	0.06076	2.0613	0.000737	0.0449	11.421	0.1186	

DATA SET – 2

Table 2-A Calculated Parameters for Corresponding Case-Specific Values in Table 1-A.

Case	P_{in}	P_{out}	ΔP	$\dot{M}_{L_{in}}$	$\dot{M}_{V_{in}}$	$\dot{M}_{L_{out}}$	$\dot{M}_{V_{out}}$	$T_{Sat(P_o)}$	$\overline{T}_W$	ΔT	$\dot{M}_{Total}$	G	X_{in}	X_{out}	$\bar{q}''_W$
abs error (δx)	3.50	3.50	0.57	0.00237	0.015	0.00198	0.0153	0.83	0.9	0.98	0.0151	0.72390	0.00386	0.00460	1.0567
Max relative error (δx/x)	0.0318	0.0322	0.0103	0.0010	0.0050	0.0010	0.0053	0.0082	0.0076	0.0586	0.0037	0.0068	0.0062	0.0065	0.0150
% relative error	±3.18%	±3.22%	±1.03%	0.10%	0.50%	0.10%	0.53%	±0.82%	±0.76%	±5.86%	±0.37%	±0.83%	±0.62%	±0.65%	±3.03%
Unit	[kPa]	[kPa]	[kPa]	[g/s]	[g/s]	[g/s]	[g/s]	[°C]	[°C]	[°C]	[g/s]	[kg/s/m^2]	-	-	[W/cm^2]
1	109.9	108.81	1.1	1.55	2.55	1.18	2.92	102.12	118.93	16.81	4.11	82.21	0.622	0.711	32.7
2	111.39	110.58	0.8	1.88	2.51	1.51	2.88	102.54	124.16	21.62	4.39	87.91	0.573	0.655	39.85
3	113.49	112.69	0.8	1.91	2.66	1.5	3.07	103.08	127.94	24.86	4.57	91.48	0.582	0.671	48.88
4	114.27	113.73	0.5342	2.158	2.78	1.83	3.11	103.31	128.14	24.83	4.93	98.77	0.563	0.629	48.04
5	118.3	116.78	1.51	2.16	2.87	1.82	3.21	104.58	131.77	27.19	5.03	100.67	0.571	0.638	53.39
6	119.21	117.71	1.51	2.37	2.92	1.94	3.5	104.41	132.46	28.05	5.29	105.92	0.551	0.632	57.28
7	122.58	121	1.65	2.35	3	1.98	3.37	105.2	136.36	31.16	5.35	107.14	0.561	0.629	65.7
Min	109.9	108.81	0.5342	1.55	2.51	1.18	2.88	102.12	118.93	16.81	4.11	82.21	0.551	0.629	32.7
Max	122.58	121	1.65	2.37	3	1.98	3.5	105.2	136.36	31.16	5.35	107.14	0.622	0.711	65.7

Table 2-B Calculated Parameters for Corresponding Case-Specific Values in Table 1-B.

Case	$\bar{h}$	$\overline{Nu}$	X_{in}	$Re_{L_{in}}$	$Re_{V_{in}}$	Re_{Total}	Ja	Pr_L	ρ_V/ρ_L	μ_V/μ_L	$\delta\bar{h}/\bar{h}$	$\delta\overline{Nu}/\overline{Nu}$	h_x
abs error	2545.23	26.27	0.0048917	39.26	1066.06	1847.7	0.0042289	0.0316965	0.0000106	0.0006661	-	-	-
Max relative error	±11.42%	±11.86%	±0.79%	±3.39%	±3.39%	±3.30%	±7.42%	±1.73%	±1.41%	±1.41%	±11.42%	±11.86%	-
Unit	[W/m^2.°C]	-	-	-	-	-	-	-	-	-	-	-	⋮
8	22166	215.56	0.62	740.45	27036	43466	0.03017	1.72	0.000674	0.0451	0.0687	0.0758	
9	20915	203.36	0.57	849.35	26375	46234	0.03874	1.83	0.000683	0.0427	0.0760	0.0824	
10	22164	215.43	0.58	869.46	28016	48088	0.04533	1.8017	0.000695	0.0433	0.0544	0.0631	
11	21917	213.01	0.563	1035.7	29236	51931	0.04531	1.71	0.0007	0.0456	0.0588	0.0668	
12	21914	212.87	0.571	1045.2	30251	52958	0.05152	1.7	0.000723	0.046	0.0496	0.0590	
13	23120	224.55	0.55	1155.3	30720	55717	0.05108	1.687	0.000729	0.0462	0.0714	0.0782	
14	22750	220.87	0.53	1158.1	31447	56043	0.057	1.665	0.000748	0.0471	0.0714	0.0782	
Max	23120	224.55	0.62	1158.1	31447	56043	0.057	1.83	0.000748	0.0471	0.0760	0.0824	

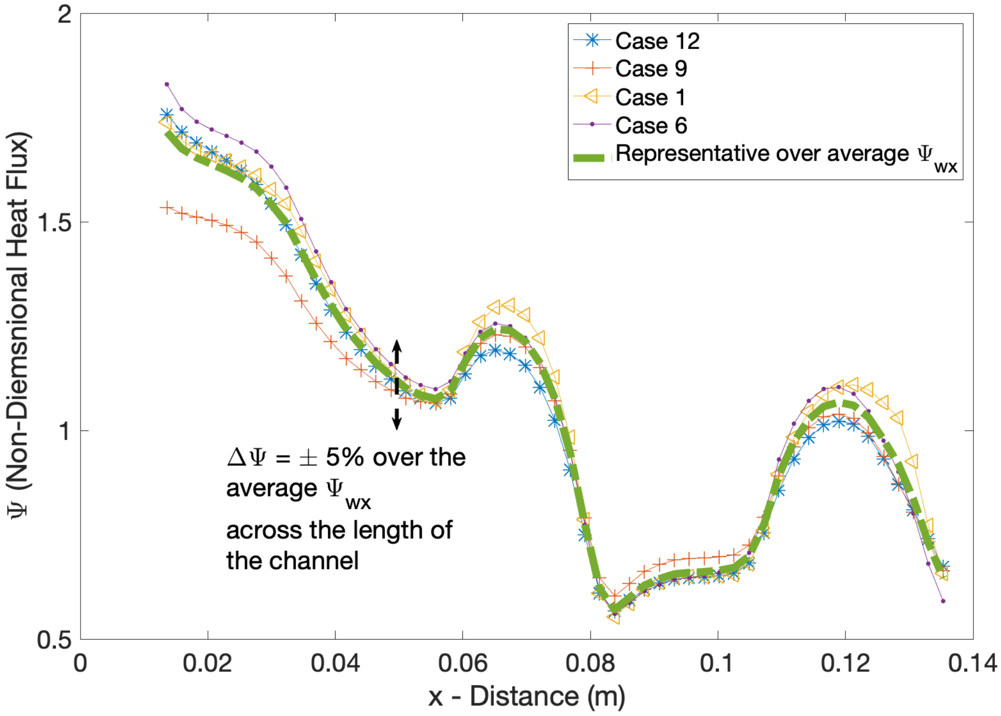
Case 12
Case 9
Case 1
Case 6
Representative over average Ψ_{wx}
$\Delta\Psi$ = ± 5% over the average Ψ_{wx} across the length of the channel
Ψ (Non-Diemsnional Heat Flux)
x - Distance (m)
2
1.5
1
0.5
0
0.02
0.04
0.06
0.08
0.1
0.12
0.14

(a)

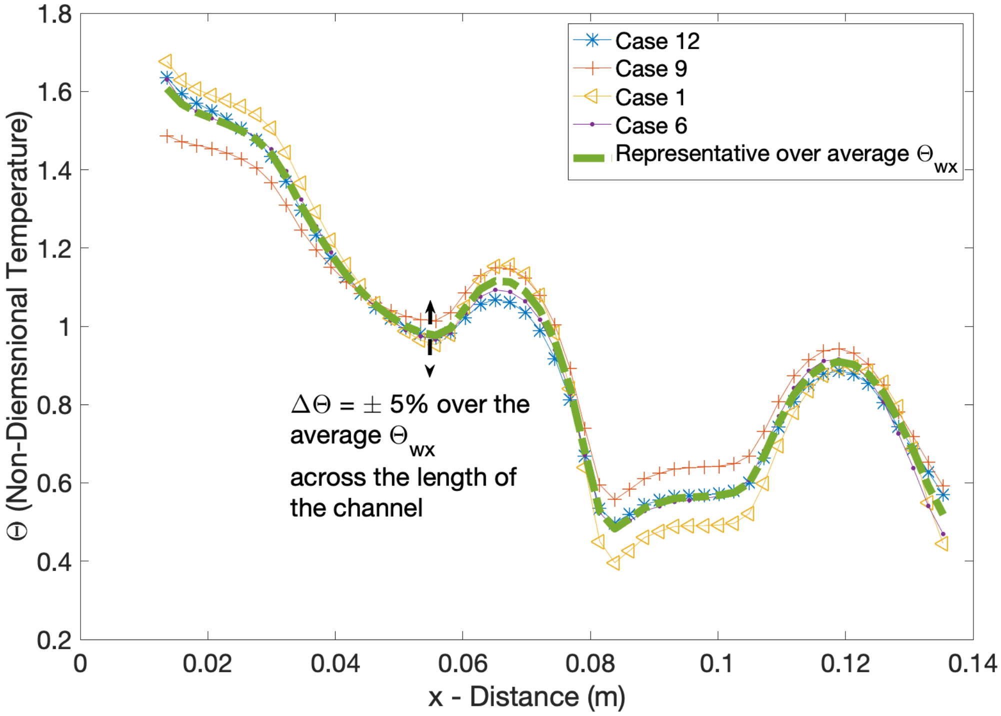
Case 12
Case 9
Case 1
Case 6
Representative over average Θ_{wx}
$\Delta\Theta$ = ± 5% over the average Θ_{wx} across the length of the channel
Θ (Non-Diemsnional Temperature)
x - Distance (m)
1.8
1.6
1.4
1.2
1
0.8
0.6
0.4
0.2
0
0.02
0.04
0.06
0.08
0.1
0.12
0.14

(b)

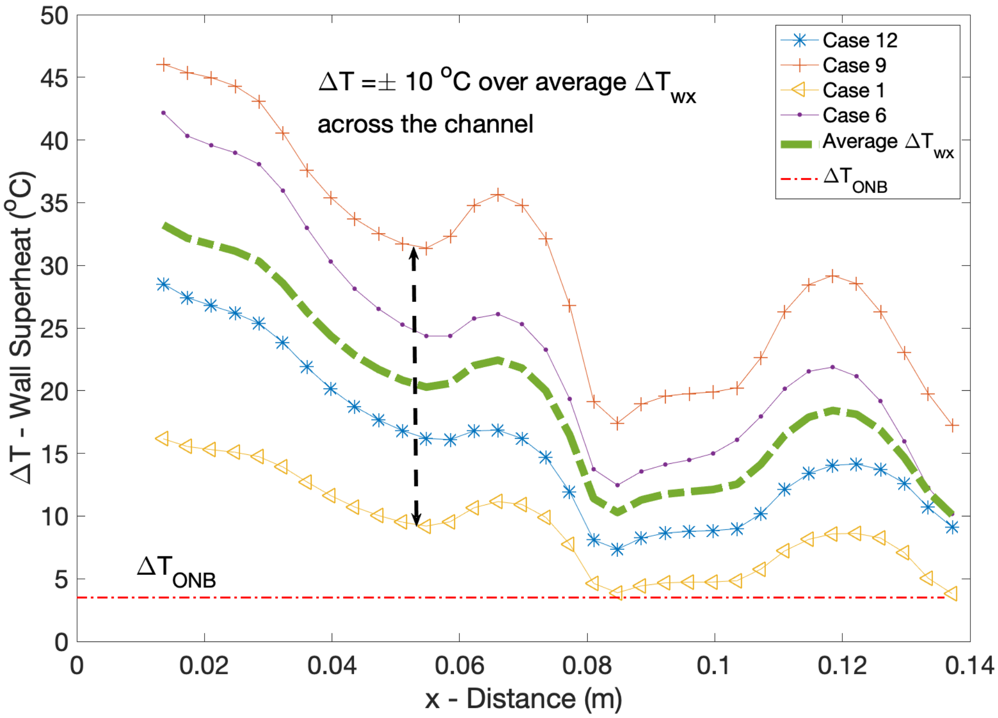

(c)

Figure 3-2: The dotted bold line in the figures above represents the non-uniform "method of heating." **(a)** $\theta_w(x)$ as defined in section-2. Within ± 5 %, the $\theta_w(x)$ curves in application to all the data acquired and reported in Tables 1-2. **(b)** $\Psi_q(x)$ as defined in section-2. Within ± 5 %, the $\Psi_q(x)$ curve is applicable to all the data acquired and reported in Tables 1-2. **(c)** ΔT Wall Superheat range over ±10% of average ΔT for all data sets in Tables 1-2.

The data reported in Tables 1-2 cover, respectively, the following range of raw and non-dimensionless data

For Table-1

Raw Data Range

$100\ {}^{kg}/_{(m^2-s)} \leq G \leq 200\ {}^{kg}/_{(m^2-s)}$;

$10\ {}^{W}/_{cm^2} \leq \bar{q}''_w \leq 80\ {}^{W}/_{cm^2}$;

$106.5\ \mathrm{kPa} \le p_0 \le 121\ \mathrm{kPa}$

Non-dimensional Data Range

$0.65 \le X_{in} \le 0.75$

$613.43 \le Re_{L-in} \le 1169.43$ (Laminar Liquid Flow)

$48253 \le Re_{V-in} \le 48317$

$0.000654 \le {}^{\rho_V}/_{\rho_L} \le 0.000737$

$0.01981 \le Ja \le 0.06076$

$1.74 \le Pr_L \le 2.06$

$0.0374 \le {}^{\mu_V}/_{\mu_L} \le 0.0494$

$64705 \le Re_{Total} \le 74288$

For Table-2

Raw Data Range

$82\ {}^{\mathrm{kg}}/_{(\mathrm{m}^2-\mathrm{s})} \le G \le 107\ {}^{\mathrm{kg}}/_{(\mathrm{m}^2-\mathrm{s})}$;

$38\ {}^{\mathrm{W}}/_{\mathrm{cm}^2} \le \bar{q}''_w \le 77\ {}^{\mathrm{W}}/_{\mathrm{cm}^2}$;

$109.9\ \mathrm{kPa} \le p_0 \le 122.5\ \mathrm{kPa}$

Non-dimensional Data Range

$0.55 \le X_{in} \le 0.62$

$740 \le Re_{L-in} \le 1158$

$26375 \le Re_{V-in} \le 31447$

$0.000674 \le {}^{\rho_V}/_{\rho_L} \le 0.000748$

$0.03017 \le Ja \le 0.057$

$1.665 \le Pr_L \le 1.83$

$0.0427 \le {}^{\mu_V}/_{\mu_L} \le 0.0471$

$43466 \le Re_{Total} \le 56043$

The data set in Table 2 involve smaller vapor velocities and mass flux G relative to the range covered in Table 1.

In a sense, the data in Table 1-2, since they both correspond to the some “method of heating” (see Figure 3.2) with a slightly different focus on mean-flux G range of variations can be combined to say that the reported experiments cover the following data-set:

Raw Data Range

$82\ {}^{\mathrm{kg}}/_{(\mathrm{m}^2-\mathrm{s})} \le G \le 200\ {}^{\mathrm{kg}}/_{(\mathrm{m}^2-\mathrm{s})}$;

$10\ {}^{\mathrm{W}}/_{\mathrm{cm}^2} \le \bar{q}''_w \le 80\ {}^{\mathrm{W}}/_{\mathrm{cm}^2}$;

$106.5 \text{ kPa} \leq p_0 \leq 122.5 \text{ kPa}$

Non-dimensional Data Range

$0.55 \leq X_{in} \leq 0.75$

$613.43 \leq Re_{L-in} \leq 1169.43$

$26375 \leq Re_{V-in} \leq 48317$

$0.000654 \leq {}^{\rho_V}/_{\rho_L} \leq 0.000748$

$0.01981 \leq Ja \leq 0.06076$

$1.665 \leq Pr_L \leq 2.06$

$0.0374 \leq {}^{\mu_V}/_{\mu_L} \leq 0.0494$

$43466 \leq Re_{Total} \leq 74288$

The details of the hardware for the test-section in Figure 3.1 involve careful considerations of the flow-channel (made of copper), its housing (made of stainless steel), placement of various sensors, arrangement and design of the 3 heaters, a transparent top (sight glass), and flow inlet to the housing (with a separator plate). These details are described in section A.1 of Appendix A.

The test-section in Figure 3.1 is divided into three region: (i) Inlet ($0 \leq x \leq x^*$) where incoming sub-cooled (about 1-2 °C below saturated temperature) liquid flow becomes approximately saturated, (ii) The annular regime saturated flow-boiling ($x^* \leq x \leq L^*$), and (iii) The exit zone ($x \geq L^*$). The length x^* is typically quite small because of the large heat-fluxes imposed on the boiling-surface and is approximately given by:

$$x^* \cong \frac{\dot{M}_{L_{in}} * C_{pL} * (T_{sat}(p_0) - T_{in})}{q''_w|_{in-av} * w} \tag{3.1}$$

Where T_{in} the liquid temperature is the inlet, w is the channel width, and $q''_w|_{in-av}$ is the approximate average heat-flux in the inlet zone. Actual estimates of x^* and L^* are best obtained by obtaining x-variations of the local 1-D HTC h_x (see discussion in section 3.3.2). The wattage driving the heaters in Figure 3.1 - as described in section A.1 of Appendix-A

-is feedback controlled to maintain prescribed constant temperature on top of the heater blocks. This keeps the average boiling-surface temperatures values limited to a safe range of $5\ ^\circ\mathrm{C} \leq \Delta\bar{T} \leq 30\ ^\circ\mathrm{C}$ and also avoids critical heat-flux issues. This safe arrangements leads to a non-uniform "method of heating" reported in Figure 3.2.

The test-section in Figure 3.1 also records two absolute pressures (through transducers APT-1 and APT-2) and a (DPT). The locations of the tap differential pressure in Figure 3.1 are sufficiently close to the inlet and the exit - and can be assumed to approximately correspond to $x \cong x^*$ and $x \cong L^*$.

3.2 Experimental Flow-loop and its Operations and Controls Procedure

The test-section in Figure 3.1 is located in the flow-loop shown in Figure 3.3. The photograph of the main parts of the flow-loop hardware associated with Figure 3.3 is shown in Figure 3.4.

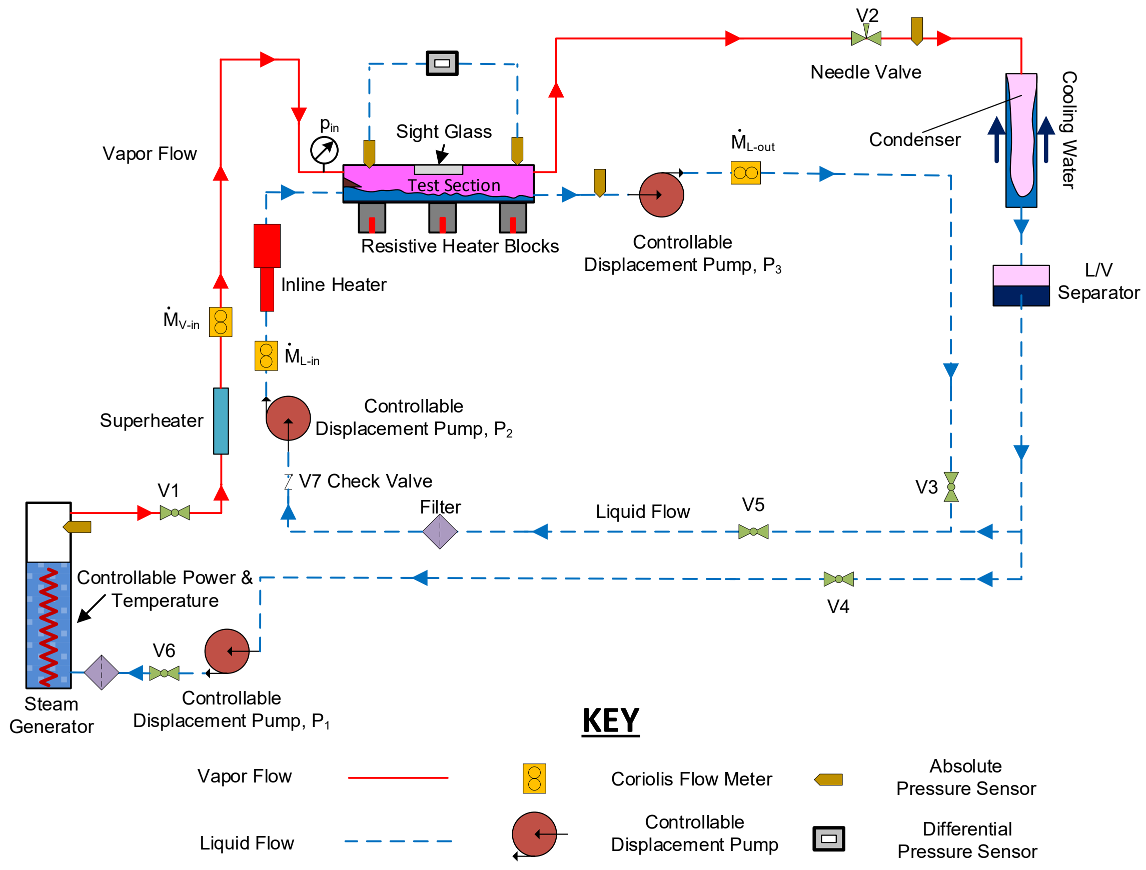

Figure 3-3 Flow loop details and components

Figure 3-4 The flow loop test stand and equipment

Required separate flows of vapor and liquid enter the test-section in Figure 3.3 at desired mass flow rates (defining inlet flow quality), pressure and temperature. Pump P_1 is a rotary vane manual speed control pump which supplies, approximately, the necessary mass flow rate to keep the steam generator liquid supply at the desired level. Pumps P_2 (gear pump) and P_3 (peristaltic pump) are computer controlled variable speed pumps. Pump P_2, along with the “Inline Heater” in Figure 3.3’s liquid line, supplies slightly subcooled (by 2-3 °C and is considered “close to saturated”) liquid to the test-section inlet (underneath the splitter plate) at a desired mass flow rate. Pump P_3 at the exit of the test-section is for further adjusting the outlet liquid mass flow rate and keeping it compatible with the liquid boiling rate (based on estimates of the total heat input that goes towards phase-change) in the test section. A total of three Coriolis Flow Meters (CFM), one flow-meter each at liquid and vapor inlets, and one at the liquid outlet - give the mass balance estimate (under steady operating conditions) of the exiting vapor flow rate. Steam Generator is responsible for supplying the desired vapor flow rate to the test section. LabVIEW program controls the heater inside the steam generator through pulse-width-modulation to supply-power – this also helps keep the exiting steam at desired temperature and pressure. A thermocouple and an absolute pressure transducer are installed within the steam generator – and they allow continuous monitoring of the temperature and pressure values of the exiting steam. Inside the "Superheater" shown on the exiting steam line (downstream of the Steam Generator) in Figure 3.3, there are two heaters (one immersion type within the tube and one resistive type surrounding the tube) that are installed. These are PID controlled heaters which make sure the vapor is superheated by 2-3 °C before it enters the test-section near the desired value of inlet pressure. The condenser is a shell and tube counter flow heat exchanger which condenses the outlet vapor from the test section back into a liquid – this cooling of the condenser is done by cold water supply (labeled as "Cooling Water" in Figure 3.3). A Liquid-Vapor separator (L/V separator) after the condenser ensures an all liquid exit (and allows for condensing into liquid any remaining vapor). Further details about the hardware are described in of Appendix-A. National instrument hardware, and a desktop PC as described in of Appendix-A, are the hardware used for data acquisition. LabVIEW (version 2016-32bit) software is implemented to control (send a signal) and acquire (receive signal) data through the hardware and sensors. Further details of instrumentation, experimental hardware, software and accuracies are also available in Appendix-A.

3.2.1 Procedure and Operations

Before starting the system up, the setup is purged to a low vacuum pressure (about 1 kPa absolute) - to make sure that, initially, most of the non-condensable gases are out of the loop. Then steam generator is started up to create steam flow across the whole flow-loop. This gradually increases the system pressure and temperature. At the same time, pumps start feeding liquid water to the steam generator to avoid any dry-out in that component. When the system pressure surpasses the atmospheric pressure, the system is pressure-purged several times to makes sure the system is more or less completely out of non-condensable (a fact ascertained by the fact that inventory temperature and pressure values in the Steam Generator are consistent with saturation table for water). When both liquid and vapor flows into the test-section are established, the test-section heaters are gradually turned on to start boiling off the liquid in the two-phase flow channel. When both test-section (including its heaters) and flow-loop are operating at steady-in-the-mean conditions, data for specific test cases are acquired. Each steady test case run is for about 10 minutes, during which it is made sure (through all the sensed data) that the test section and the flow-loop are operating steadily. For each case, flow rates, pressures, temperatures, and heat flow rates are adjusted at a specific desired value.

To achieve the steady-in-the-mean operations, pump P_1 sucks the liquid from the Liquid/Vapor separator after the condenser and from the liquid line after the valve V_4 and feeds the liquid into the steam generator. Vapor exiting the steam generator goes to the test-section inlet above the separator plate shown in Figure 3.3. Gear pump P_2 supplies the test-section with inlet liquid at the desired flow rate, which is coming from a combination of the test section outlet and Liquid/Vapor separator. This liquid goes underneath the separator plate installed at the inlet of the test-section. There is a filter installed before pump P_3 to prohibit any particle from going into the gear pump P_2 or the test-section. The liquid in the test-section does not completely boil off, so peristaltic pump P_3 is used to adjust the liquid outlet flow rate after the stagnation chamber - at the outlet of test-section (see Figure 3.3) – implemented in a way that no vapor is allowed into the liquid line out of the stagnation chamber and liquid is not allowed into the vapor exit line. There are several flow visualization sigh-glasses installed at critical locations of the flow-loop to visually make sure that at the desired location the flow is fully liquid or vapor, as per requirements of the operations. The flow visualization sight-glasses are installed at: 1- inlet of the steam generator (to ascertain and ensure only liquid flow is being fed to the generator). 2- liquid outlet of the test sections stagnation chamber (this is to make sure that only the liquid phase is coming out of that line). 3- vapor outlet of the test section’s stagnation chamber (this is to verify that there is no liquid going out through that line). 4 - before the gear pump P_2 to make sure that only liquid is continuously supplied into the gear pump.

It suffices to note here that, besides dedicated PID controls for the Steam Generator, Inline Heater, and Superheater (which includes inlet pressure p_0) in Figure 3.3, the principle PID controls are for the mass flow rates $\dot{M}_{L-in}, \dot{M}_{V-in}$, and $\dot{M}_{L-out}$ as per discussions above. Further details for this section are described in Appendix-A.

The reported data in Tables 1- 2 are for the set of experimental runs for which it was visually verified (pictures/operations from the transparent top) that the flow was annular (or misty annular) over the length of interest: $x^* < x < L^*$.

3.3 Description of Acquired and Processed Data

The acquired and processed data resulting from basic data analyses are reported in Tables 1 (A-B) and 2 (A-B). In the Tables, different case numbers characterize different experimental runs. Each set of data indicates an approximately unique set of experimental conditions that were at steady state for at least about 60 minutes. Over this duration, real-time monitoring made sure that all sensed values of system variables (consisting of the test section and the flow-loop) were nearly steady. Furthermore, the saturation conditions corresponds to pure liquid./vapor of water with negligible non-condensable air. This was ensured by start-up (system purged to close perfect vacuum) and pressure purging processes followed by test for saturation condition attainments in the stagnant zones of the flow-loop (steam generator and L/V separator in figure 3-3). Within this duration, for 10 minutes, all the sensors' data (temperatures, pressures, flow rates, pump speeds, heat fluxes, heater powers, etc.) were acquired and saved at a sampling rate of 100 Hz (100 samples per second). Subsequent steady and dynamic data analyses use these saved data.

Three types of data fall into two categories. One category consists of directly measured variables (such as some listed in the headers of Tables 1-A and 2-A and some not listed there but still needed for obtaining the values of many computed variables – such as the ones reported in Tables 1B and 2B). The other category consists of a computed variable – which are of two types. One type of computed variable arises from explicit formulas that utilize values of measured or known variables. The second type of computed variables are obtained here from ANSYS Fluent based computational solutions (of partial differential equations) – e.g. local values of Heat Transfer Coefficient (HTC) h_x and overall average HTC (h) - which employ experimentally measured variables as boundary conditions.

3.3.1 Simulations based on synthesis with experimental data

This section describes the modeling/simulations approach implemented, with the help of ANSYS Fluent software version 2018, to obtain local x-dependent values of Heat Transfer Coefficient (HTC) h_x that arise from one-dimensional width-averaged modeling of annular flow-boiling depicted in Figure 3.7 (a).

The simulation tool uses a 3-D conjugate conduction-convection analysis for the entire flow-system (see schematic in Figure 3.5 where dashed and dotted lines represent system boundary). In addition, separate conduction-convection analyses are implemented on Ansys-Fluent for each of the three cartridge heaters (see a schematic of a representative cartridge heater in Figure 3.6 a and b). The entire system consists of a copper channel (see Figures. 3.5, and its schematic is Figure3.7 (a)), three heater cartridges, and the enclosure (divided, for analyses' convenience, into top and bottom parts). The top part of the enclosure is made of steel housing (with a transparent sapphire top) that encloses the sides and the top of the channel (the dashed line in Figure 3.5 is its boundary). The bottom part of the enclosure is made of the cartridge heaters and some exposed part of the channel's bottom (the boundary of this bottom part of the enclosure is marked by the bottom line in Figure 3.5). With the help of Figure 3.8, which is a schematic of the heated boiling-plate (that constitutes the horizontal bottom of the channel in Figure 3.7(b)), the essential ideas underlying the conjugate analyses – which yield the sought for local values of hx – are discussed next.

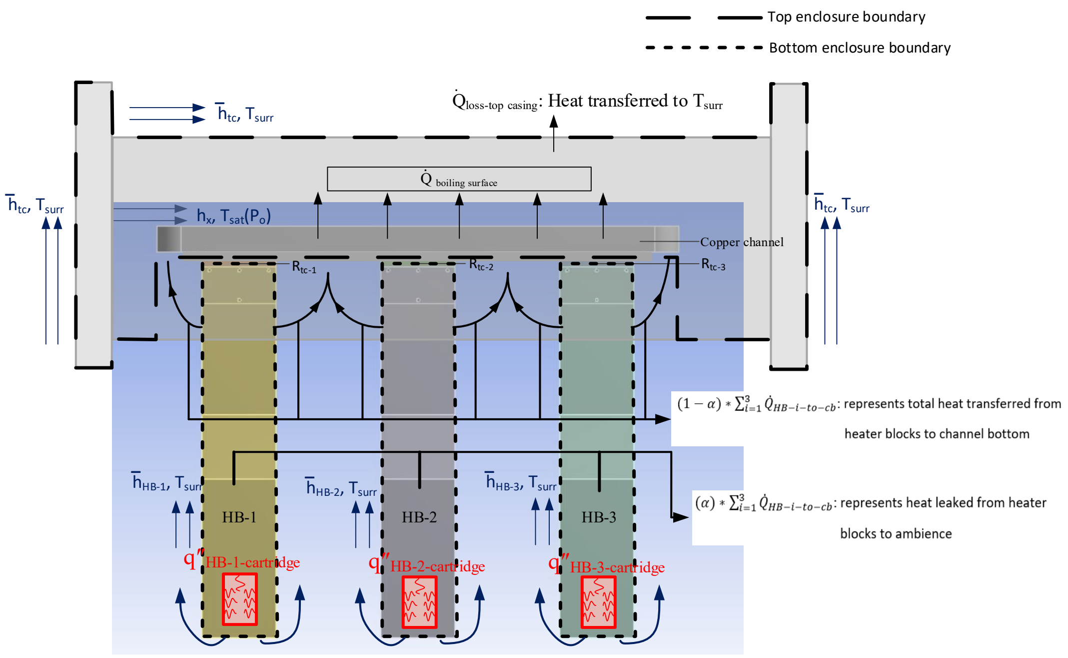

Figure 3-5 Entire flow-system geometry - with marked variables that are defined in this section and in section A.3 of Appendix-A. The view is of a vertical plane cross-section that is parallel to the length of the channel and goes through the middle of the channel-width.

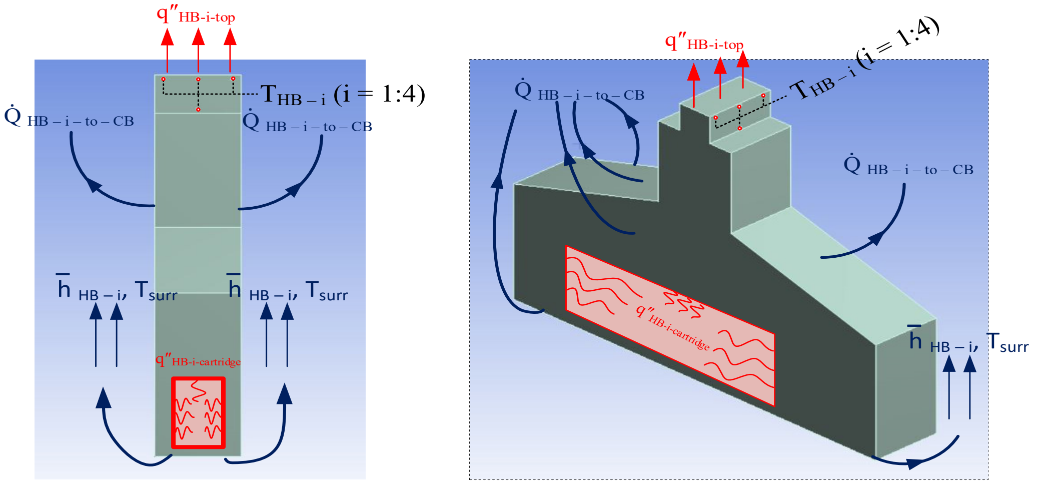

(a) (b)

Figure 3-6 (a) The side view of a representative heater block cartridge i (i = 1 to 3) with the depiction of utilized boundary conditions. **(b)** The isometric view of the same

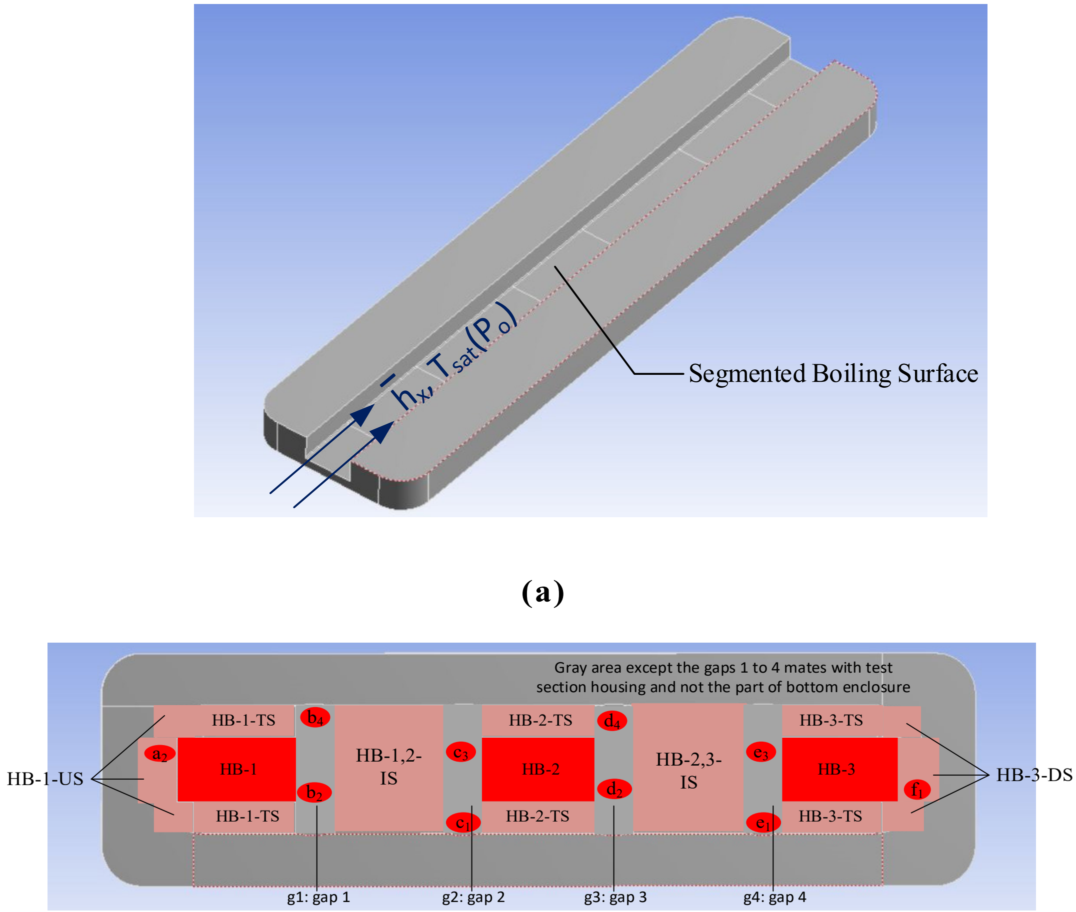

(a)

(b)

Figure 3-7 (a) The copper channel hardware's top – with groove forming the channel. The boiling-surface on the bottom of the groove in this picture experiences convection thermal boundary condition shown in Figure 3.8. This means for the top surface in Figure 3-8 $T_{sat}(p_0)$ and h_x has to be supplied. *The remaining three surfaces in the groove of this picture are adequately modeled as adiabatic or known surface-temperature ones*. (b) The copper channel hardware's bottom surface (red and peach color) is shown with marked surfaces of interest that are used for heat-flux calculations. Red circles represent measured temperatures.

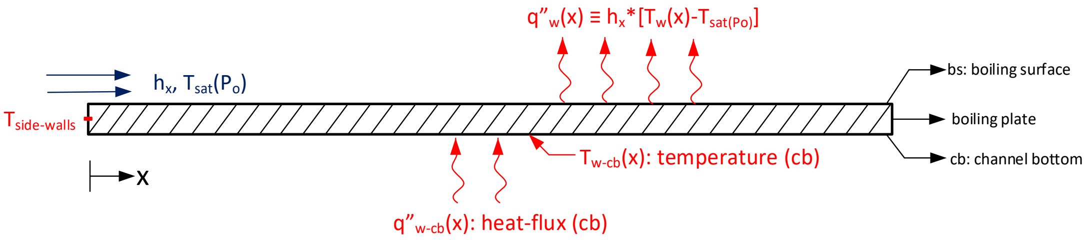

Figure 3-8 A schematic of the boiling-plate underneath the channel groove in Figure 4(a).

Note that the heater cartridges (Figure 3.6) and the complete system (Figure 3.5) have some known and some unknown thermal boundary conditions that must also factor in obtaining reasonable modeling estimates of the heat-leakage rates from the top and bottom parts of the enclosure in Figure 3.5. The modelling/simulations also relate to thermal contact resistances between the cartridge heaters and the channel-bottom (cb) of the boiling-plate shown in Figure 3.7 b (marked R_{tc1} to R_{tc3} in Figure 3.5). It suffices to note here that these conduction-convection analyses for the heater cartridges (Figure3.6) and the complete system (Figure 3.5) effectively yield both the channel bottom heat-fluxes and temperatures denoted, respectively, as $q"_{w-cb}(x)$ and $T_{w-cb}(x)$in Figure 3.8. The temperatures at the two side edges and front and back edges of the boiler-plate in Figure 3.8, representatively marked as $T_{side\text{-}walls}$, are also effectively obtained/modeled. The top boiling-surface's width-averaged one-dimensional convection boundary condition in Figure 3-8, viz. $q''_w(x) \equiv h_x.[T_w(x) - T_{sat}(p_0)]$ with $T_{sat}(p_0)$ known and h_x unknown, requires imposition of a guessed profile for hx. But it is well known that for steady conduction analysis of the boiler plate in Figure 3.8 (which is part of the system in Figure 3.5), one only needs one of the two known channel-bottom (cb) thermal boundary conditions of: heat-flux $q"_{w-cb}(x)$ or temperatures $T_{w-cb}(x)$ in Figure 3.8. This extra information at channel bottom is however available (see Appendix B) and this allows us to guess, iterate, and converge to the correct h_x values for the boiling-surface in Figure 3.8. The details of the simulations and algorithms leading to converged h_x values are described in Appendix-B.

A sample result for case 7 in Tables 1(A-B) yields the h_x versus x curve, as shown in Figure 7 below.

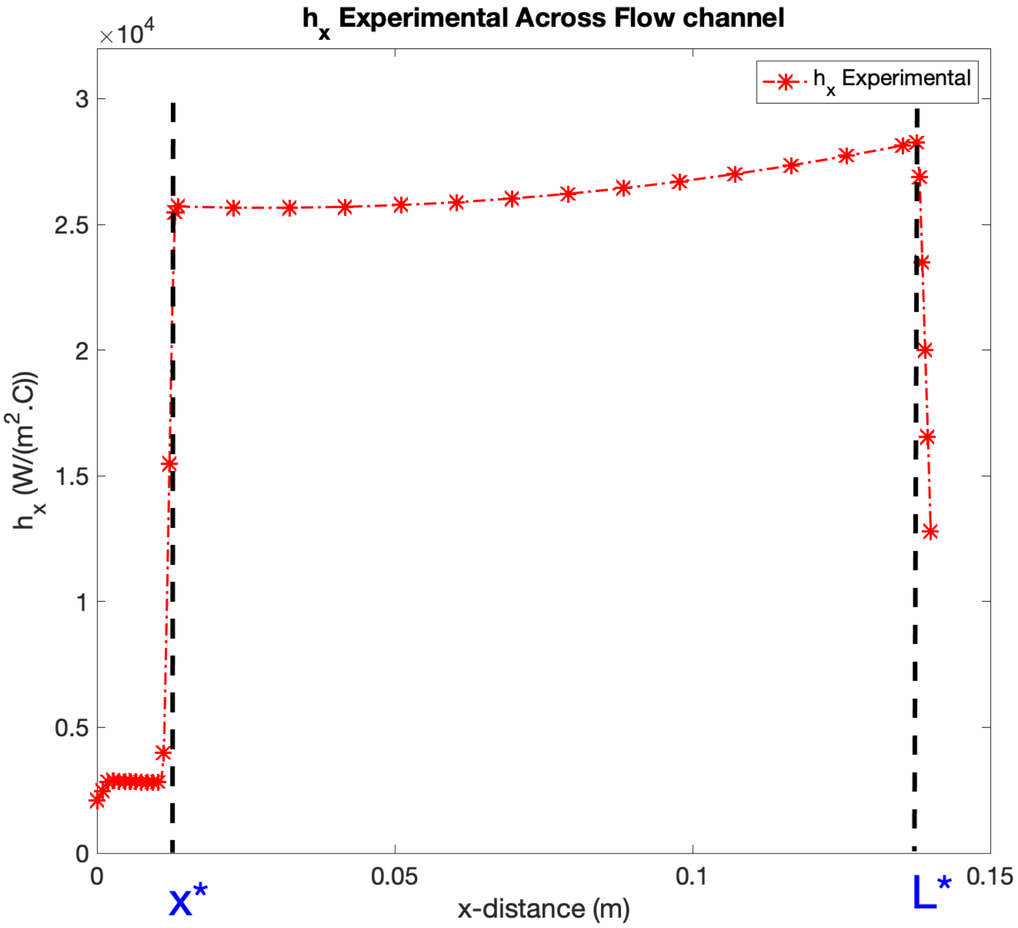

Figure 3-9 Local HTC h_x versus distance curve as obtained for case 7 in Table-1. The distances x* and L*, as marked above, take into account earlier discussions and estimates – including the predicted profiles for the boiling-surface temperatures and heat-flux values, respectively denoted

Appendix-B describes – in greater detail – the simulation procedure and results that ascertain the boundary conditions in Figure 3.8. The process involves direct use of some known measured values of temperatures and some measured, but not directly used values of temperatures. The temperatures that are not used to estimate boundary conditions are also predicted. And then used indirectly by obtaining certain quantities such as the sum of the square "errors" of respective differences between the two sets of measured and predicted temperatures. The algorithm proceeds towards minimizing the "errors."   An agreement (within ±0.5°C) was achieved between these experimentally measured and predicted temperatures. Estimated values of certain thermal contact resistances and overall heat-leakage rates (related to guessed convection coefficients ($\bar{h}_{tc}$, $h_{HB\text{-}I}$, leakage-factor α) are verified to have approximately the same values for different experimental test runs for Tables 1 and 2 for any representative choice of T_{sat} and T_{surr} (number choices for T_{sat} and T_{surr} are guided by representative experimentally measured values; inlet test-section pressure and saturation tables for T_{sat} and a single-location surrounding air-temperature for T_{surr}). It should be noted that the accuracy of predicting $q''_{W-cb}(x)$ and T_{W-cb} in Figure 3.8 alone are important and inaccuracies in predicting other variables such as $h_{HB\text{-}i}$ ($i = 1$ to 3), h_{tc}, α, etc. in Figures 3.5 to 3.6 are of secondary importance as long as those estimations do not affect the noted boundary conditions in Figure 3.8. Also, the overall heat-flow rate into the flow-boiling test-section, as obtained by these simulations, are verified to be consistent with experimental data for inlet and outlet flow rates (as measured by Coriolis flow meters) and energy balance for flow-boiling. The consistency with supplied heat into the cartridges arise– by design – from the algorithm that defines heat-flux $q''_{HB\text{-}cartridge\text{-}i}$ in Figure 3.5 which acts around the cavities for the heater cartridges. In 3-D energy balance (implemented on ANSYS, for the test-section and its enclosure in Figure 3.5), *the computed numbers* for boiling-surface heat-flux and measured inlet/outlet mass flow rates are also consistent with the heat inputs for the heater blocks, as measured by power-meters (watt-meter) and relevant heat-leakage rates. This is further discussed in chapter 4. A difficult part of the simulation – thanks to the work done by Harsha Sathi for his MEEM 5990 Special Topics course in support of this thesis – involved importing of all the complex geometry into the ANSYS workbench – from already existing precise 3D CAD models. ANSYS meshing software is also used to discretize the geometry, edge refinement is implemented to capture thermal concentration at curvy contact regions and holes, and solutions are verified to be mesh-size independent.

3.4 Uncertainty Analyses and Uncertainty in Reported Data

As mentioned earlier, this thesis reports four types of data in two categories. And this section describes a method for ascertaining and reporting the uncertainty in these data.

Measured variables

One category of data consists of directly measured steady time-averaged values of variables, denoted as a set $\{Y_{m\text{-}i}\}_{i=1 \text{ to } I}$ (where “i” is an integer – a counting index - for up to “I” variables). For example, $\{Y_{m\text{-}1} \equiv \dot{M}_{Lin}, Y_{m\text{-}2} \equiv \Delta p,\ Y_{m\text{-}3} \equiv Temp_{k=k^*}, \ldots\}$ are some of the variables listed in the headers of Tables 1A and 2A. Here "$\{Temp_k\}$" denotes all the measured temperatures described for Figures 3.3 and 3.5 of section 3.3 – which are used (along with other measurements) in the calculation of boiling-surface temperatures $T_w(x)$ indicated in Figure 3.8. Note that “m” is not a counting index – it stands for a measured variable. These also include some measured/ascertained variables that are not listed in Tables 1-A and 2-A, but are needed for obtaining the values of many computed variables reported in Tables 1-B and 2-B – e.g., the rate of heating of a heater block (i = 1 to 3) by a cartridge heater, $\dot{Q}_{cartridge\text{-}heater\text{-}i}$, temperatures $\{Temp_k\}$ measured at other locations including those shown in Figure 3-3, 3-5 and 3-8. The saturation temperature $T_{sat}(p_0)$, etc. The total estimated uncertainty in each of these measured variables – which are independent and uncorrelated to each other – are denoted as $\delta Y_{m\text{-}i}$. The sensor accuracies, bias (if any), and calibration related uncertainties associated with $\delta Y_{m\text{-}i}$ are denoted as $\delta Y_{m\text{-}i}|_{fixed}$. For thermocouples, pressure transducers, etc. measurements, in-house calibrations were used (with the help of thermometers and manometers) to establish or improve upon vendor ascertained values of $\delta Y_{m\text{-}i}|_{fixed}$. However, for some high-quality calibrations coming with manufacturer assurance (Coriolis meters, etc.), the recommended calibrations for $\delta Y_{m\text{-}i}|_{fixed}$ were used after simple verifications involving order of magnitude testing. Some of these fixed uncertainties were estimated in absolute terms, e.g. $\delta Temp_k|_{fixed} = \pm 0.5°C$, and some in relative terms, e.g. $\delta q''_{cartridge-heater}/q''_{cartridge-heater} \cong \pm 0.015$.

The total uncertainty $\delta Y_{\text{m-i}}$ consists of $\delta Y_{\text{m-i}}|_{\text{fixed}}$ plus any statistically random uncertainty associated with obtaining ten minutes of time-averaged values of variables $Y_{\text{m-i}}$, and is defined as [2]:

$$\delta Y_{\text{m-i}} \equiv \delta Y_{\text{m-i}}|_{\text{fixed}} + t_{95} \cdot S_{Y_{\text{m-i}}} \qquad (3.2)$$

In the equation above, "$t_{95} \cdot S_{Y_{\text{m-i}}}$" is a standard error (on the mean $Y_{\text{m-i}}$) multiplied by a factor. In this expression, typically the factor t_{95} relates to a 95% confidence interval associated, typically, with t-distribution for the data set under consideration and $S_{Y_{\text{m-i}}}$ is estimated as standard error – which is standard deviation divided by $\sqrt{N}$). For 10 minutes of data at a sampling rate of 100 Hz, $N \cong 6 * 10^4$, and the distribution is nearly Gaussian. As a result $S_{Y_{\text{m-i}}} \cong 0$, and:

$$\delta Y_{m-i} \cong \delta Y_{m-i}|_{\text{fixed}} \qquad (3.3)$$

for all the measured variables considered here.

The above procedure is used to compute relative uncertainties reported for all the measured values data in Tables 1-2.

Calculated variables

The other category of data reported here consists of computed variables $\{Y_{\text{c-j}}\}_{j=1 \text{ to } J} \equiv \{Y_{\text{c-1}}, Y_{\text{c-2}}, Y_{\text{c-3}}\}$ which are further subdivided into three sets $\{Y_{\text{c1-j}}\}_{j=1 \text{ to } J1}$, $\{Y_{\text{c2-j}}\}_{j=1 \text{ to } J2}$, and $\{Y_{\text{c3-j}}\}_{j=1 \text{ to } J3}$. Here subscript "c" stands for calculated variables and subscripts "c1-j" to "c3-j" denote the categories (1 to 3) of calculated variables that are further described below.

Calculated variables of the first type

The first type of computed variables $\{Y_{\text{c1-j}}\}_{j=1 \text{ to } J1}$, such as $\{Y_{\text{c1-1}} \equiv Re_{L_{in}}, Y_{\text{c1-2}} \equiv Re_{V_{in}}, Y_{\text{c1-3}} \equiv X_{in}, \ldots\}$ in Tables 1B-2B of section 2, typically arise from explicit formulas that utilize sums of one or more terms named $\{PY_{m\text{-}i}\}$, where "i" is a counting index $1 \leq i \leq IP$. Each of the terms $PY_{m\text{-}i}$ typically utilize one or more measured variables $Y_{m\text{-}i}$ and are in the power law form of the type:

$$PY_{m\text{-}i} = Y_{m-1}{}^{bi-1} \cdot Y_{m-2}{}^{bi-2} \dots Y_{m-IP}{}^{bi-I} = \prod_{k=1}^{IP} Y_{m-k}{}^{bi-k} \qquad (3.4)$$

where i = 1 to IP are integers – with "IP" denoting the number of power-law terms – and {bi-k} (with i = 1 to IP and k = i = 1 to I) being real numbers with zeroes allowed to accommodate number of Y_{m-k} terms being less than IP. Recall that "m" is not a counting index – it stands for "measured" variables.

Furthermore, calculated variables of the first type are of the form:

$$Y_{c1\text{-}j} = a_{j1}PY_{m\text{-}1} + a_{j2}PY_{m\text{-}2} + \cdots a_{jI}PY_{m\text{-}IP} = \sum_{i=1}^{IP} a_{ji}PY_{m\text{-}i} \qquad (3.5)$$

where $\{a_{ji}\}$ are real numbers, with j = 1 to J1 and i = 1 to iP being integers. It is known (see [3]), that the uncertainty $\delta Y_{c1\text{-}j}$ for the term on the left of Equation (3.5) is related to uncertainties $\delta PY_{m\text{-}i}$ of the power law terms $\{PY_{m-i}\}$. The relationship is given by:

$$\delta Y_{c1\text{-}j} = \left[\sum_{i=1}^{iP} (a_i \cdot \delta PY_{m\text{-}i})^2\right]^{\frac{1}{2}} \qquad (3.6)$$

and the uncertainties $\delta PY_{m\text{-}i}$ associated with the power law expressions in Equation (3.4) are given as:

$$\frac{\delta PY_{m\text{-}i}}{PY_{m-i}} = \left[\Sigma_{k=1}^{IP} \left(\frac{b_{i-k} \cdot \delta Y_{m\text{-}k}}{Y_{m-k}}\right)^2\right]^{\frac{1}{2}} \qquad (3.7)$$

The above procedure is used to compute relative uncertainties for the first type of computed variables and report them in the headers of Tables 1-2.

Calculated variables of the second type

Examples of calculated variables of the second type in Tables 1B-2B and elsewhere in section 2 are $\{Y_{c2\text{-}j}\}_{j1=1\text{ to }J2}$ such as $\{Y_{c2\text{-}1} \equiv h_x,\ Y_{c2\text{-}2} \equiv q''_w(x),\ \ldots\}$. These variables are calculated with the help of Ansys FLUENT software by procedures described in section 3.3.1 and Appendix B. These variables are computed from supplied boundary conditions that eventually arise from measured or known variables such as $\{Y_{m\text{-}i}\}_{i=1\text{ to }I}$. For example, h_x values have a non-linear dependence (from the solution processes associated with underlying partial differential equations and the experimental geometry) determined by a non-linear response function R. This function R depends on key input variables (the salient ones are listed below):

$$\begin{aligned} h_x &\equiv R\left(\{\mathrm{Temp}_k\} \leftrightarrow \overline{T}_{cb}, q''_{\text{cartridge-heater}}, T_{sat}(p_0), T_{surr} \ldots\right) \\ &\equiv \frac{q''_w(x)}{T_w(x) - T_{sat}(p_0)} \end{aligned} \tag{3.8}$$

$\overline{T}_{cb}$ is a variable assigned for representing a number of measured values (out of subset $\{\mathrm{Temp}_k\}$) channel bottom temperatures for calculating uncertainty in those representative temperatures. Even though there are numerous boundary conditions involved in obtaining converged h_x values, the most influential one is the $T_{sat}(p_0)$ boundary condition implemented on the boiling surface. The variables $q''_{\text{cartridge-heater-}i}$ (i=1 to 3) and T_{surr} boundary conditions do not have a comparable (with respect to $T_{sat}(p_0)$) impact on h_x uncertainty as the computed variables on the right most side of equations 3.8. They are implemented in the solution of the boundary value problem and hence they affect the nonlinear response function R in equation 3.8. They ultimately lead to converged boundary conditions on channel bottom surface, hence they are also considered to be important in obtaining simulation uncertainty. As is known, once representative partial derivatives $R_1 \equiv \frac{\partial R}{\partial \overline{T}_{cb}}$, $R_{2i} \equiv \frac{\partial R}{\partial q''_{\text{cartridge-heater}}}$, $R_3 \equiv \frac{\partial R}{\partial T_{sat}(p_0)}$, $R_4 \equiv \frac{\partial R}{\partial T_{surr}}$, etc. are estimated by finite difference estimates - with one at a time perturbation of the salient boundary conditions - and subsequent solutions of the boundary value problems (using ANSYS Fluent as per procedure described in section 3.3 and Appendix A.3), the uncertainty δh_x in h_x is approximately given by

$$\delta h_x \cong \sqrt{\{R_1 \cdot \delta \bar{T}_{cb}\}^2 + [\sum_{i=1}^{3} \{R_{2i} \cdot \delta q''_{cartridge-heater}\}^2] + \{R_3 \cdot \delta T_{sat}(p_0)\}^2 + \{R_4 \cdot \delta T_{surr}\}^2} \quad (3.9)$$

where $\delta T_w(x)$, $\delta q''_{cartridge-heater}$, $\delta T_{sat}(p_0)$, δT_{surr}, etc. represent the already estimated measured variable uncertainties. For a sample calculation for case 7 in Table 1B, the three terms under the radical sign – on the right of Equation (3.9) - are, respectively, 0.171, 0.44, ,0.837 and 0.0016 with $\delta h_x \cong 860.02$ Equations similar to Equation (3.9) yield uncertainties in converged values of $q''_w(x)$ and $T_w(x)$.

The above procedure is used to estimate relative uncertainties in the second type of computed variables - which are then reported in Tables 1-2.

Calculated variables of the third type

Examples of calculated variables of the third type in Tables 1B-2B and elsewhere in section 2 are: $\{Y_{c3\text{-}j}\}_{j1=1 \text{ to } J3}$ with $\{Y_{c3\text{-}1} \equiv Nu_x, Y_{c3\text{-}2} \equiv \overline{Nu}, \ldots\}$. These variables are like calculated variables of the first type – the difference being that all the variables on the right side of Equation (3.4) are not measured variables $Y_{m\text{-}i}$. Some are calculated variables of the second type – for which uncertainty has already been computed (e.g. h_x in $Nu_x \equiv (h_x \cdot D_h|_H)/k_L$). Therefore the calculation procedure for these variables is the same as for the calculated variables of the first type.

REFERENCES

1. Taylor, Barry N., and Chris E. Kuyatt. "NIST Technical Note 1297 1994 Edition Guidelines for Evaluating and Expressing the Uncertainty of NIST Measurement Results." *Natl. Inst. Stand. Techno!.* (1994): 1-20.
2. Moffat, R. J. "Contributions to the theory of single-sample uncertainty analysis." Journal of Fluids Engineering 104, no. 2 (1982): 250-258.

3. Holman, Jack Philip, and Walter J. Gajda. Experimental methods for engineers. Vol. 2. New York: McGraw-Hill, 2001.

4 Results and Discussions

4.1 Results on local HTC h_x

This work, unlike most experimental works underlying or supporting development of HTC correlations ([1-7]), succeeds in conducting experiments that directly yield one-dimensional width-averaged local h_x values (see Figure 4.1) for high heat-flux experiments (for the schematic in Figure 3.1 of chapter 3) conducted for a given "method of heating." Most works ([1-7]) attempt to infer local variations of h_x with distance x by developing correlations relying on a more limited set of available information. Such available information typically consists of a set of average HTC values obtained by suitable experimental measurements over different length segments of the test-section – with or without help from a few local HTC measurements at discrete locations $x = x_1, x_2, x_3$, etc. The results, as in Figure 4.1 for data in Tables 1A-B, cover a range of parameters (see Equations (3.1) - (3.3) in chapter 3) for a representative fixed – but non-uniform – "method of heating," as defined by a "single curve" for $\theta_w(x)$ and/or $\Psi_q(x)$ shown in Figures. 3.2 a,b,c.

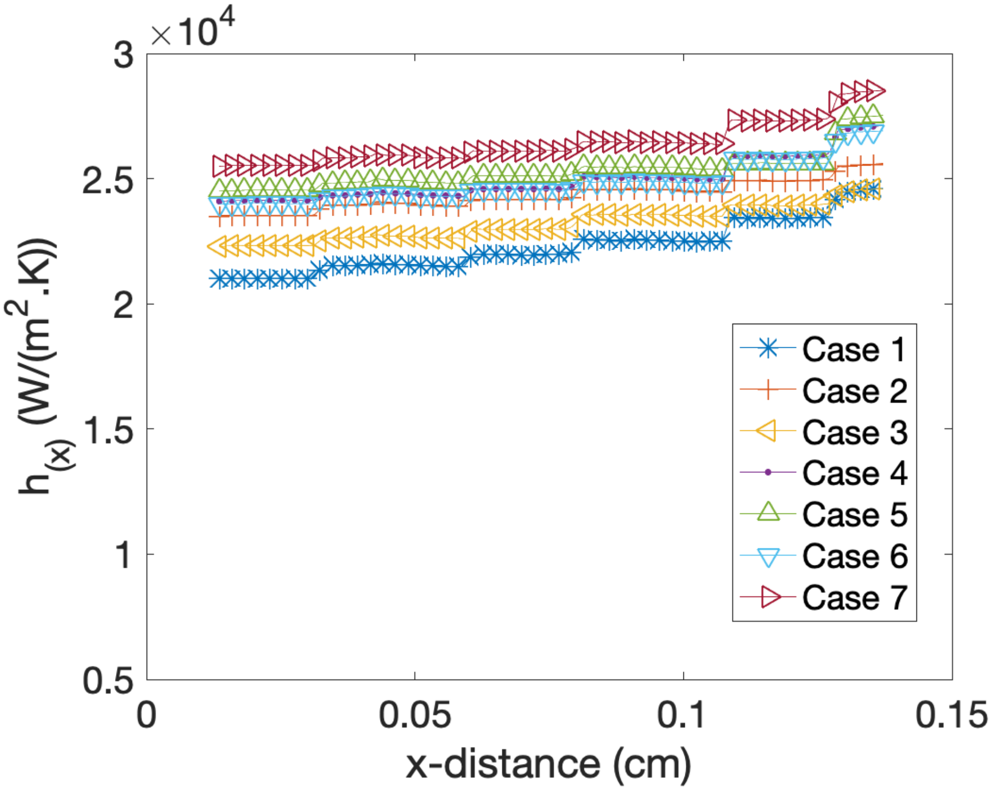

Figure 4-1: Experiments-simulations synthesis based local HTC h_x (W/(cm^2-°C) versus distance x (m) curves for cases marked in Table-1.

The experiments-simulations synthesis based local HTC h_x versus distance x curves in Figure 4.1 are for cases marked in Table-1. These values result from a first-of-its-kind sophisticated approach discussed in section 3.3.1 and Appendix B. (Similar results are available for the table 2 data set but not presented here for brevity)

4.2 Results on Quality X(x)

The integration of local 1-D energy equation in Equation (2.17), as discussed in Ch 2 and [8], yields reliable estimates of quality X(x) variations – and this is shown in Figures. 4.2 – 4.3 for the representative cases in Table 1. Figure 4.3 shows that a representative X(x) quality variation not only satisfies local energy equation but also yields values in agreement with experimentally measured inlet quality X_{in} and outlet quality X_{out}.

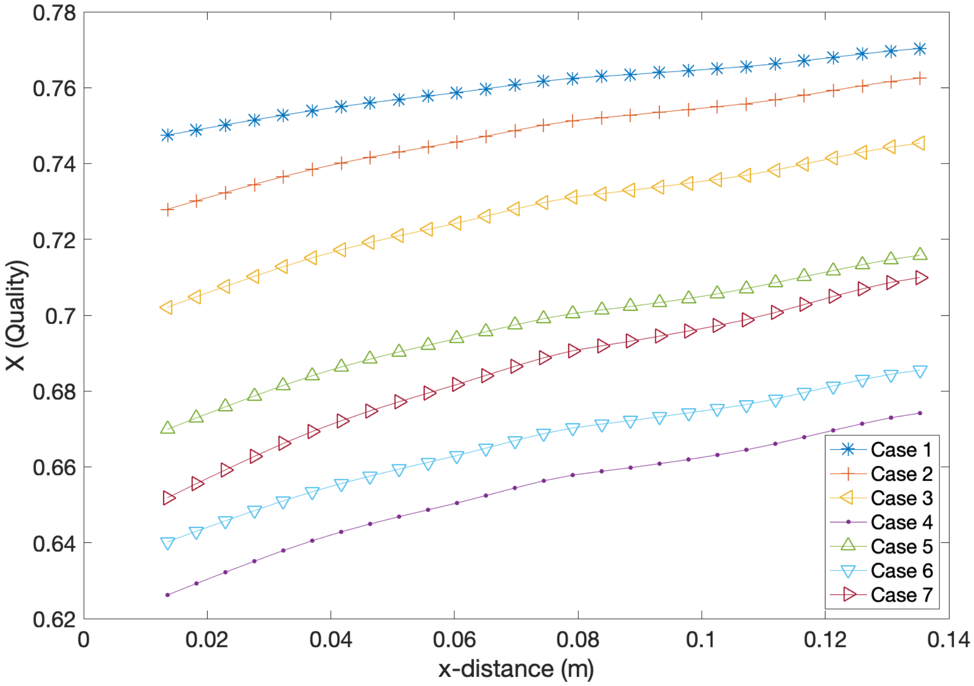

Figure 4-2: Quality X versus distance x (in m) curves for cases 1 to 7 marked in Table-1.

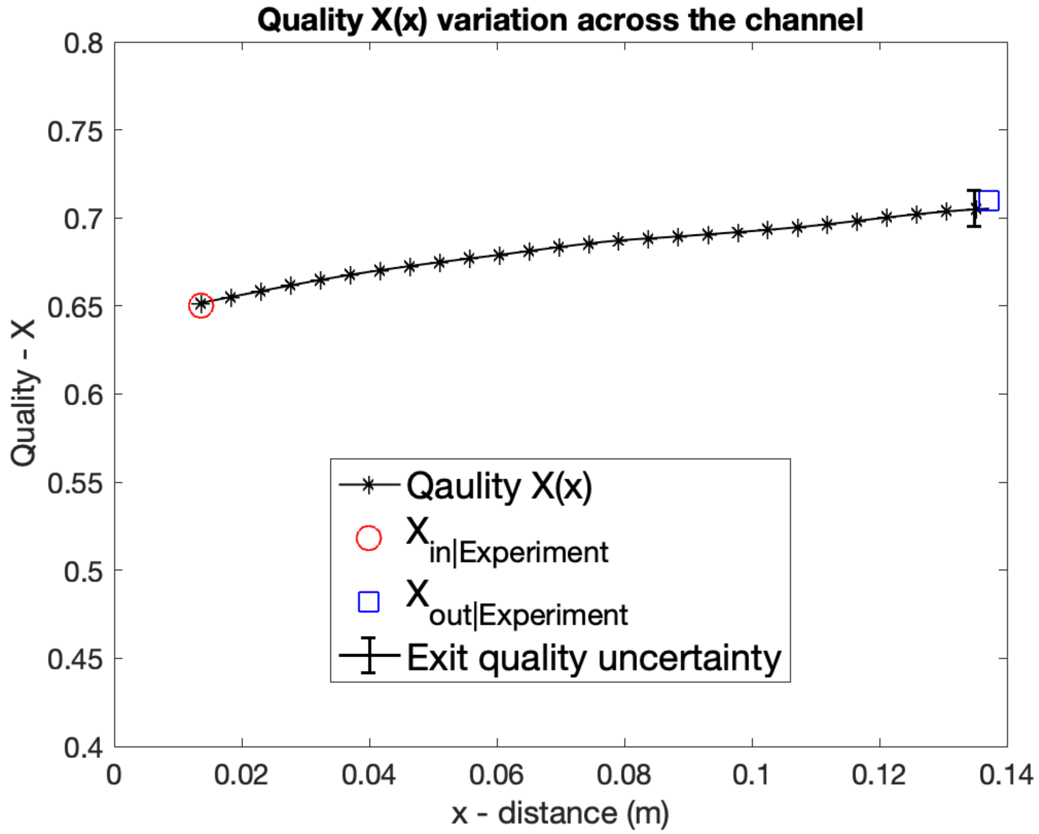

Figure 4-3: Quality X versus distance x (m) curve for a representative case 7 marked in Table-1.

4.3 Results on Local HTC in Comparison with Available Correlation Based Estimations

For the range of parameters considered in Equations (3.1) – (3.3) in section-3, assuming weak dependence on non-uniform $\theta_w(x)$ and/or $\Psi_q(x)$, the above described experimentally assessed local HTC "$h_x = h_x|_{Expt}$ versus distance x" curves in Figure 4.1 and reliable estimates of quality X(x) in Figures. 4.2-4.3, one can also obtain additional estimates of local HTC "$h_x \cong h_x|_{Corr}$" from relevant and existing HTC correlations. Such comparisons can only yield order of magnitude agreements, see discussions in [8]. For a representative case 7 marked in Table-1, Figure 4.4 shows order of magnitude agreement with curves obtained from Kim and Mudawar [1], Klimenko [2], and Dorao et al. [4] correlations. It is interesting to note that, in this parameter range, the values of $h_x = h_x|_{Exp}$

are monotically increasing with x – while local values of boiling-surface temperatures $T_w(x)$ and heat-flux values $q''_w(x)$ are on average decreasing, see Figures. 4.5 – 4.6. As discussed with the help of Equation (2.7) in section-2, this heat-exchange efficiency increase – as modeled by increasing h_x – is feasible, despite decreasing heat-flux $q''_w(x)$ values.

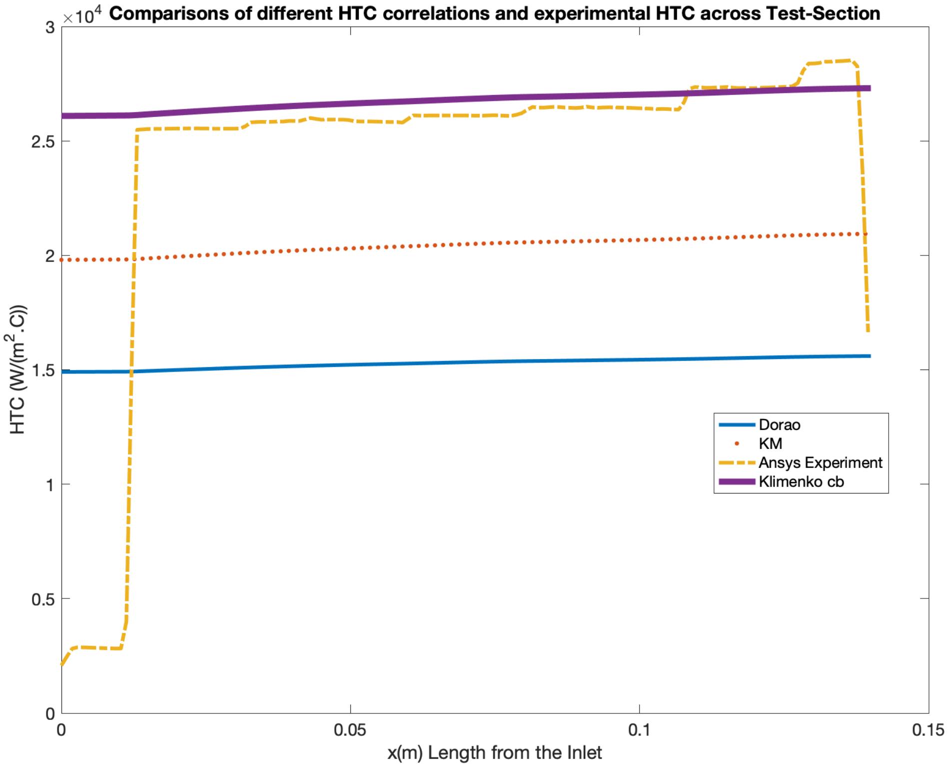

Figure 4-4: Representative h_x (W/m^2-°C) versus distance x (m) curve, obtained from experiments-simulations synthesis, for case 7 marked in Table-1. It is in order of magnitude agreement with curves obtained, for the same parameter set that defines the experimental case, from existing and representative engineering correlations for local HTC h_x.

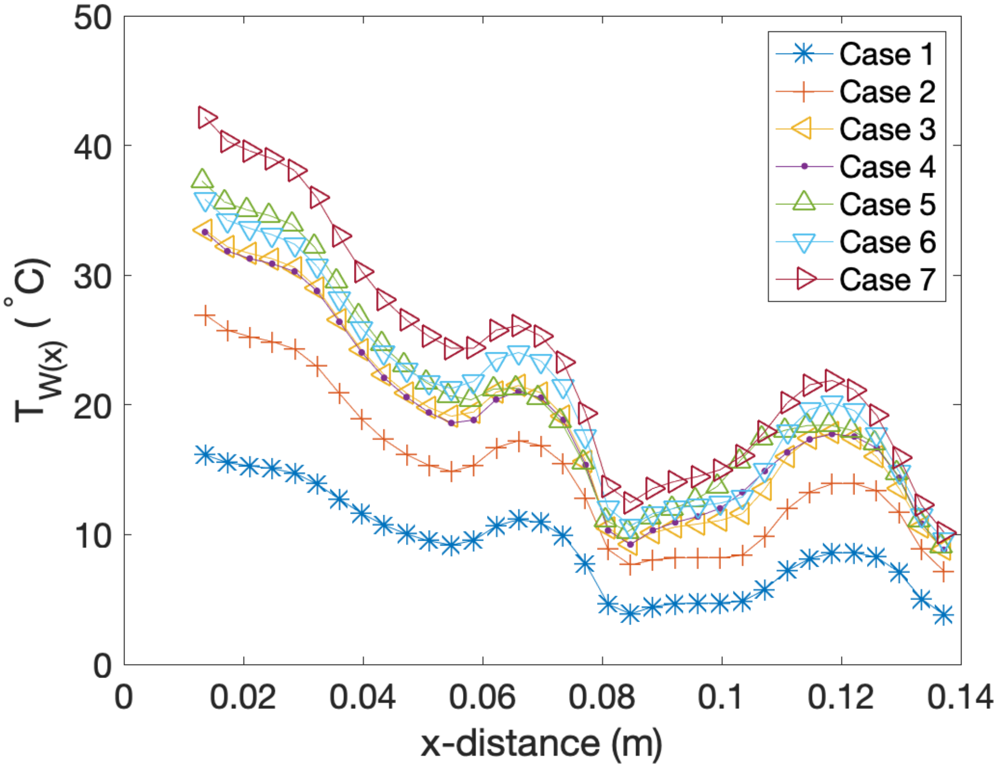

Figure 4-5: Boiling-surface wall temperature $T_w(x)$ versus distance x (in m) curve for representative cases 1 to 7 marked in Table-1.

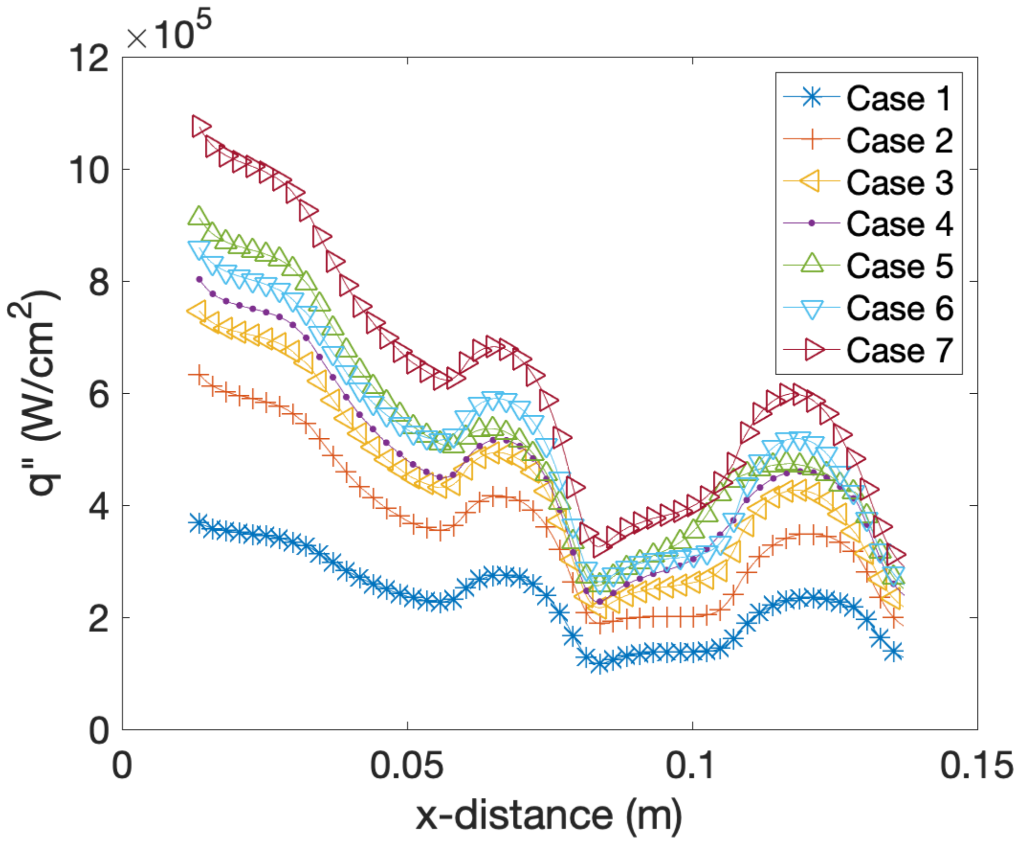

Figure 4-6: Boiling-surface heat-flux $q''_w(x)$ versus distance x (m) curve for representative case 1 to 7 marked in Table-1.

4.4 Discussion of Relationship Between Void-Fraction Models and Local Film Thickness Values

Also, as discussed in section-2, meaningful applications of void fraction correlations $\epsilon(X(x))$ – obtained from adiabatic experiments – to corresponding (locally identical values of $\dot{M}_L(x)$ and $\dot{M}_v(x)$) flow-boiling situations need to go further and require that both adiabatic and flow-boiling situations be in the same flow-regime and have known equal values at a specific $x = x^{\#}$ location. This assumes that other differences between phase-change and adiabatic flow conditions are adequately modeled by using properly computed values of varying qualities X(x) (as in Figures. 4.2 – 4.3). To ensure the above, it is proposed that all relevant void fraction correlations $\epsilon(X(x))$ be scaled by a factor to satisfy, at the inlet $x = x^* \cong 0$, the condition:

$$\epsilon^* = \frac{A_V(x^*)}{A(x^*)} \cong \frac{\left(h - \tilde{\Delta}(x^*)\right).w}{h.w} = 1 - \frac{\tilde{\Delta}(x^*)}{h} \tag{4.1}$$

In Equation (4.1), $\Delta(x^*)$ represents a local representative liquid thickness of width w in the absence of nucleation. Two relevant existing correlations ([9 -10]) are scaled to satisfy Equation (4.1) and the resulting values of void fraction $\epsilon(x)$ and approximate/effective film thickness $\Delta(x)$ – both with the recommended adjustments satisfying Equation (4.1) as well as without any such adjustments – are plotted and shown in Figures. 4.7 – 4.8. The nearly identical curves for the adjusted cases justify the above described modeling assumptions and restrictions. The proposed case-specific models for void fraction $\epsilon(x)$ and approximate film thickness $\Delta(x)$ are then represented by the average - the dotted "----" curves in Figures. 4.7 – 4.8. Then $\epsilon_{Model}(X(x))$ and corresponding $\Delta(x)$ curves – with quality X(x) as computed earlier – are given by:

$$\epsilon_{Model}\left(X(x)\right) \equiv \frac{\epsilon_{Rouhani}\left(X(x)\right) + \epsilon_{Thome}\left(X(x)\right)}{2} \tag{4.2}$$

and

$$\epsilon_{Model}\left(X(x)\right) \equiv \frac{h\text{-}\Delta(x)}{h} \tag{4.3}$$

Note that approximate/representative film thickness $\Delta(x)$ in the absence of nucleation as shown in Figure 4.8 is expected to be of the same order of magnitude as the actual film thickness $\widetilde{\Delta}(x)$ for all annular flow boiling situations in the presence of nucleation as well as for negligible entrainment rate ([11-12]) conditions. Whether or not the annular flow conditions involve negligible or non-negligible entrainment rates, as far as estimation of vapor mass flow rate $\dot{M}_V(x)$ as $\dot{M}_V(x) \equiv G \cdot A \cdot X(x)$ are concerned, X(x) computations based on phase-change (as implemented here) should be adequate. This is because entrainment rates due to mechanical ripping-off of droplets from the interface can continue to be modeled, primarily, as an adiabatic phenomena which are similarly present in the corresponding adiabatic misty annular flows. Therefore, cross-sectional liquid mass flow rate in the liquid film regions $\dot{M}_{Lf}(x)$ and actual film thickness $\tilde{\Delta}(x)$ (relative to approximate/effective film thickness $\Delta(x)$) for non-negligible entrainment rates are expected to satisfy:

$$\dot{M}_{Lf}(x) < \dot{M}_{L}(x) \equiv G \cdot A \cdot \{1 - X(x)\} \tag{4.4}$$

and

$$\tilde{\Delta}(x) < \Delta(x) \tag{4.5}$$

However for zero entrainment and significant nucleation rates (as is the case here), we expect $\tilde{\Delta}(x) > \Delta(x)$, although, in this thesis, we do not have reliable estimates of entrainment rates, visual observations from the top transparent plate suggests that, overall entrainment rate up to the test-section exit is less than 0.5% of $\dot{M}_{L-in}$. Therefore, for discussions in this thesis, one assumes the inequality in Equation (4.5) is weak, and one has:

$$\Delta(x) \approx \tilde{\Delta}(x) \tag{4.6}$$

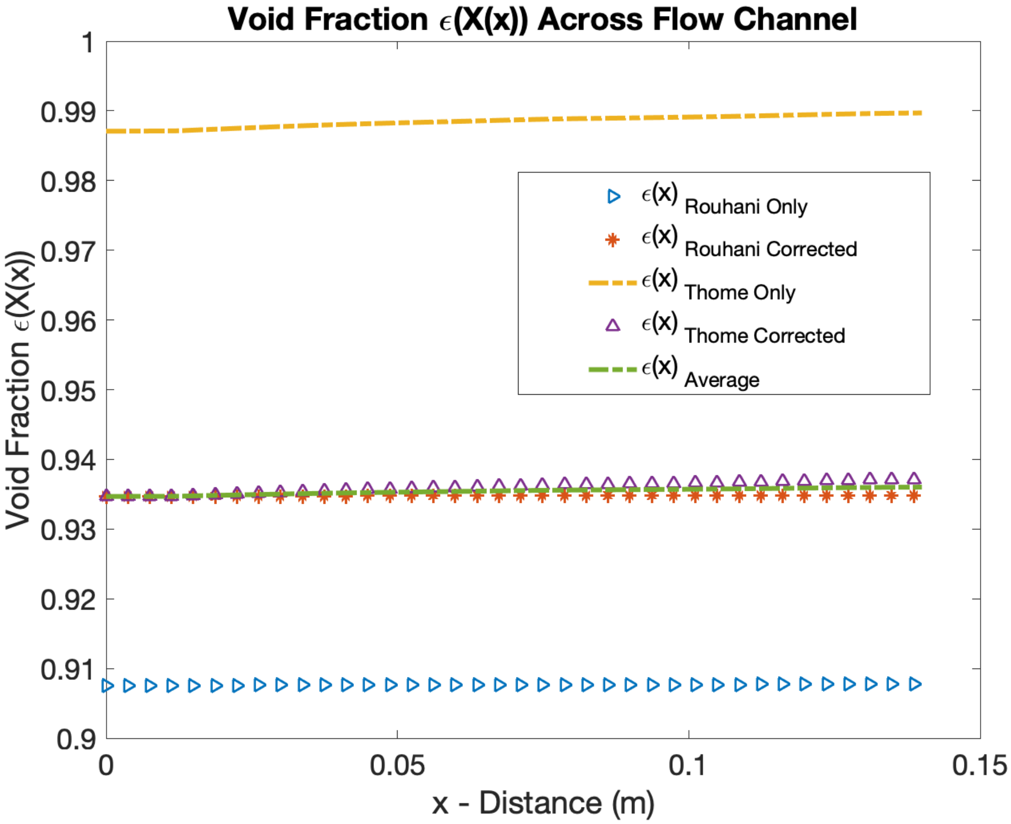

Figure 4-7: Two existing void-fraction models ϵ(X(x)) versus distance x (m) curves – with and without inlet condition adjustments - for a representative case 7 marked in Table-1. Quality X versus distance x (m) calculations is used to replace quality X with distance x. The mean "----" curve for the adjusted inlet condition is the proposed representative void-fraction model.

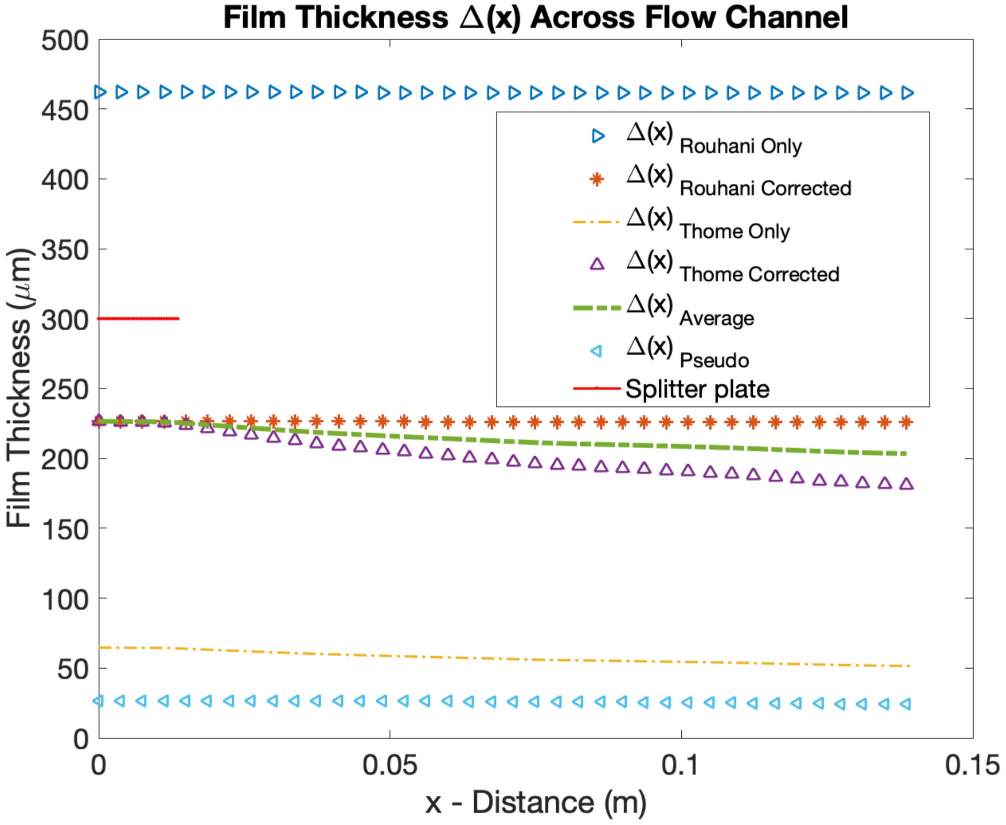

Figure 4-8: Film thickness "Δ (x) (m) versus distance x (m)" curves obtained from two existing void-fraction models $\epsilon(X(x))$ – with and without inlet condition adjustments - for a representative case 7 marked in Table-1. The mean "----" curve for the adjusted inlet condition is the proposed representative model for film thickness Δ (x) (m). $\Delta(x)_{Pseudo} \approx$ 10-20 μm - film thickness required to have same order of magnitude Experimental h(x|cb)

4.5 Comparisons between Measured and Modeled Pressure Drops

Despite allowable neglect of entrainment rates leading to Equation (4.6), the measured pressure-difference Δp_L in Figure 2.4 is expected approximately agree with the modeled value of the total pressure difference (See section 2.2.3.3). This is because one dimensional momentum balance must approximately be satisfied. However only approximate agreement is expected because interfacial shear stress models are inadequate even for adiabatic two-phase flows – let alone modelling of interfacial shear stress in the presence of phase-change and microscale nucleation rates. As a result, available models for $\left(-\frac{\partial p}{\partial x}\right)_{fric}$ ins equations (2.20) – (2.23) are quite approximate. Though improved modeling of $\left(-\frac{\partial p}{\partial x}\right)_{fric}$, by combined consideration of data in this thesis and those in [5-7], can be attempted to ensure near equality of measured and modeled values of Δp_L in Figure 2.4 – such efforts are outside the scope of this thesis. Under reported conditions, therefore, only "order of magnitude" agreement is expected between measured and modeled values of Δp_L in Figure 2.4 . By modeling $\left(-\frac{\partial p}{\partial x}\right)_{fric}$ as the mean of two predictions – one employing Lockhardt – Matinelli correlations [13] and the other employing Friedel correlations [14] – and using the remaining modeling approaches described earlier in this thesis, Table 4.1 is obtained for data in Tables 2(A-B). It demonstrates order of magnitude satisfaction of momentum balance. Note that "order of magnitude" agreement between measured and modeled values of Δp_L (as defined in Figure 2.4) is the same as approximate satisfaction of momentum balance expressed as Equations (2.20) – (2.23).

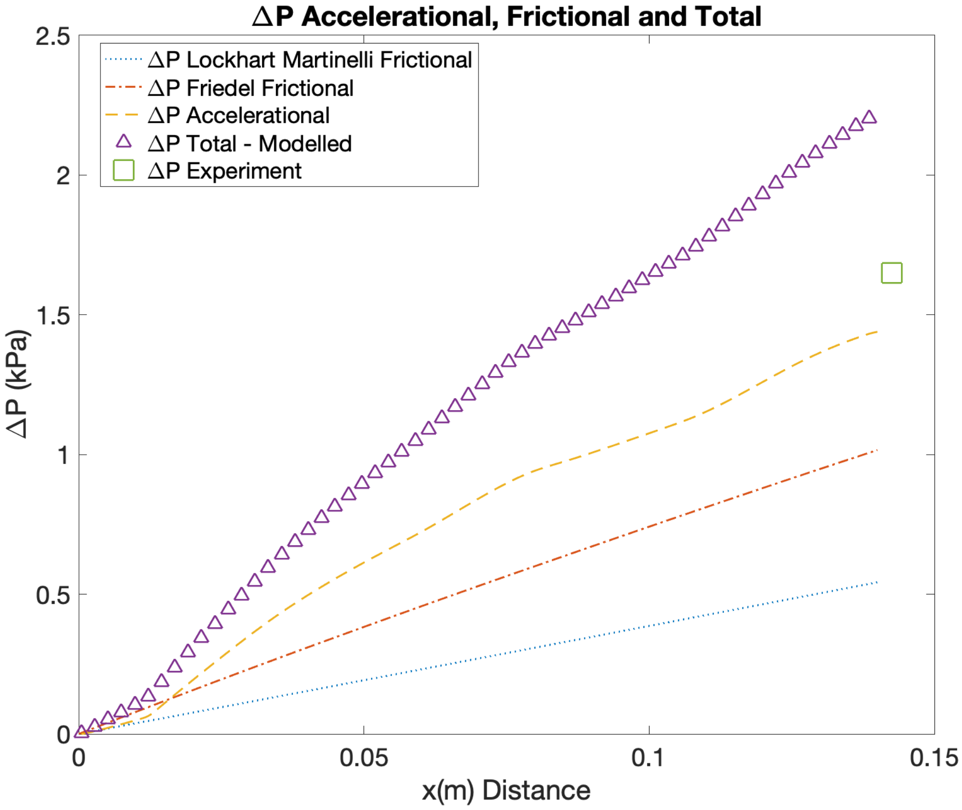

Figure 4-9: Pressure drop variation through the channel from the inlet to the outlet. Average of Lockhart Martinelli and Friedel model was used for calculation of total modelled pressure drop. The green square shows the experimental pressure drop through the flow channel.

Table 4.1: Pressure Drop comparisons for measured and modeled values of Δp_L in Figure 2.4

Case #	ΔP Experiment (kPa)	ΔP Friction (kPa)	ΔP Friction + ΔP Acceleration (kPa)	% Error
8	1.1	0.78	1.23	11.82
9	0.8	0.804	1.44	80.00
10	0.8	0.808	1.53	91.25
11	0.53	0.855	1.24	133.96
12	1.51	0.918	1.55	2.65
13	1.51	0.95	1.63	7.95
14	1.65	0.97	1.72	4.24

4.6 Estimation of $h_{x|cb}$ (i.e. HTC in the absence of nucleation) and its comparisons with experimentally measured $h_{x|Total}$ (total HTC)

As discussed in chapter 2, the new definition of $h_{x}|_{cb}$ in Equation (2.3) implies that its computations for annular flows are associated with the hypothetical absence of heat carrying nucleate boiling – resulting in a hypothetical heat-flux $q''_w|_{cb}$, all else remaining the same. Also, as discussed in Chapter 2, very good estimates of

$$q''_w|_{cb} \equiv h_x|_{cb} \cdot \Delta T(x) \cong \frac{k_L}{\Delta(x)} \tag{4.7}$$

are available through $\Delta(x)$ if it is estimated – using void fraction correlations – as in Figure 4.8. The resulting estimate of $h_x|_{cb}$ for a representative case 7 marked in Table-1 is shown in Figure 4.9 below.

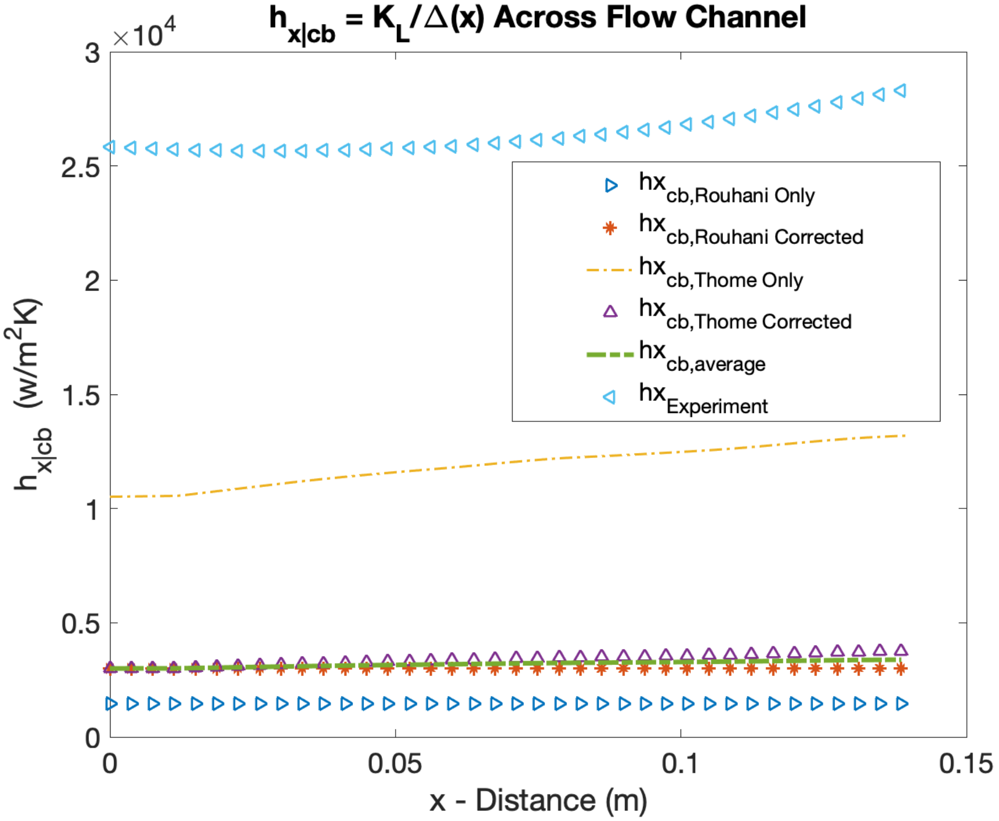

Figure 4-10: Proposed estimates for convective part of local HTC, $h_x|_{cb}$ (W/m^2-ºC), versus distance x (m)" curves obtained from two existing void-fraction models $\epsilon(X(x))$ – with and without inlet condition adjustments - for a representative case 7 marked in Table-1. The mean "----" curve for the adjusted inlet condition is the proposed representative model for local HTC, hx|cb (W/m^2-ºC). h(x|cb) are obtained assuming as if no nucleation. Let: $h_{(x|Total)} = k_L/\Delta(x)_{Pseudo}$

The same estimate of $h_x|_{cb}$ in Figure 4-9, for which $h_x = h_x|_{Total}$ has been obtained in Figure 4-1, is shown again – along with $h_x|_{Total}$ – in Figure 4-10 below. Figure 4.10 exemplifies the remarkable dominance of $h_x|_{nb}$ in Equation (2.3). This dominance is largely arising from "micron and sub-micron" scale nucleate boiling contributions for the thin film (Figure 4.8) annular flow-boiling situation. This result supports numerous similar results obtained for low heat-flux annular boiling experiments [5-7] as well as in [8] where void-fraction correlations were adjusted as per the approach described here (which uses Equation (4.1)) and, instead of experimental results for $h_x|_{Total}$, an order of magnitude correlations based estimate (using [1], [2] & [4]) was used. This is an important result which emphasizes the importance of nucleation rate mechanisms – as denoted by $\{S^*\}$ in Equation (2.14) – that need to be harnessed for developing technological solutions addressing high heat-flux electronic cooling (see [11], chapter 1) needs.

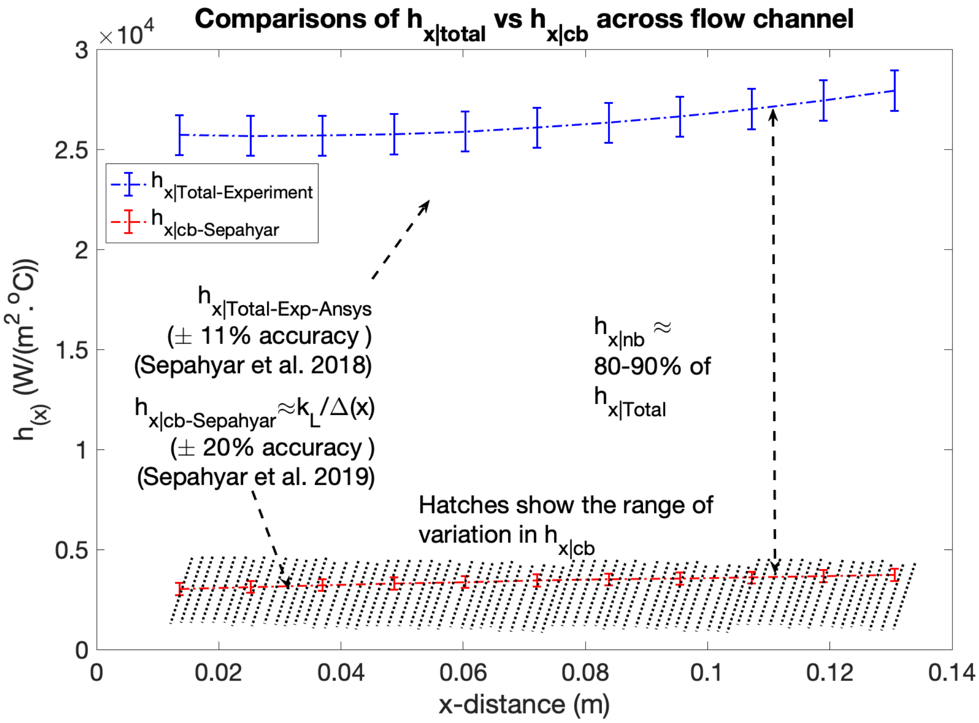

Figure 4-11: Comparison of experiments-simulations synthesis based local HTC h_x (W/(cm^2-°C) versus distance x (in m) curves for case#x marked in Table-1 with convective part of local HTC, $h_x|_{cb}$ (W/m^2-°C), versus distance x (m) curve as obtained in Figure 4.9.

The significant distance between the two in the proposed Equation (2.3) decomposition $h_x|_{Expt} \equiv h_x|_{cb} + h_x|_{nb}$ establishes the dominance of micro-scale nucleation ($h_x|_{nb}$is about 80 – 90 % of the total h_x) for this thin liquid film (see Figure 4-8 for film thickness in the range of 200 – 230 μm) annular flow boiling regime.

4.7 Comparisons of Proposed and Conventional Decomposition of HTC into Nucleate and Convective Parts

Also, if one were to replace $h_x|_{Total}$ in Figure 4-11 by an order of magnitude correlations based estimate (using [1]) and denote it as $h_x|_{Total\text{-}KM}$, we can obtain its variations with distance x , as shown in Figure 4-12 below. Further, one can use the conventional/traditional decompositions (as in [1]) of $h_x|_{Total\text{-}KM}$ into nucleate (denoting it as $h_x|_{nb\text{-}C/T}$) and convective (denoting it as $h_x|_{cb\text{-}C/T}$) parts and plot them as well. This is also done in Figure 4-11, where one clearly obtains a diametrically opposite and minimal role of nucleate boiling for the "so called" convective annular regime.

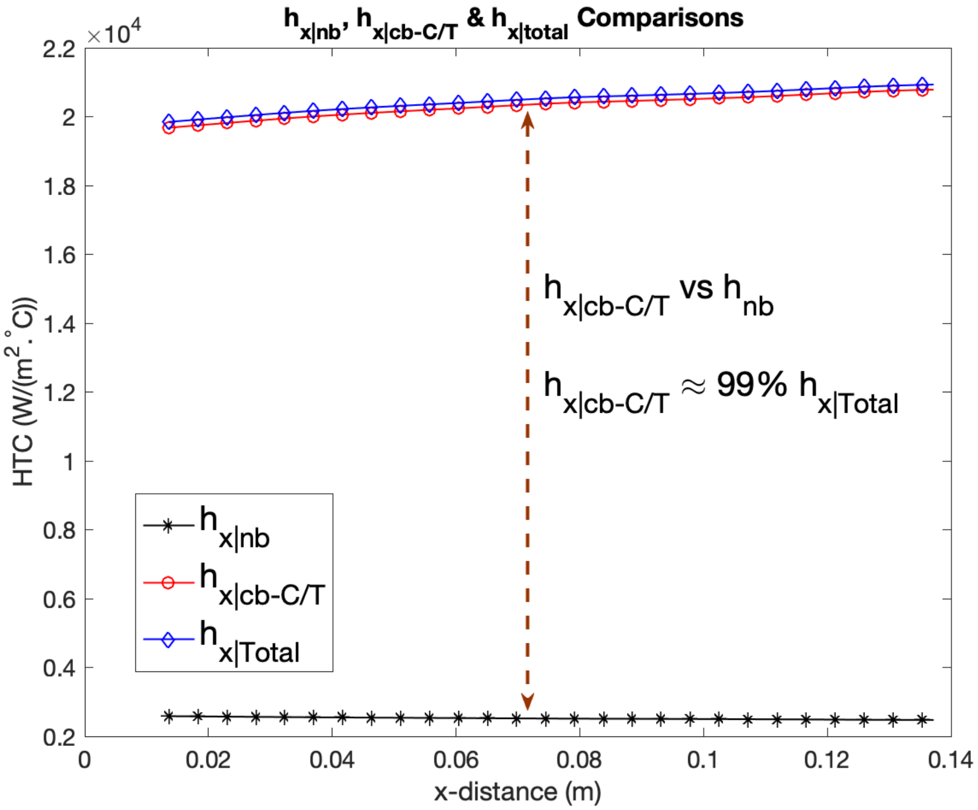

Figure 4-12: For the same case as in Figure 4-11, if the corresponding Kim and Mudawar correlation's [1] h_x values from Figure 4.4 is used and is decomposed in conventional/traditional ways (note that in this Figure $h_x|_{total} = h_x|_{total\text{-}KM}$). As in [1], the decomposition is into convective ($h_x|_{cb\text{ - }C/T}$) and nucleate boiling ($h_x|_{nb\text{ - }C/T}$) parts. The

dramatically different than Figure 10 variations - with respect to distance “x” -are obtained above. Here $h_x|_{cb\text{ - }C/T}$ component dominates.

Therefore, the new definition of decomposition of $h_x = h_x|_{Total}$, as in Equation (2.3), is important. Yet there are no problems with classical/traditional decompositions if: (i) its misleading names are changed, and (ii) it is recognized that these classifications are based solely on strong and weak dependences on $\bar{q}''_w$ in Figure 2.3. A sample set of representative calculations shown in Figure 4-13 below – where Klimenko [2] correlation has been decomposed into its constituent $h_x|_{cb\text{ - }C/T}$ and $h_x|_{nb\text{ - }C/T}$ parts – shows that the new results do not question the strong and weak dependences on $\bar{q}''_w$ criteria employed in conventional/traditional decompositions. This thesis’s data, being restricted to annular regime, does not cover the stronger $\bar{q}''_w$ dependences observed for the lower qualities range shown in Figure 4-13 – or similar data elsewhere ([1], [3], etc.) in numerous other experiments/correlations. Therefore this thesis does not question the conclusion that there is a much higher sensitivity (to mean heat-flux $\bar{q}''_w$ values) of local HTC h_x values associated with larger sized bubbles encountered for low quality X values that correspond to what are typically termed nucleate/bubbly regimes of flow-boiling.

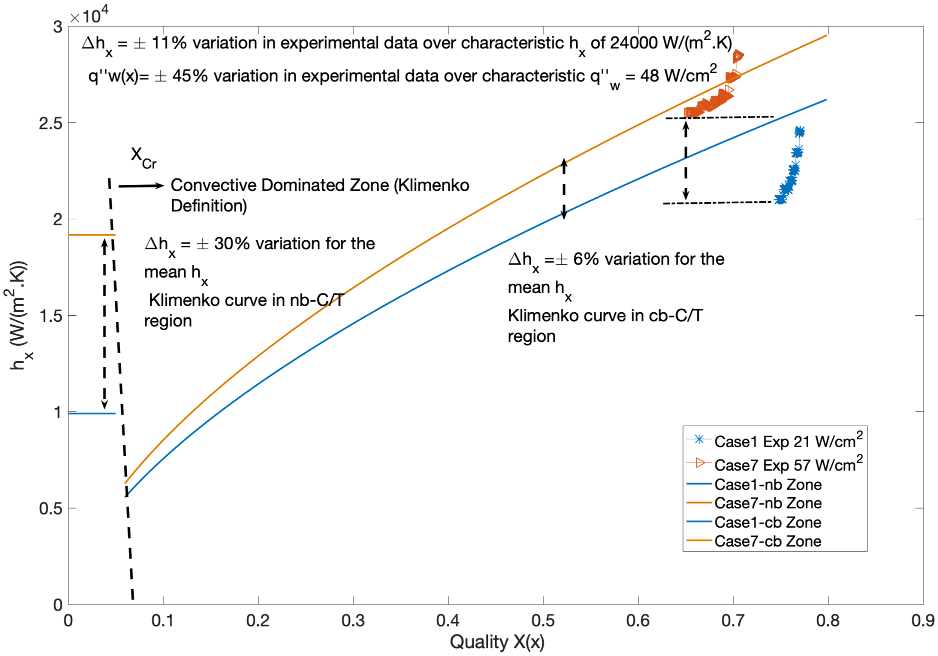

Figure 4-13: The h_x data obtained here all fall - in the conventional/traditional sense – in the convective regime. The experimental values and the regimes are limited – but in agreement with typical heat-flux dependencies associated with such classifications (here Klimenko [2] is used to cover a larger range of qualities).

It should be re-emphasized here that in [5-7], where a rigorous laminar/laminar direct numerical solutions (DNS) is used to obtain $\bar{q}''_w$ values for low heat-flux cases – and results are compared with low heat-flux experimental data – the remarkable dominance of nucleate boiling (as observed in Figure 4-11) continue to hold. Only regions of suppressed nucleation rates – that are widely acknowledged and are also observed and inferred (with modeling help) – that are known to us (see [15]) correspond to vary thin (1- 30 μm) films near stable dryout zone in Figure 2.3a.

4.8 General Compatibility of Results with Overall Energy Balance for Flow-boiling

Local energy balance is satisfied by experiment-modelling synthesis and it yields $h_{x|Total}$ values in Figure 3-9 over $0 \leq x \leq L$ (also see Figure 3.1). However, overall energy balance is only accurately satisfied over $x^* \leq x \leq L^*$ (as discussed in section 3.1).This is because the “elliptic” stagnant zone between x = L* and stagnation chamber in the test-section in Figure 3-1 is expected to have recirculative vapor flow and some liquid entrainment in the form of tiny drops (from the liquid at the bottom to the vapor). This causes vapor outlet flow to have small portion of tiny liquid drops. Even a small 0.5% of entrainment rate can cause – because of the large latent heat of water – a disagreement between heat inputted $\dot{Q}_{in|flow}$ to the channel (which partially boiled off liquid flow) and the one calculated for overall energy balance may arise. For 0.5% entrainments, an average error of 20-25% in $\dot{Q}_{in|flow}$ values as obtained from the equation below is possible. Flow-based energy equation is given as:

$$\dot{Q}_{in|flow} \cong \left(\dot{M}_{L_{in}} - \dot{M}_{L_{out}}\right) * h_{fg} \tag{4.1}$$

Last but not least, recall the associated uncertainties in the flow measurement and heat input to the heater-blocks are also considered. These values of uncertainties are given in Table 1 and Table 2. Therefore this average 20-25% discrepancy in $\dot{Q}_{in|flow}$ values is acceptable – as this does not affect the values reported over $x^* \leq x \leq L^*$. The average 20-25% discrepancy in $\dot{Q}_{in|flow}$ values are shown in associated tables given in Appendix C (see Tables C-1 and C-2).

5 Conclusions

The main conclusions are:

- Successfully designing, purchasing, manufacturing, assembling and testing a new experimental hardware and software which developed from ground zero.
- This thesis was able to implement a unique experiments-simulations synthesis yielding local HTC values for steady annular flow-boiling in horizontal rectangular cross-section ducts that involve water as working fluid and moderate-to-high heat-flux operations.
- The local HTC results are in order of magnitude agreement with existing HTC data and correlations.
- Building on earlier results and hypotheses for low heat-flux local HTC values for steady annular flow-boiling in horizontal rectangular cross-section ducts (involving FC-72 and modeling/simulation approaches), this thesis further establishes – for higher heat-flux cases – a new meaning and decomposition of local HTC values into its convective and nucleate parts. In this new meaning and decomposition, it is again established that most of the typically encountered annular regime flow-boiling locations are dominated by micron to sub-micron scale heat carrying nucleation rates (typically they carry over 80% of the heat).
- The conclusion above suggests and enables a new technological approach (patent pending) for achieving high heat-flux operations that restrict flow boiling to a specific regime (say low exit quality flows involving nucleate/bubbly regimes over the entire length of the duct) and then introduces new nucleation-rate altering mechanisms. The new mechanisms significantly add to the critical roles that micron to sub-micron scale heat carrying nucleation rates can play (as identified in this thesis).

REFERENCES

1. Kim S-M, Mudawar I (2013c) Universal approach to predicting saturated flow boiling heat transfer in mini/micro-channels – Part II. Two-phase heat transfer coefficient. International Journal of Heat and Mass Transfer, 64: 1239-1256.

2. Klimenko, V. V. "A generalized correlation for two-phase forced flow heat transfer." International Journal of heat and mass transfer 31, no. 3 (1988): 541-552.

3. Kandlikar, Satish G. "A general correlation for saturated two-phase flow boiling heat transfer inside horizontal and vertical tubes." Journal of heat transfer 112, no. 1 (1990): 219-228.

4. Dorao, Carlos A., Oscar Blanco Fernandez, and Maria Fernandino. "Experimental Study of Horizontal Flow Boiling Heat Transfer of R134a at a Saturation Temperature of 18.6 C." Journal of Heat Transfer 139, no. 11 (2017): 111510.

5. Patcharapol Gorgitrattanugul, Ph.D from MTU. “Experimental Investigation of temperature controlled innovative annular flow-boiling of FC-72 in millimeter scale ducts-steady and enhanced pulsatile realizations.” (2017).

6. Narain, A., H. Ranga Prasad, Gorgitrattanagul, P, S. Sepahyar and Mehendale, S, “Significant Role of Heat carrying Micro-scale Nucleation Rates for Steady Annular Flow boiling (Traditionally termed Convective Regime), Part I: Modeling/simulations support for assessments of experimental data.” To be submitted.

7. Gorgitrattanagul, P., A. Narain, R. Kumar*, A. Ghate, and D. Pandya, “Significant Role of Heat carrying Micro-scale Nucleation Rates for Steady Annular Flow boiling (Traditionally termed Convective Regime), Part II: Experiments for Low Heat-flux Operations with FC-72 as a Working Fluid.” To be submitted.

8. Narain, A., Ranga Prasad, H. and Koca, A., "Internal Annular Flow Condensation and Flow Boiling: Context, Results, and Recommendations." In: Kulacki FA (ed.) Handbook of Thermal Science and Engineering, 2018, vol. 3, pages 2075-2162. Springer, Cham. Invited Article.

9. Rouhani SZ, Axelsson E (1970) Calculation of void volume fraction in the subcooled and quality boiling regions. International Journal of Heat and Mass Transfer, 13(2):383–39.3

10. Cioncolini, A., Thome, J.R., 2012. Void fraction prediction in annular two-phase flow. Int. J. Multiphase Flow 43, 72e84.

11. Carey VP (1992) Liquid-vapor phase-change phenomena. Series in chemical and mechanical engineering. Hemisphere Publishing Corporation, New York.

12. Ghiaasiaan SM (2007) Two-phase flow, boiling, and condensation: in conventional and miniature systems. Cambridge University Press, Cambridge.

13. Lockhart R, Martinelli R (1949) Proposed correlation of data for isothermal two-phase, two-component flow in pipes. Chem. Eng. Prog, 45: 39-48.

14. Friedel L (1979) Published. Improved friction pressure drop correlations for horizontal and vertical two-phase pipe flow. European two-phase flow group meeting, Paper E.

15. Narain A, Kivisalu, M., Naik, R., Gorgitrattanagul, N., Mitra, S., Hasan, M. M. (2012) Published. Comparative Experimental and Computational Studies for Annular Condensing and Boiling Flows in Milli-meter Scale Horizontal Ducts. Proceedings of ASME 2012 Summer Heat Transfer Conference, Rio Grande, Puerto Rico, USA. ASME.

A Experimental Hardware

This section discusses and presents all the hardware components used in Two Phase Flow Loop and the associated Test-Section and components. The flow-loop here is the whole set up including all components which includes test-section as well as other components.

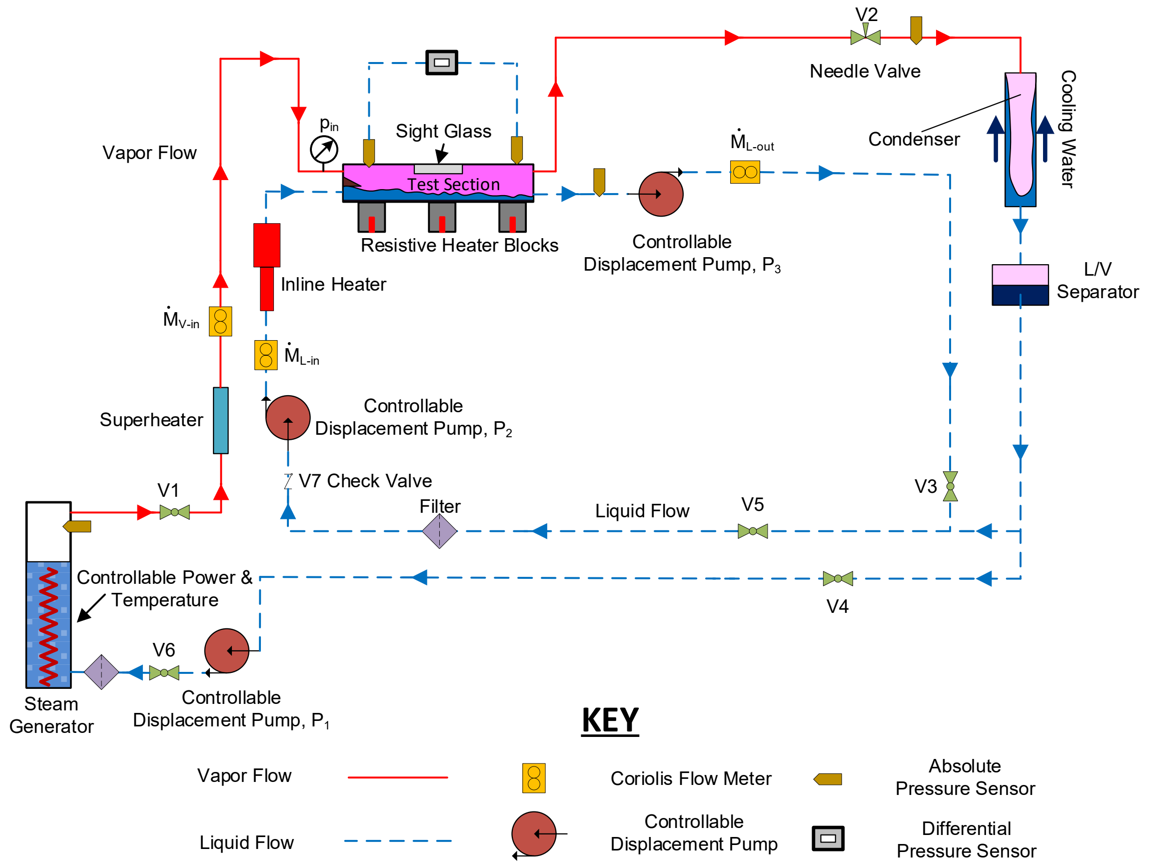

Figure A-1 High Heat Flux Water Flow Loop Schematic. This includes all the components that are going to be presented later in this section. The figure is self-explanatory with additional legends that show all components.

Figure A-2 The flow loop physical set-up during a test run on December 27th 2018. The high-speed camera is set up at the top of the tripod facing and adjusted in the flow channel during the run.

A.1 Test-Section

The purpose of the test-section is to provide a controlled environment for flow-boiling water safely at high (up to 500 W/cm^2) heat-flux values while supporting a sufficiently high through-flow of steam to stabilize the annular flow regime over the entire heated length of the flow channel by means of interfacial shear stress. Provision is made for up to 5 heaters underneath the test-section flow channel. Currently 3 heater blocks are implemented underneath the test-section. Heating is provided mainly from the bottom of the flow channel, with some heat entering through the sides as well. A window (sight glass) forms the top of the flow channel over a region of interest covering most of the heated length.

The main features of the test-section are illustrated in the schematic of Figure A-3 simplified geometry of the test-section and location of the heaters and transducers is shown in Figure A-4. Both figures show the details of liquid and vapor inlet and outlets. An exploded 3D-CAD view of the test-section components is shown in Figure A-5 and Figure A-6 indicates a cut through of flow-channel and associated housing. Pictures of the physical components of the test-section and its configuration currently being used are shown in Figure A-7 in an exploded view.

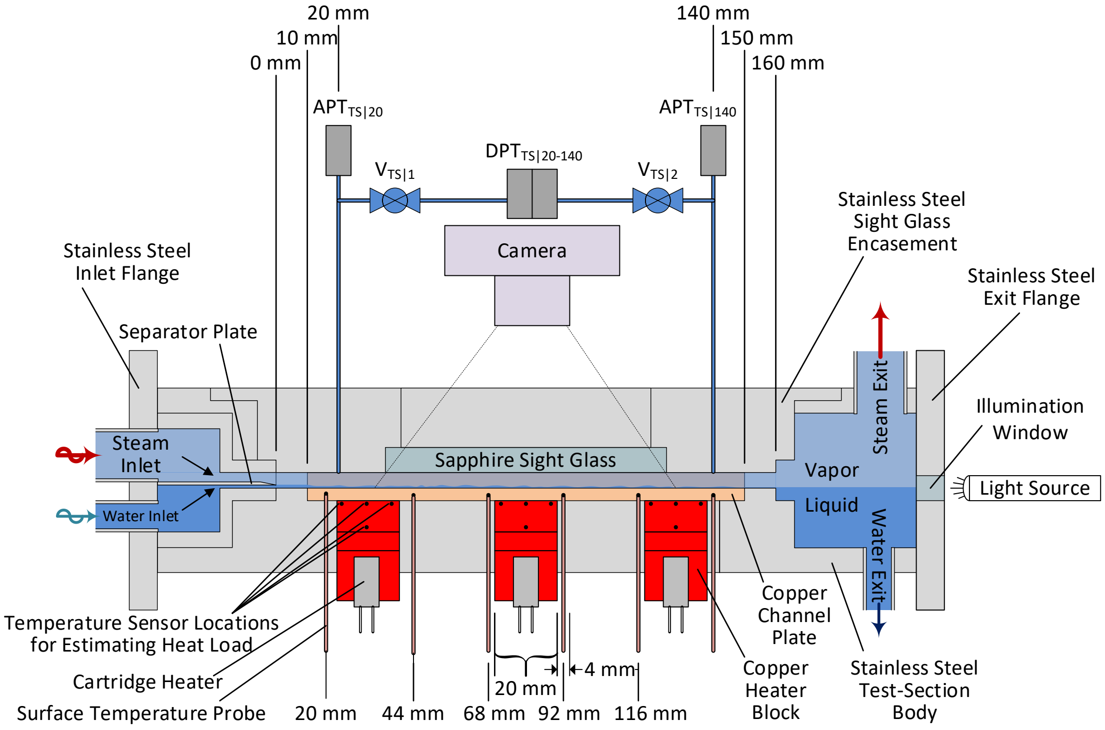

Figure A-3 Test-Section Detailed Schematic. This represents the physical configuration of the test-section as it currently exists. Here the reference point for distance along the flow channel is the end of the separator plate, and relevant downstream distances are labeled above and below the channel with vertical leaders. The width of the flow channel is 10 mm and its height 5 mm.

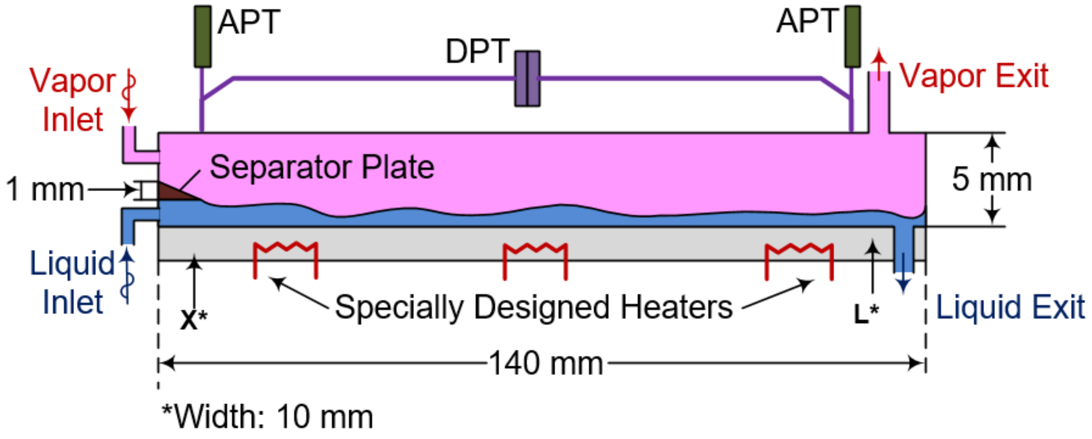

Figure A-4 This is a simplified schematic of Figure A-3 The channel length is not representative of the physical configuration.

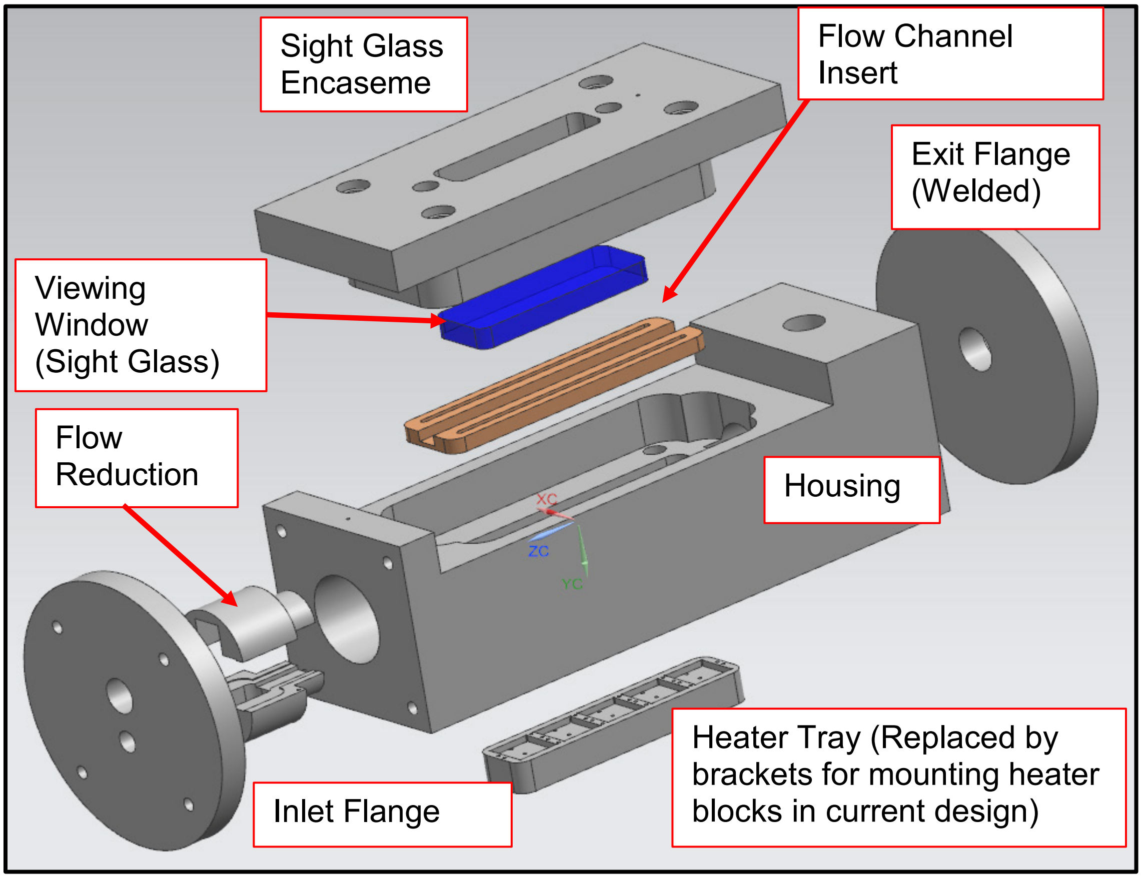

Figure A-5 Test-Section Exploded View. This represents the main components of the test-section as they currently exist, with the exception of the heater tray, which is replaced by brackets for holding the new copper heater blocks and the flow channel temperature sensors.

The test-section assembly consists of a flow channel insert which is clamped within the housing by an encasement which contains a window to allow for flow visualization. Two pipe ports in the encasement, immediately adjacent to the window hole, support pressure measurements. Four bolts (bolts locations are shown in Figure A-5) hold the sight glass encasement on to the housing. These bolts are integral flange type stainless steel bolts. Teflon O-rings (not shown in Figures) underneath the heads of these bolts are retained by counter-bores and seal against leaks. These four bolts thread into blind holes in the housing, of which one is visible in Figure A-5. The use of blind holes eliminates any potential sources of leakage in the housing.

The inlet flange retains the two flow reduction halves and the separator plate (not shown in both Figure A-3 and Figure A-4) within the housing. It is held on by 4 screws (shown in Figure A-5). An o-ring groove within the bolt circle (not visible in figures), provides sealing with a high temperature silicone or Teflon o-ring. The exit flange is permanently welded to the test-section housing and is fitted with a single pipe fitting port for illumination and level-checking purposes. A circular sight-glass is inserted over there for illumination and verification of flow level in the stagnation chamber.

A gasket (not shown in Figure A-5) underneath the flow channel insert seals between its bottom surface and a ledge within the housing (see Figure A-6). The gasket has an opening to accommodate the heaters and thermocouples which interface with the channel insert from the bottom.

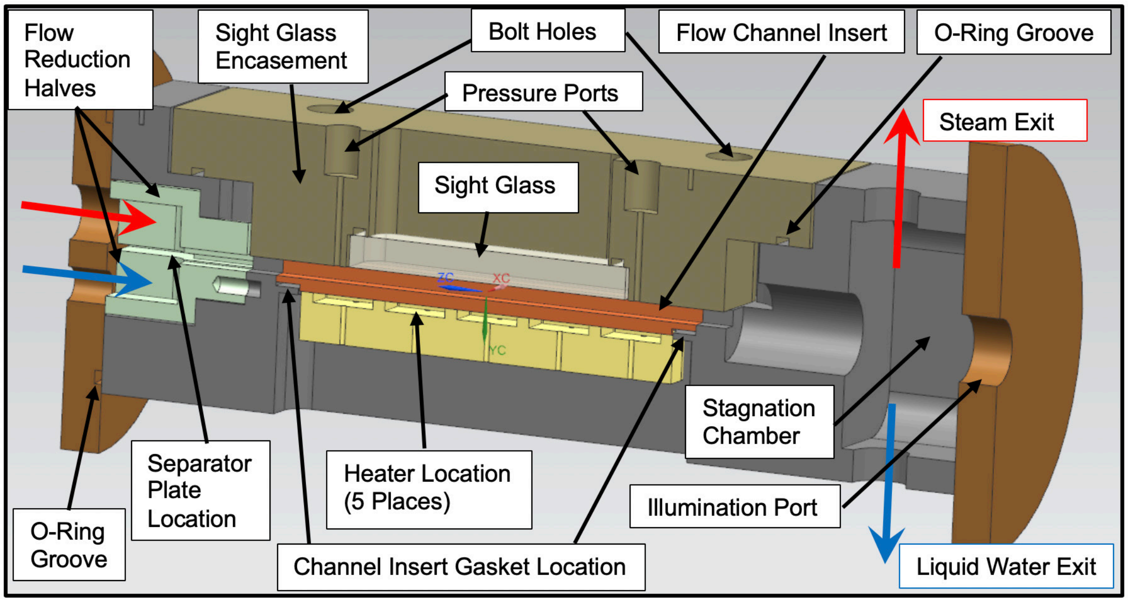

Figure A-6 Test-Section Cross-Section. Steam and liquid water enter from the left on opposite sides of a separator plate. After combining and passing through the flow channel insert, they are separated again in the stagnation chamber, where the steam exits upward, and the liquid water exits downward through pipe ports machined in the test-section housing.

Figure A-6 shows a cut-away view of the test-section, with the cut surface passing through the center of the flow channel with respect to its width. Steam (red horizontal arrow in Figure A-6) enters through a $^3/_8$ inch NPT threaded pipe port. Liquid water (blue horizontal arrow in Figure A-6) enters through a $^1/_8$ inch NPT threaded pipe port. Each of the two pressure ports consist of a $^1/_{16}$ inch diameter hole with a counter-bore in which is machined a ¼ inch NPT threaded pipe port. The steam exits upward (red vertical arrow in Figure A-6) through a ½ inch NPT threaded pipe port machined in the test-section housing, while the liquid exits downward through another ½ inch NPT threaded pipe port machined in the test-section housing. Liquid/vapor phase separation is accomplished by means of gravity acting within a stagnation chamber of significantly larger cross-sectional area than the flow channel. The yellow heater tray in Figure A-6 was originally designed to accommodate our specialized compact heaters which was manufactured inhouse. When those heaters became impractical within the scope of this grant, this part was exchanged for mounting hardware more practical to the new copper heater blocks that have been machined inhouse.

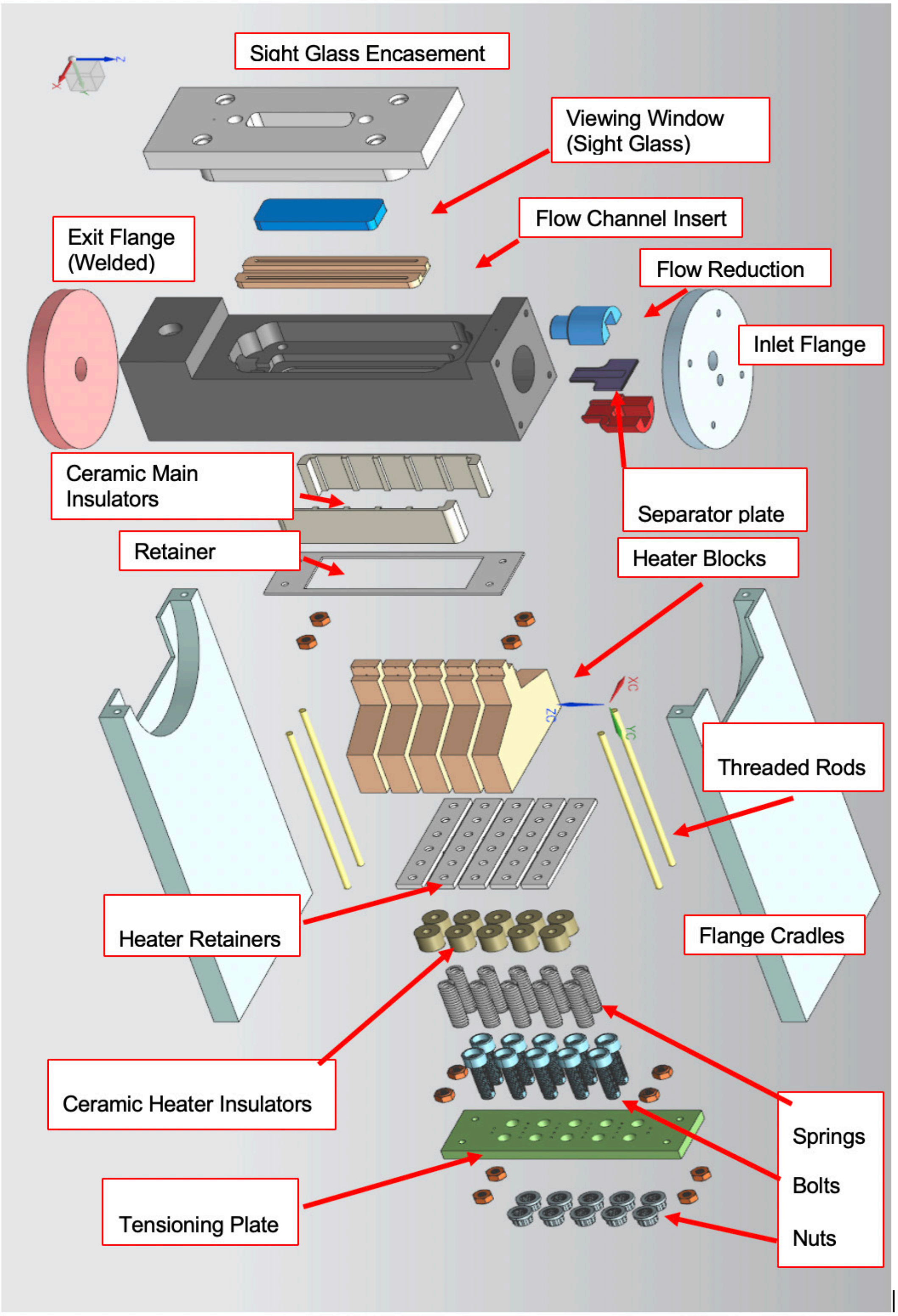
Sight Glass Encasement
Viewing Window
(Sight Glass)
Flow Channel Insert
Exit Flange
(Welded)
Flow Reduction
Inlet Flange
Ceramic Main
Insulators
Separator plate
Retainer
Heater Blocks
XC
ZC
YC
Threaded Rods
Heater Retainers
Flange Cradles
Ceramic Heater Insulators
Springs
Bolts
Tensioning Plate
Nuts

Figure A-7 Test-Section and Heater Mounting Block exploded view. This figure indicates final main parts of test-section, copper heaters along with the cradles and rest of components.

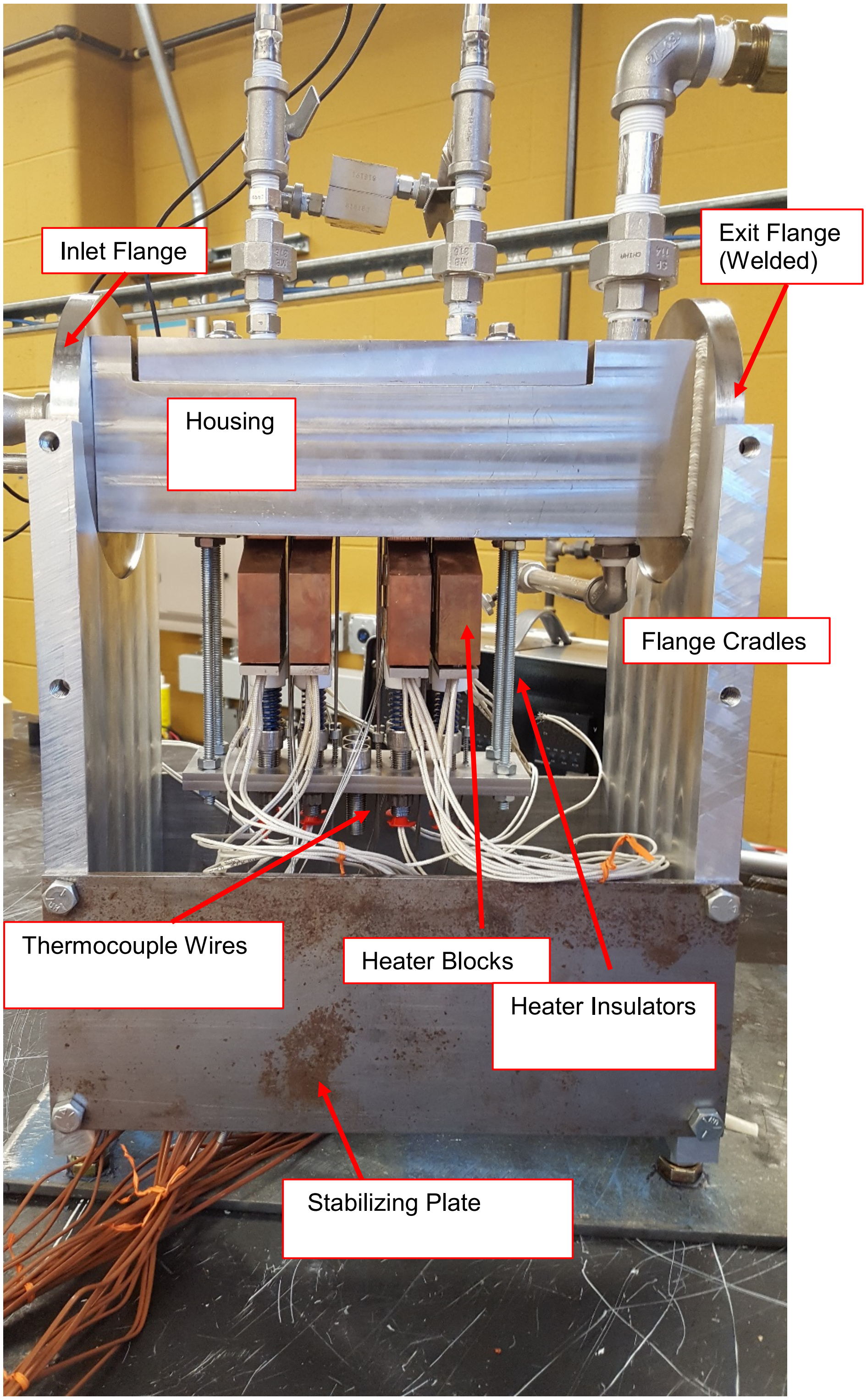

Figure A-8 Front view Test-Section final assembly.

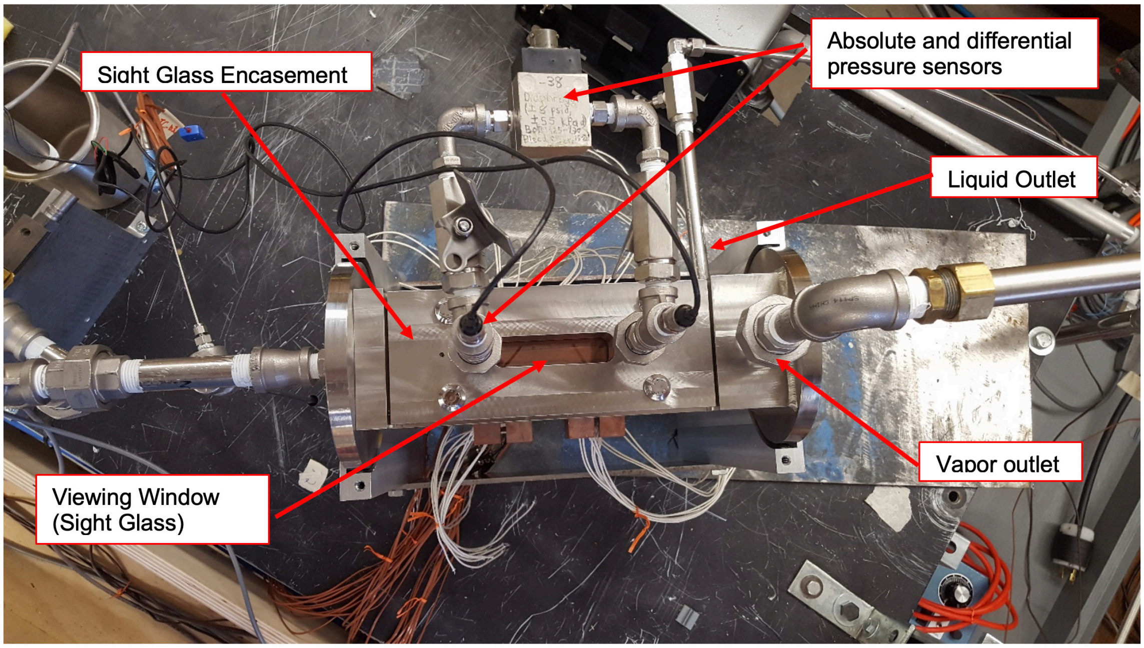

Figure A-9 Top view of the test-section assembly. The sight glass encasement which surrounds the sapphire glass viewing window is visible here.

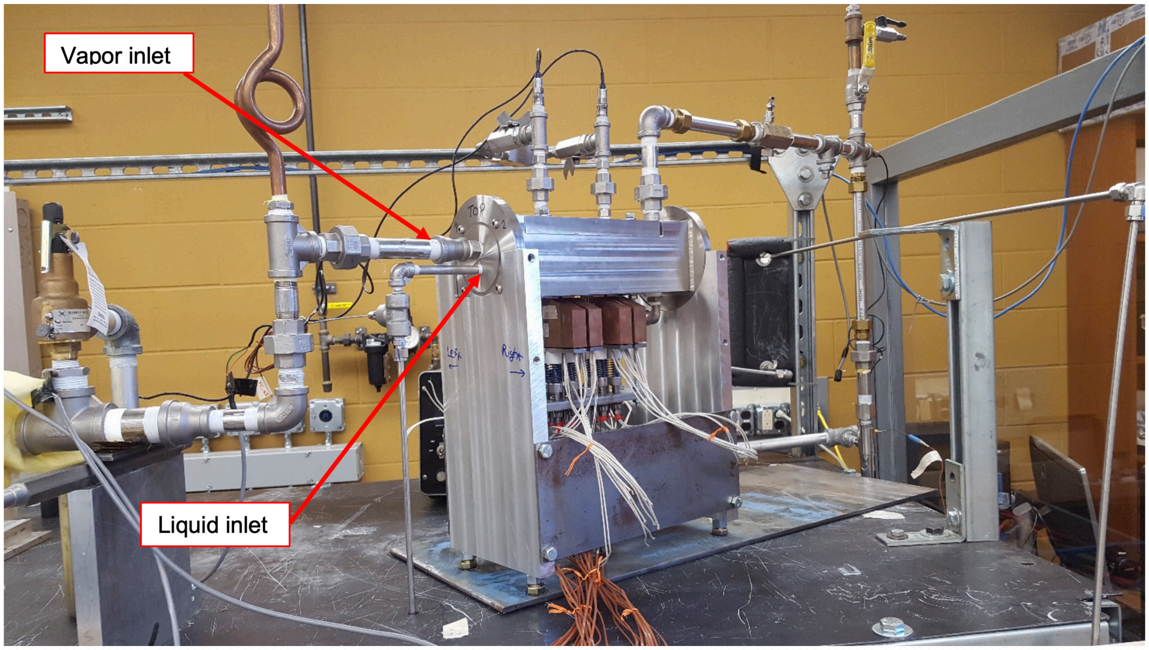

Figure A-10 Side view of the test-section physical assembly and mounting hardware with the vapor and liquid inlets indicated.

Figure A-7 shows the entire exploded view test-section assembly and mounting hardware. The sensors such as pressure transducers and thermocouples are not indicated in this figure but everything else in detail is visible in this figure. Currently instead of 5 heater blocks, only 3 heaters are being used for testing the system. Figure A-9 above is the top view of the physical implementation of the test-section. The flow channel is visible through the sight glass at the center of the picture. The differential pressure transducer (DPT) is offset from the center of the test-section to allow for flow visualization. The pipe branches to the right and left of the DPT contain low profile ball valves used for isolation. Figure A-10 is the side view of the assembly and mounting structure of test-section. With the liquid and vapor inlet clearly visible over here.

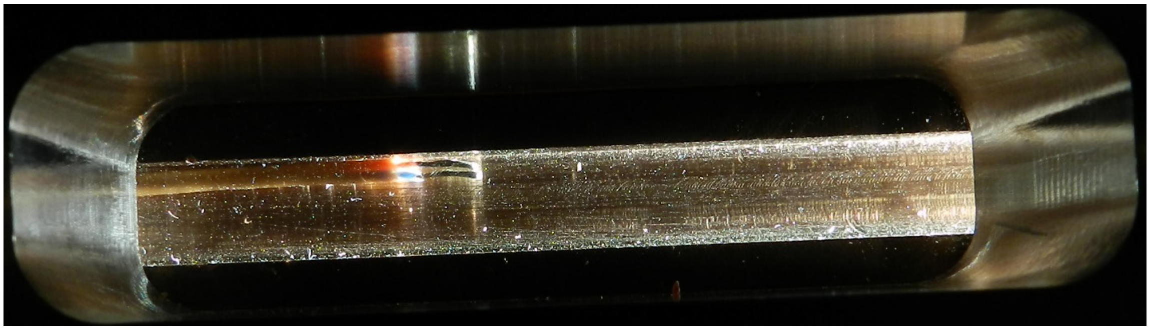

Figure A-11 Top View of Flow Channel. A pair of thermocouple wires has been placed in the flow channel for reference. The picture was taken in a dark environment using manual focus settings.

Figure A-11 shows an example of the type of flow visualization pictures that we expect to report. There is not flow in the channel, so a pair of thermocouple wires was inserted into the flow channel from the inlet end to provide a frame of reference. The illuminating light is coming from a light source through a bulls-eye sight installed in the illumination pipe port shown in Figure A-3.

A.1.1 Flow Channel

Flow Channel is 14 cm long, 1 cm wide and 5 mm high. This channel is made of Copper-C110 (390 $\frac{W}{m.°K}$, electrolytic tough pitch) to be highly thermal conductive. It is being heated from the bottom by the heater block and there are 10 thermocouple placed width wise and length wise across the channel from the inlet to the outlet to capture the bottom surface of the channel. Figure A-3 and Figure A-4 schematically show the location of the heaters and thermocouples on the bottom surface. There are two inlet ports and two outlet ports located in the test-section housing as stated above.

This choice of material minimizes thermal resistance at the cost of decreased corrosion resistance compared with the originally selected Nickel 201 alloy. The Nickel 201 alloy was not available in the dimensions required. Because of its lower corrosion resistance, this copper insert may need to be replaced as needed. If corrosion of this flow channel insert causes contamination of the water in the flow-loop, a corrosion resistant coating may be applied to surfaces exposed to the flow (such as nickel plating or high temperature paints). Figure A-12 below shows top and bottom views of the copper flow channel insert.

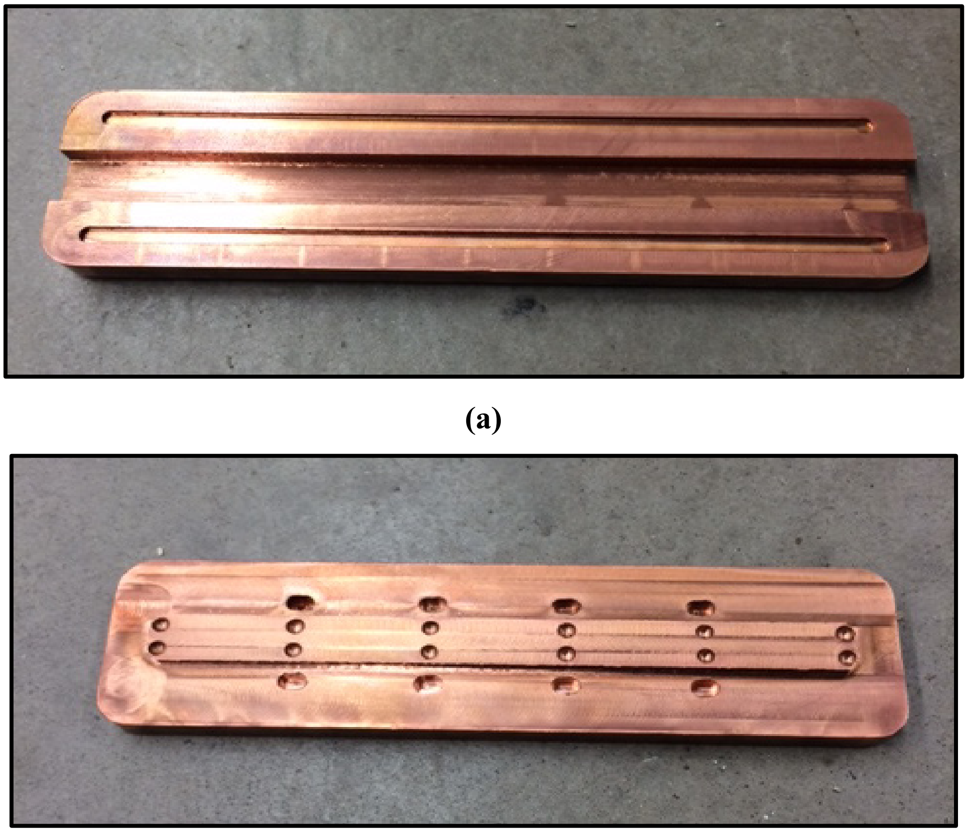

(a)

(b)

Figure A-12 (a) Top View Photograph of Flow Channel Insert. **(b)** Bottom View Photograph of Flow Channel Insert.

The top of the flow channel insert (see Figure A-12(a)) contains a central groove of 10 mm width and 5 mm depth through which liquid water and steam flow. The liquid water forms a thin film on the bottom of this groove. It is partly or completely boiled within this 140 mm long region as a result of heating in up to 5 distinct locations, each 20 mm long and separated by 4 mm gaps. Two smaller grooves, on either side of this central channel, accommodate high temperature silicone O-ring cord stock to cushion the sapphire glass against scratches.

Boiling surface temperature is measured from the bottom of this channel insert in six pairs of thermo-wells (round pockets on the raised portion of the insert in Figure A-12(b)) which approach the flow channel to within 2 mm but do not pierce into it. This design both provides a smooth surface for the boiling flow and prevents potential sources of leaks. Eight additional thermo-wells come from the bottom between the heated regions (4 on each side of the flow channel, see elongated pockets in Figure A-12(b)). They extend approximately 1 – 3 mm up each side of the channel and are positioned 7.5 mm on each side of its central axis. They also do not pierce into the flow channel. These 20 temperatures are used in conjunction with transient or steady conduction modeling, as appropriate, to obtain temperatures of the boiling surface.

A gasket underneath the flow channel seals between its bottom surface and the stainless steel housing. This gasket is made out of vermiculite and has a stainless steel insert for structural strength. Because of the small cross-sectional area available for sealing, it was necessary to use stove gasket cement in combination with the gasket to prevent leaks.

Five contact areas underneath the test-section flow channel – each of 10 mm width transverse to the flow channel and 20 mm length in the direction of the flow channel – are provided to support physical contact with heaters. Of these, 4 will typically be used in the immediately upcoming experiments at up to 0.5 kW/cm^2 heat-flux into the water. For future experiments (not part of our supplement request) a similar heating method may be used with 2 non-adjacent heated sections to achieve > 1 kW/cm^2 into the water at the flow channel bottom surface. These surfaces designated for heating are separated by 4 mm in the lengthwise direction to accommodate temperature sensors.

A.1.2 Sight Glass

Sight glass is located inside the test-section on top of the flow channel. It is made of high temperature sapphire glass and specifically designed, manufactured and purchased to be inserted in this location. It covers a significant portion of the channel as it is visible in the test section pictures.

A.1.3 Heaters

Heater Blocks are visible in previous pictures presented earlier. They are custom designed and machined copper heater blocks. They are used to concentrate heat from six cartridge heaters (not visible in the pictures but the heater wires can be seen in **Error! Reference source not found.** where the white wires coming out of the bottom of heater blocks) into a 10 mm by 20 mm cross-sectional area. Embedded thermocouple probes (Thermocouple wires are visible in different picture including Figure A-8) are horizontally embedded in the heat transfer path. Using a computational steady or transient conduction/convection analysis, thermal boundary conditions (surface temperature profile and heat load) from each heater block into the flow channel insert at their contact area may be estimated using these temperatures. For validation, the measured power (from the product of voltage and current) of the cartridge heaters can be compared with the heat loads needed required in the model at the cartridge heater locations to match the measured temperatures in the heat transfer path.

Each of the 6 cartridge heaters is rated for 200 W at 120 VAC; thus the combined maximum power available at each heater block is 1.2 kW. If all of this heat is transferred into the channel insert, this yields a maximum heat-flux of 0.6 kW/cm^2. Due to heat losses from the surfaces of each copper block not exposed to the channel insert, along with heat spreading within the channel insert, we expect a maximum of 0.5 kW/cm^2 to be available at the center of each heated region to transfer into the water film.

For the first round of experiments after initial validation of the test-section, the cartridge heaters were powered by 0 – 120 volt AC and 0-15 amps power supplies controlled through the computer and DAQ system. All 6 cartridge heaters in each heater block is wired in parallel such that one supply powers each heater block.

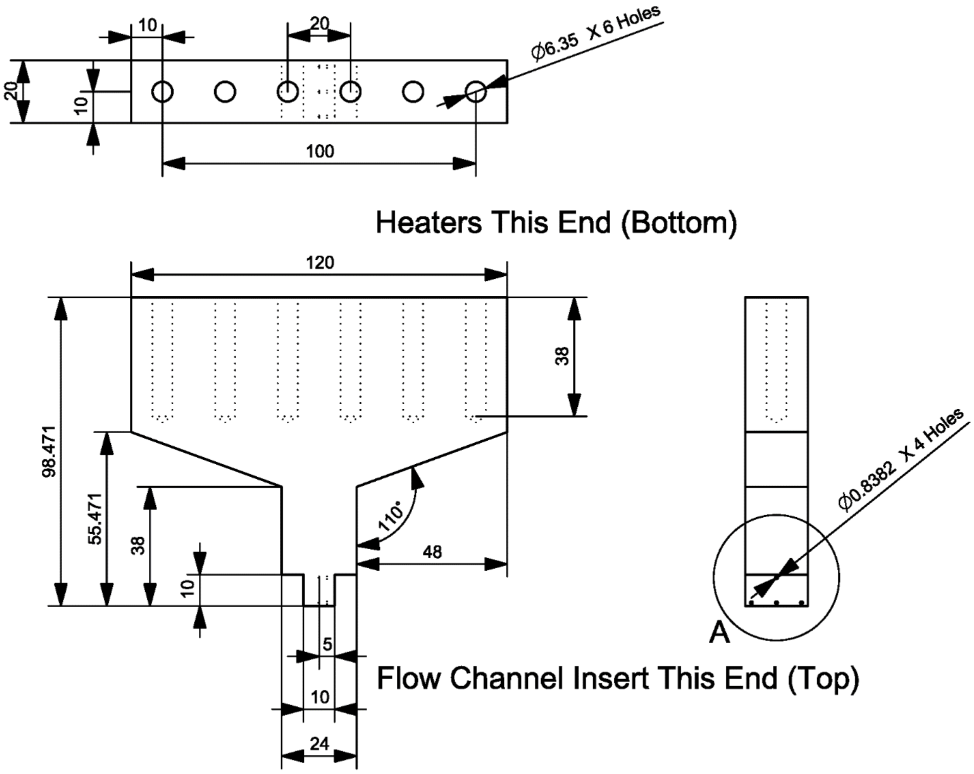

Figure A-13 Heater Block geometry and associated dimensions. Dimensions are in mm.

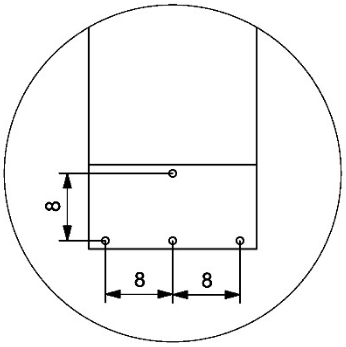

Figure A-14 Detailed view Heater Block geometry top part. Dimensions are in millimeters.

The heater block design of Figure A-13 was verified using steady conduction computational modeling to ensure that the selected heaters would not overheat while sourcing 0.6 kW/cm^2 to the channel insert through the tip of the heater block. This modeling defined the operating temperature range of the heater blocks to be 200 – 730 degrees C at maximum heat load.

A.1.4 Test-Section Housing

The test-section housing holds all of the components together. It is machined out of a single piece of 316/316L stainless steel. This material was chosen because of its superior corrosion resistance. Its low thermal conductivity compared to other metal alloys helps reduce heat leakage from the channel insert. However, its machinability was poor, and attempts from two different shops affiliated with Michigan Technological University were required to finish machining the housing. This added to the cost of the test-section and caused a delay of a few months. Pictures of the housing after it has been machined and the exit flange has been welded to it are shown in Figure A-15 below.

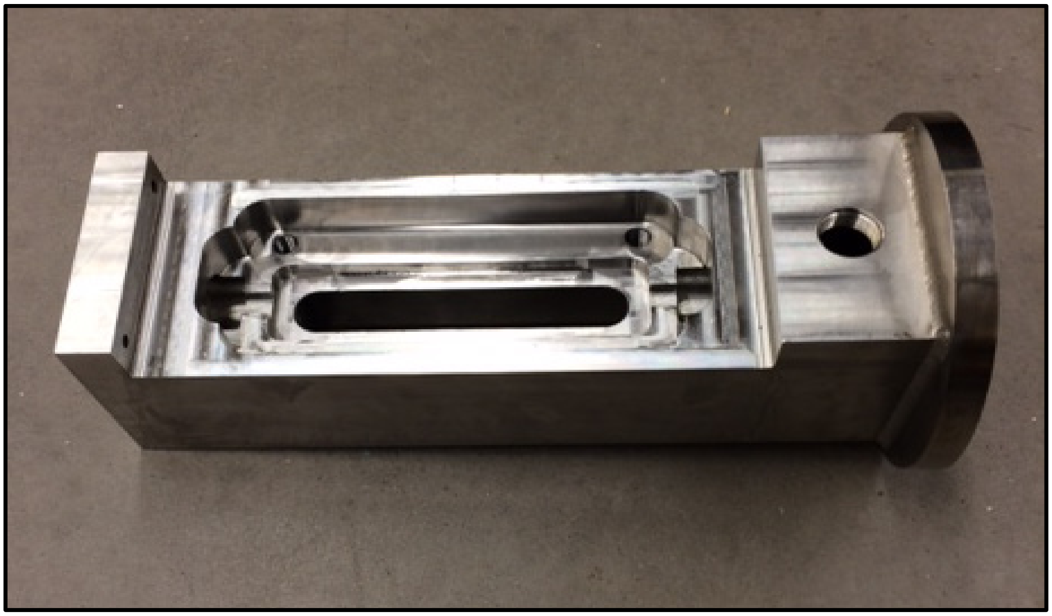

(a)

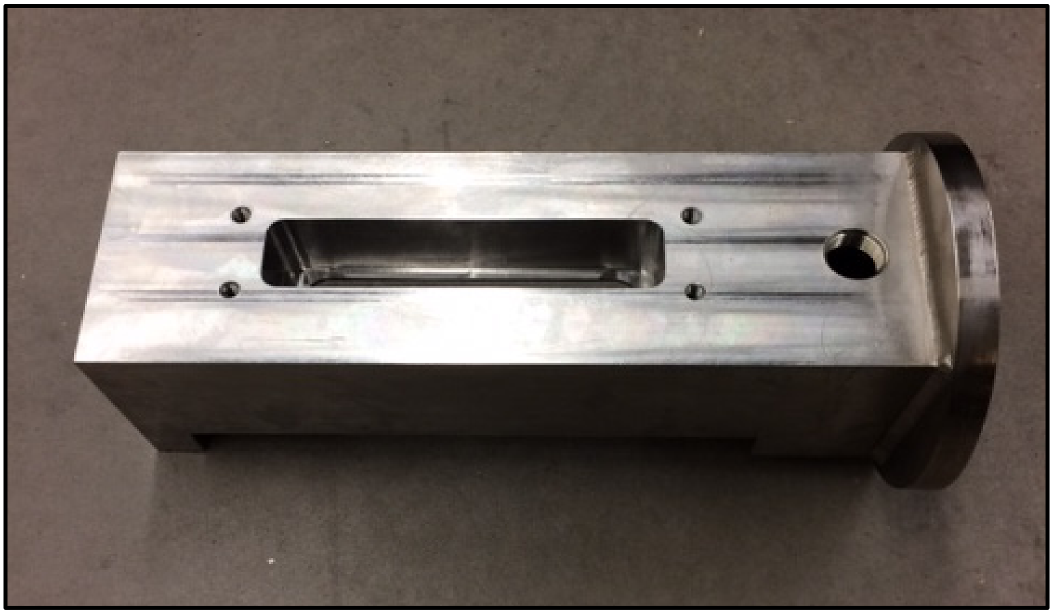

(b)

Figure A-15 (a) Top View and **(b)** Bottom View of the test-section housing with the exit flange welded to it.

The steam exit pipe port is visible to the right in Figure A-15(a), and the liquid water exit pipe port is visible to the right in Figure A-15(b). Two of the blind holes for the screws which hold the sight glass encasement are visible in Figure 14a. They are threaded $^3/_8$ - 16 UNC ($^3/_8$ inch, 16 threads per inch) to a depth of about 1 inch. The stainless-steel integral flange bolts which interface with them are shown in Figure A-16 below.

The four threaded holes around the pocket near the middle of the bottom of the test-section housing visible in Figure A-15(b) are for the threaded rods that will hold the mounting brackets for the heater blocks and thermocouple probes. These mounting brackets are currently being designed. There are also four threaded holes (not shown in Figure A-15) in the inlet end of the test-section housing for the screws that hold the inlet flange on to the test-section housing. The heads of these screws are visible in Figure A-16 below. These eight mounting holes are all threaded ¼ - 20 UNC ($^1/_4$ inch, 20 threads per inch) to a depth between ½ and 1 inch.

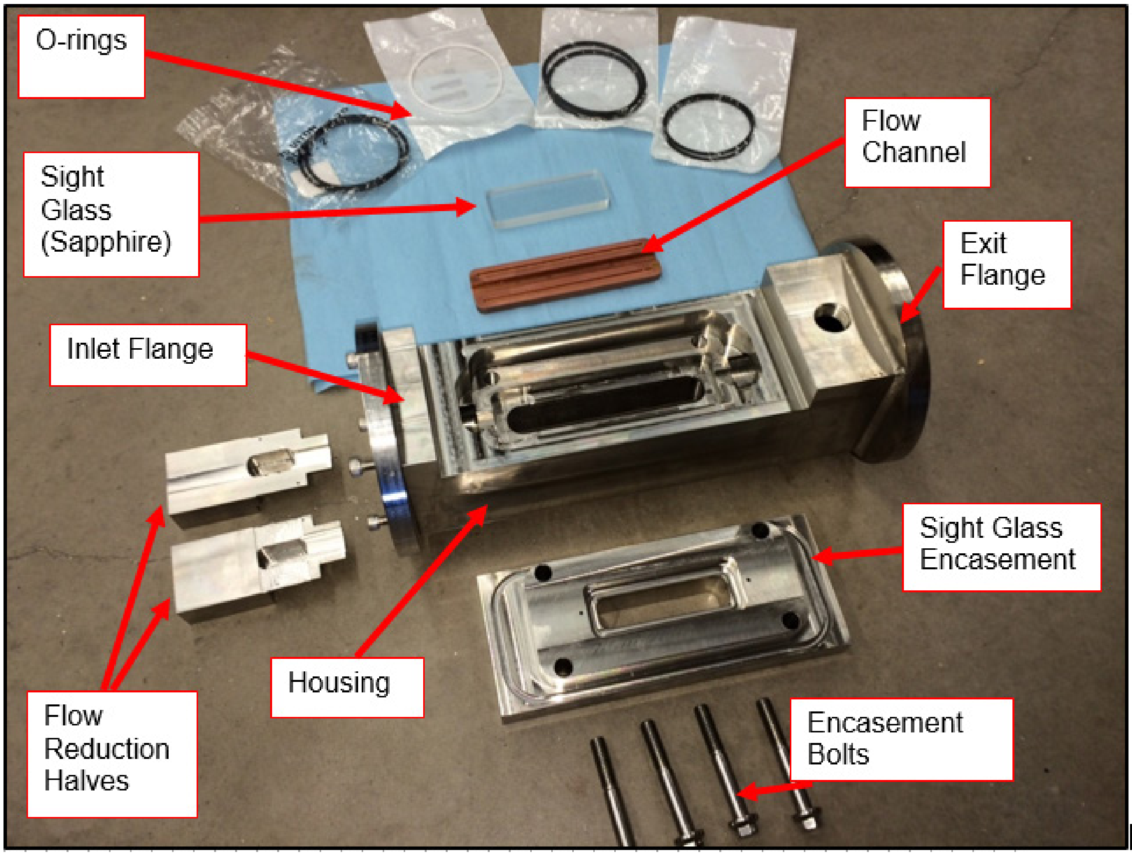

Figure A-16 Test-Section Main Components before Assembly.

Note that in the picture used for Figure A-16, the flow reduction halves are only partially machined. They have since been completed, along with the separator plate. Screw torque specifications for the fasteners interfacing with the test-section housing are shown in Table A- 1: Test-section Housing Screw Torque Specifications below. Safety wire or another suitable means will be used to ensure that the sight glass encasement and inlet flange screws do not loosen.

Table A- 1: Test-section Housing Screw Torque Specifications

Inlet Flange Screws	50 – 60 (5.6 – 6.8)	in·lb (N·m)
Encasement Screws (top)	65 – 75 (7.3 – 8.5)	in·lb (N·m)
Threaded Rods (bottom)	36 – 48 (4.1 - 5.4)	in·lb (N·m)

The low torque specified for the integral flange encasement screws is to reduce stress on the rim of the screw head flange and the top edge of the counter-bores in the sight glass encasement which hold the O-rings. This counter-bore greatly reduces the contact area between the flange of the screw and the top surface of the sight glass encasement. The pressure force acting on the four sight glass encasement bolts at an internal pressure of 60 psig (maximum intended operating pressure, although usually pressure will be within 30 psig) is approximately 480 pound-force per bolt. The mechanical advantage of the screw at the minimum torque specified leads to approximately 1000 pounds of tensile force per bolt (considering friction) which means that the maximum pressure will not be able to unseat the sight glass encasement from the test-section housing because of insufficient bolt tension. If test-section internal pressures are kept within 30 psig, up to a 12% increase in encasement screw torque is permissible. The threads of these screws should not be lubricated. To further reduce possibility of damage to the test-section sight glass encasement housing due to the screw head flanges, only hard O-rings, such as those made out of Teflon, should be used.

Due to the small contact area associated with the flange of the bolt, the normal stress between the screw head flange and the encasement, including the pressure force from 60 psig of internal pressure, may cause some localized deformation in the encasement housing at maximum torque and pressure the first time the test-section is pressurized. The screw heads would not be affected. This analysis is based on estimates of the strengths of the stainless steel screw material and the 316/316L stainless steel material of the encasement. Therefore, it is recommended to tighten these screws to maximum torque, proof test the test-section at 90 psig, and re-tighten them before operating the test-section in the flow-loop. This will ensure that the localized deformation has already occurred prior to testing for long times with thermal cycling, reducing the likelihood of the screws loosening later during testing and steam leaks forming at the junction between the sight glass encasement and the housing.

A.1.5 Inlet Separator Plate and Flow Reduction Halves.

To enable the proper development of thin-film annular boiling flows, it has been found in past experiments with FC-72 [1] that it is necessary to keep the liquid and vapor separate during their entrance into the flow channel. The design here is one in which a separator plate is sandwiched between two flow reduction halves. These flow reduction halves are represented as CAD models in Figure A-2 and Figure A-3. The upper half has a pocket which lines up with the steam inlet port at one end and the test-section flow channel on the other end. The lower half has a pocket which lines up with the liquid water inlet port at one end and the test-section flow channel at the other end. Pictures of the unfinished flow reduction halves are shown in Figure A-16; they have since been completed, along with the separator plate, and installed in the test-section housing.

The separator plate fits tightly between the flow reduction halves when installed in the test-section housing. It has O-ring sealing in locations where there is not much material overlap, such as where it interfaces with the inlet flange and where it interfaces with the flow reduction halves near the entrance of the flow channel. The CAD drawing of the separator plate is shown in Figure A-17 below.

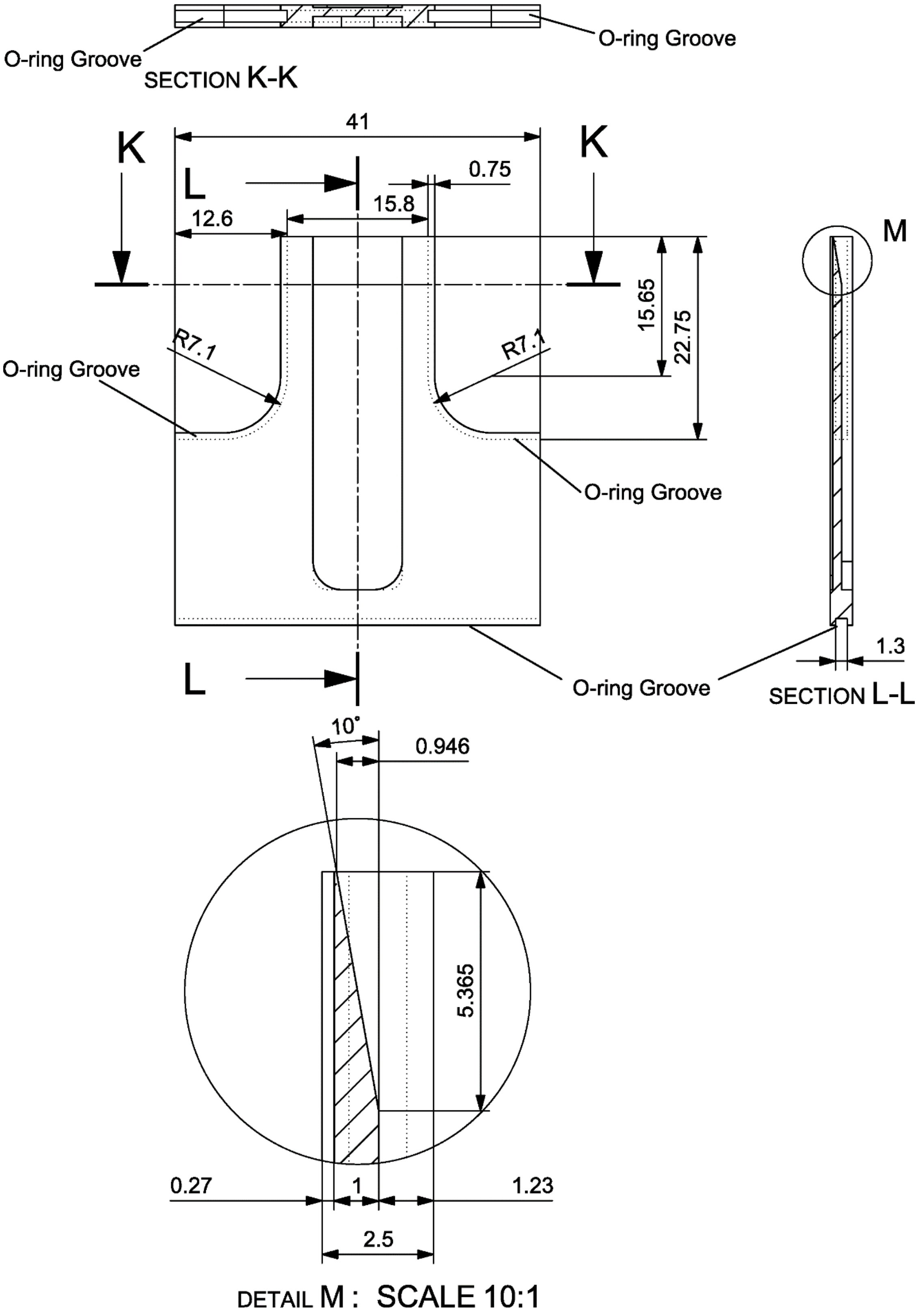
O-ring Groove
SECTION K-K
O-ring Groove
41
K
K
L
0.75
15.8
12.6
15.65
22.75
R7.1
R7.1
O-ring Groove
O-ring Groove
M
L
O-ring Groove
1.3
SECTION L-L
10°
0.946
5.365
0.27
1
1.23
2.5
DETAIL M : SCALE 10:1

Figure A-17 Test-Section Separator Plate Sample CAD Drawing. Dimensions are in millimeters.

The separator plate was designed to fit completely within a pocket machined within the lower flow reduction half. A reduction in the thickness of the separator plate where the flows converge, tapered from the steam side, helps reduce the formation of turbulent vortices due to flow separation. The gap height in the completed separator plate is approximately 0.25 mm on the liquid side and 1.25 mm on the steam side. On the steam side, an additional 2.5 mm of gap height is added by the adjacent pocket in the upper flow reduction half. The overall thickness of the separator plate is 2.5 mm, and its thickness between the two flows is 1 mm, tapering down to approximately 0.5 mm at the downstream end.

An indexing dowel pin of 5 mm diameter and 12 mm length was used to fix the angular position of the inlet flow reduction halves and separator plate within the test-section housing, since their outer surfaces are cylindrical when assembled. The hole for this pin is visible toward the left of the cut-away view in Figure A-3.

While the flow reduction halves were machined from 316/316L stainless steel, the separator plate was machined out of Nickel 200, which is easier to machine than 316/316L stainless steel and has a much higher thermal conductivity. The higher thermal conductivity of the separator plate would reduce the temperature difference between the liquid and vapor phases before they come together; the resulting reduction in sub-cooling of the liquid water when it enters the channel will make it easier to suppress nucleation in the thin liquid film. Nickel 200 has a similar or greater corrosion resistance compared with 316/316L stainless steel.

A.2 Steam Generator

The Steam Generator is a 24kW (480 Volts, 27 amps, 3 phase) vessel manufactured by Infinity Fluids. The model number is CRES-SG-48-0240-K-3P. This device is the source of providing vapor at the required pressure and flow rate to the flow loop. The maximum volumetric capability of this device is 82 (lbs/hr) which is about 10.33 (gr/sec). The vessel is made of Stainless Steel 316L to be highly corrosion resistant. There is a sight glass installed on this device to indicate the water level in the vessel and operator makes sure dry-out won't happen during the operation of the flow loop. Below is a figure of this device. The Steam Generator has three ports. One of liquid inlet to the vessel which supplies liquid water into the component. The other one is vapor outlet which eventually this flow goes into the flow channel. The last one is a safety relief valve which makes sure pressure will be released if any blockage happens in the flow loop.

The Steam Generator is controlled through Data Acquisition Hardware and software developed for this system. Pulse width modulations at 30 Hz are sent into the control box to control the solid-state relays which determines the power output from the helical heater inside the Steam Generator. Flow loop schematic shows the steam generator location on the flow loop.

There are a pressure transducer and thermocouple installed in the vessel as well which gives accurate simultaneous working pressure and temperature of the vessel. This data is essential for operating the flow loop since it gives the upstream working temperature and pressure of the loop which is important for controlling flow channel operation pressure.

A.3 Coriolis Flow Meters

There are three Coriolis flow meters (Composed of the sensor + transmitters) installed in the flow loop. First one is at the inlet vapor line, second one is on the inlet liquid line and third is on outlet liquid line. These flow meters are able to give accurate mass flow rate values of the inlet and outlet flows in the channel. These flow rate values are critical variables for operating the flow loop since it can give the energy balance across the flow channel which will be used to verify the amount of heat being removed from the channel. Coriolis flow meters give output signal of 5-20 mA which is converted to 0-10 Volts to be able to read thorough input DAQ module.

These flow meters have been calibrated by the manufacturer and also the calibration has been verified using the Emerson software which verifies the calibration and also it was used to verify the reading that was acquired and recorded through the LabVIEW.

A.4 Super Heaters

Superheaters are type of heaters that make sure the vapor that is going through the channel are superheated and no condensation happens inside the channel. I have installed two super heaters in flow line after the Steam Generator as shown in flow loop schematic figure A1. The first super heater is an inline immersion heater 1kw which is threaded into the 1'' piping. The second super heater is a wraparound heater which is in the downstream of first super heater with power of 1.5 kW. PID controllers are defined and implemented in the LabVIEW software to control these super heaters. The feedback signals for these heaters are the temperature thermocouples that installed in the downstream of each heater in the direction of the flow which will be used to control the flow temperature accurately within ± 0.5°C.

A.5 Pressure Transducers

A.5.1 Absoluter Pressure Transducer (APT)

There are totally 5 absolute pressure transducers installed in this system. The pressure transducer model is ETM-624-312M-12BARA manufactured by Kulite. The specificsation can be found online. These traducers are installed at the critical locations which live recording and monitoring the pressure is essential. Out of five transducers, two are installed on the inlet and outlet of the flow channel to give accurate value of pressure. One is installed in the Steam Generator and two are installed at the liquid and vapor outlet in the downstream of flow channel exit as it is shown in Figure A-1. These transducers have signal output in the range 0-10 volts which goes into the data acquisition hardware.

The pressure transducers have been calibrated inhouse periodically to make sure of pressure values reading are accurate and precise.

A.5.2 Differential Pressure Transducer (DPT)

There is a differential pressure transducer installed on the top of the flow channel indicated in Figure A-1. This transducer is connected in the same line with the APT in the channel. It will be used to verify the values reading from the two APTs.

A.6 Condenser

Condenser is located in downstream of vapor outlet from the flow channel as it is shown in the flow loop schematic in Figure A-1. It is a shell and tube counter-flow condenser which condenses all the vapor produced through the test section and steam generator back into the liquid.

A.7 Liquid Vapor Separator

The L/V separator is a narrow vessel holding approximately 2.5 liters. Its purpose is to provide opportunity for any steam leaving the condenser to condense before entering the liquid lines. It also serves as a low pressure sink for the liquid water exiting the test-section and operates at nearly the same pressure as the condenser. The L/V separator is not insulated to ensure that the liquid exiting it is sufficiently sub-cooled not to re-boil in the liquid lines while remaining close enough to its saturation temperature to reduce thermal transients.

A.8 High Speed Camera

High speed camera (APX model) installed on top of the test-section to record the flow inside the channel. This camera makes sure that the assumption of annular two-phase flow is verified visually. It is also used to verify the existence and an estimation of micro/mili nucleation bubbles formed in the liquid flow.

A.9 Accumulator

The Accumulator is designed and manufactured in-house out of stainless-steel material. It is basically a pressure vessel with volume of 9.8 Liters. It is used as a reservoir to supply or store excess water whenever necessary. The water stored inside needs to be only a few degrees Celsius subcooled compared to the steam generator outlet steam to decrease the thermal inertia in the steam generator and Flow-Loop. There are 5 band-heaters with total power of 6 kW strapped around the vessel with 6 thermocouples, 1 pressure gauge and 5 controllers (in the associated control box) to be able to control and monitor the temperature, pressure and power. The role of this accumulator is very critical because first it allows accommodation of larger range of flow rates and operating powers into the flow-boiler (test-section). Secondly it decreases the unsteady operating time in between the steady state runs significantly, which used to be a challenge in the FC-72 flow-loop of Attachment-2 and [1].

A.10 Inline Heater

The inline heater is a 2000 watts immersion heater installed in the liquid line in the upstream of the liquid inlet to the test section. It has the role to preheat the water close to saturation temperature (1-2°C) at the inlet pressure of test-section channel. The wattage into this heater is adjustable and is manually controlled to get close to saturation temperature based on feedback from thermocouple in the liquid inlet. (Refer to Figure A-1 flow-loop schematic)

A.11 Pumps

There are totally three pumps installed in the flow-loop that would circulate the flow across the whole system.

A.11.1 Rotary Vane Pump

Th rotary vane pump is located at the inlet of Steam Generator and has the role to supply liquid water into the vessel. It has the maximum capacity of 15 (gr/sec) which is well above the critical liquid flow rate needed to supply to the Steam Generator. (Refer to Figure A-1 flow-loop schematic).

A.11.2 Gear Pump

The gear pump is at the upstream liquid inlet to the test-section and is responsible for supplying liquid water to the test section. It is both manual and computer controlled through the LabVIEW. The pump is able to provide a volumetric flow rate up to 400 (mL/min).

The gear pump provides a pulseless flow to the channel. This is essential to have liquid flow as a thin film into the channel.

A.11.3 Peristaltic Pump

Peristaltic pump is located at the liquid test-section outlet after the pressure transducer as it is shown in Figure A-1 flow-loop schematic The main reason for having this pump is to provide enough pressure in the liquid outlet downstream to not allow any vapor at the stagnation chamber at the end of housing shoves into the liquid line. After several initial runs and observations, it was seen through the sight-glass (right after the liquid outlet shown in Figure A-1 flow-loop schematic) that vapor and liquid both are getting though the liquid line because of high pressure at the stagnation chamber. This pump helps to stabilize the pressure at the stagnation chamber which causes steady level of liquid in the chamber.

A.12 Filters, Valves, Fittings and Pipes

There are several filters, ball valves, needle valves installed at various location across the clos channel. These fittings help to control, stabilize, leak test, and properly circulate the flow across the flow-loop.

A.12.1 Filters

There are filters installed in the flow loop to remove any particle that can damage the critical components in the system. First one is installed before the gear pump. The reason being that this pump head is very sensitive to any debris or unwanted particles and can be damaged, so it is essential to have this filter. The second filter is before the Steam Generator inlet port. This filter has the role to remove all the debris that flow through loop and prevent them to enter the steam generator and into the test-section accordingly.

A.12.2 Valves

The ball valves have several applications in the loop. One is to isolate specific part of the system for leak test. Second, they allow to manually adjust and control the pressure across the flow loop. Third, they are used to redirect the flow in specific path and during drainage process after the operation.

Needle valve has slightly different story, its presence is critical for fine tuning the pressure and flow rate across the loop. The critical location for needle valve is valve number 2 which is in between the vapor outlet and condenser. Because in the condenser all the vapor condenses into the liquid the pressure significantly drops, needle valve acts as a barrier between the high pressure and low pressure side for an smooth transition in pressure drop.

A.13 Structure

The support structure or frame work of both the Flow-Loop and tests section is, 1-5/8" x 1-5/8", zinc-plated Unistrut. The size of the frame is 3 feet wide, 5 feet high and 8 feet long. There are two levels of 0.075 inch thick carbon steel sheet, at 1 foot and 5 feet above the floor, on which most components are installed. Additionally, to keep the operator safe from any steam leakage, a transparent polycarbonate wall is installed in between the computer user and the flow-loop.

A.14 Computer & DAQ

Data from temperature, pressure, and flow rate sensors will be recoded through the data acquisition hardware and software. The data acquisition (DAQ) hardware is composed of a cDAQ-9178 National Instruments chassis (Compact DAQ). The modules installed in this chassis are: one NI 9205 analog input module, one NI 9215 simultaneous sampling analog input module (for obtaining dynamic test-section pressure data), two NI 9213 thermocouple input modules, one NI 9211 thermocouple input module, and one NI 9264 analog output module. The analog output module allows us to control the speed of the pumps, the automatic control valves, and the super-heater and test-section heaters; while the analog input module records the pressure transducers, flowmeters, thermocouple probes and pump speed. The cDAQ chassis and modules are shown in Figure 18 below. LabVIEW 2015 edition is the designated software for the communication with the DAQ hardware.

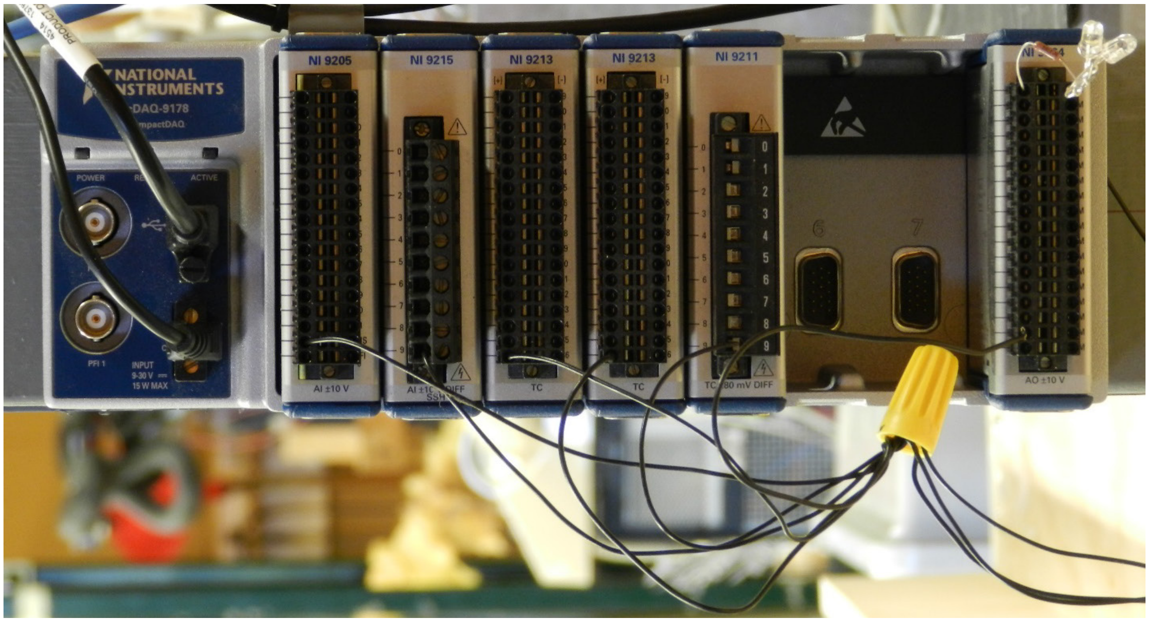

Figure A-18 National Instruments Compact DAQ Chassis and Modules.

A.14.1 Auxiliary National Instruments DAQ Hardware

An SCXI-1503 module with an SCXI-1306 terminal block, an SCXI-1120 module with an SCXI-1303 terminal block, and an SCXI-1121 module with an SCXI-1303 terminal block will be used in an SCXI-1000 chassis to process additional thermocouple probe data from the test-section, as needed. The SCXI-1000 chassis is connected to an NI PCIe-6321 DAQ card in the computer. This SCXI system will also be accessed through the LabVIEW 2015 software.

A.15 Other Components

There are other components used in the flow-loop as well which are shown in Figure A-1 including different types of valves such as ball valves, needle valves, check valves and relief valves. There are also strainers and a filter which removes particles from the main flow-loop water. Stainless steel pipes and various fitting from 1’’ to 1/16’’ size were also used in the flow-loop. In places where it was necessary to monitor pressure, but recording was not needed, pressure gauges were implemented.

Figure A-19 The Flow-Loop Test Stand and Equipment.

In Figure A-19, the steam generator control box is the large grey panel on the front of the test-stand. The steam generator vessel is in the front left corner. The two horizontal pipes on the upper level before the Coriolis flowmeter will be wrapped with the super-heater elements. The Coriolis flowmeter is in the middle at the front on the upper level. The test-section is in the background on the upper level toward the left. After validation testing, the test-section will be inserted where the straight section of pipe is to the right of the Coriolis meter. The condenser is mounted vertically at the back right corner; it extends above and below the upper level. The L/V separator is located underneath the condenser on the lower level. The white peristaltic pump after the L/V separator is toward the front of the lower level, just to the right of center. The accumulator vessel is at the back of the lower level in the center, but it is mostly hidden from view by the steam generator control box. The second white peristaltic pump, between the accumulator and the steam generator, is visible immediately behind the steam generator vessel. The back of the gear pump drive is visible underneath the steam generator control box. Three pressure gauges are visible. The dedicated electrical panel and some of its receptacles are visible on the back wall.

Figure A-20 Flow-Loop, Computer and DAQ Hardware.

In Figure A-20, the black computer tower is just to the right of center in the foreground. The Compact DAQ (cDAQ) chassis and modules are vertically mounted on the frame of the safety wall toward the center of the picture. The unpainted cable tray is for signal wires. The painted cable tray behind the safety wall is for power cords. They grey box with the black front panel just to the right of the monitors is the control box for the accumulator. The SCXI chassis and terminal blocks are visible on the red mat on top of the desk. The FC-72 flow-loop is visible in the background on the far left.

B Details of Conjugate conduction-convection numerical simulation procedure presented in section 3.3.1

Problem objective:

The main objective of the problem is to obtain the following local boiling surface parameters: $q''_w(x)$ and $T_w(x)$ (shown in Figure B-1) as obtained from iteratively calculated and applied values of local boiling surface heat transfer coefficient (HTC) h_x along with iteratively adjusted control volume heat loss rates (in W) such as $\dot{Q}_{loss\text{-}top\text{-}casing}$ from top casing enclosure and $\dot{Q}_{loss\text{-}bottom\text{-}casing}$ from bottom casing enclosure (shown in Figure B-2).

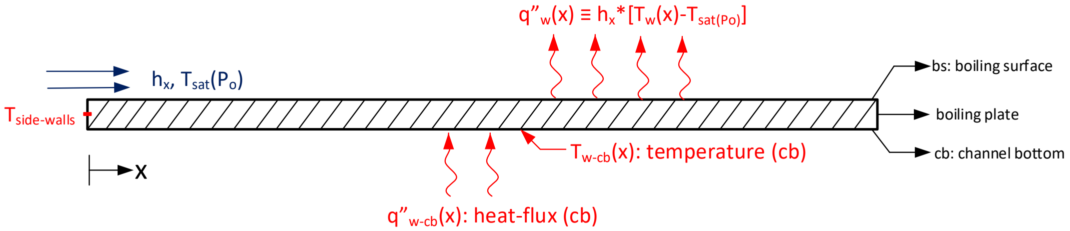

Figure B-1: A schematic of the boiling-plate with required and to be obtained boundary conditions.

It may look, at first, surprising as to how one can predict two thermal boundary conditions – viz. $q''_w(x)$ and $T_w(x)$ – for the boiling-surface in Figure B-1 (note that Figure B-9 depicts a representative schematic of the copper channel's isometric view with boiling surface shown therefore which the mentioned thermal boundary conditions are being obtained). The answer lies in the fact that experimental measurements must be designed to be such that we completely or partially (in this case only partial knowledge was feasible) know the two thermal boundary conditions – viz. $q''_{w-cb}(x)$ and $T_{w-cb}(x)$ - for the channel-bottom-surface of the thick plate that forms the copper channel shown in Figure B-7 and B-9. The 3-D ANSYS-based steady conduction analysis approach and the algorithm presented here makes the partial knowledge of these two thermal boundary conditions for the channel-bottom of the copper plate complete and yields the two values of $q"_{w-cb}(x)$ and $T_{w-cb}(x)$ for the bottom surface as well as h_x and $T_{sat}(p_0)$ – from which one obtains $q"_w(x)$ and $T_w(x)$ - for the boiling-surface. This completion of initially partial knowledge of the two thermal boundary conditions $q"_{W\text{-}cb}(x)$ and $T_{W\text{-}cb}(x)$ in Figure B-1 as depicted in Figure B-8 is achieved by making sufficient amount of temperature measurements elsewhere in the top and bottom casings for the flow-channel. This is followed by sub-system conduction analyses with iteratively guessed values of h_x - while requiring that the predicted temperature values agree with the additional measurements elsewhere on the 3-D solid model (which includes casings connected to the flow-boiling channel). This approach, to our knowledge, is a unique and is a first of its kind way of obtaining semi-experimental estimates of local values of boiling-surface HTC h_x.

Nomenclature:

bs: boiling surface

cb: channel bottom

$\dot{Q}_{loss\text{-}top\ casing\text{-}ambient}$: Heat lost to T_{surr} from top casing enclosure

$\dot{Q}_{loss\text{-}bottom\ casing\text{-}ambient}$: Heat lost to T_{surr} from bottom casing enclosure

α: Leakage factor

h_x: Local boiling surface heat transfer coefficient

$R_{tc\text{-}i}$: Interfacial thermal contact resistances between heater blocks and channel bottom surface

h_{tc}: an assumed heat transfer coefficient on top casing

$\dot{Q}_{HB\text{-}i\text{-}cartridge}$: Heat input for each heater block (i = 1:3)

$q"_{HB-(i)-cartridge}$: Heat flux input for each heater block (i=1:3)

$\bar{h}_{HB-i}$: Heat transfer coefficient applied on the air exposed exterior surfaces of each heater block. (i=1:3)

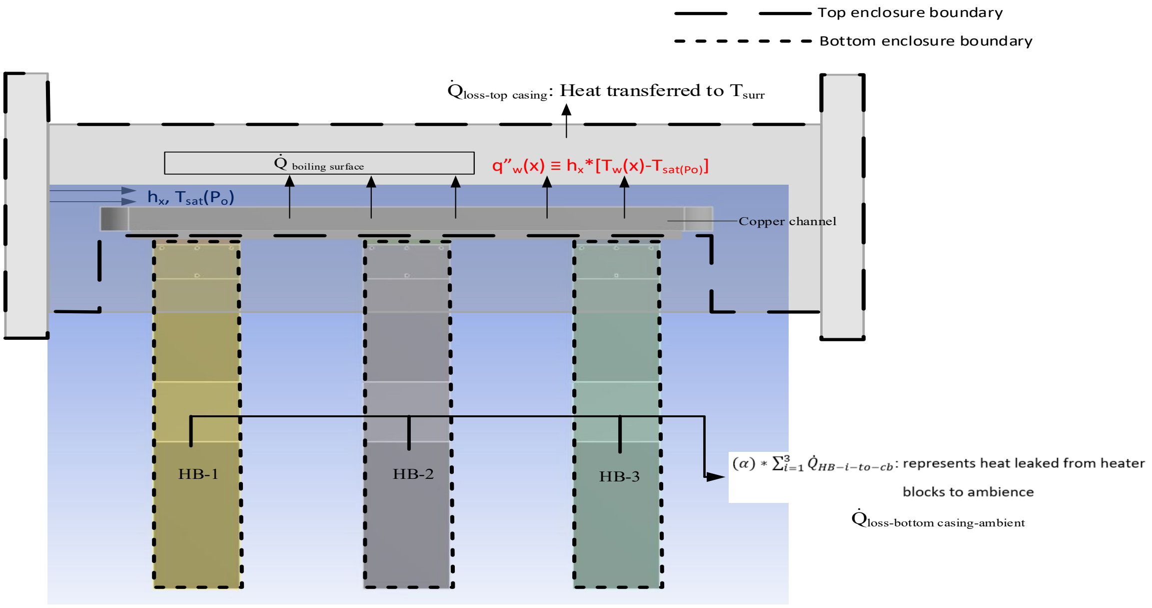

Figure B-2: Schematic of the test section geometry with depiction of boiling surface and control volume parameters.

However, to obtain the required parameters, various auxiliary parameters such as $q''_{HB-(i)-cartridge}$, $\bar{h}_{HB\text{-}i}$, $\sum_{i=1}^{3} \dot{Q}_{HB-(i)-to-CB}$, $R_{tc\text{-}i}$, q''_{cb}, $\bar{h}_{tc}$ and α (heat leakage factor) must be obtained. The auxiliary parameters are shown in Figure B-3 (nomenclature given in the page above)

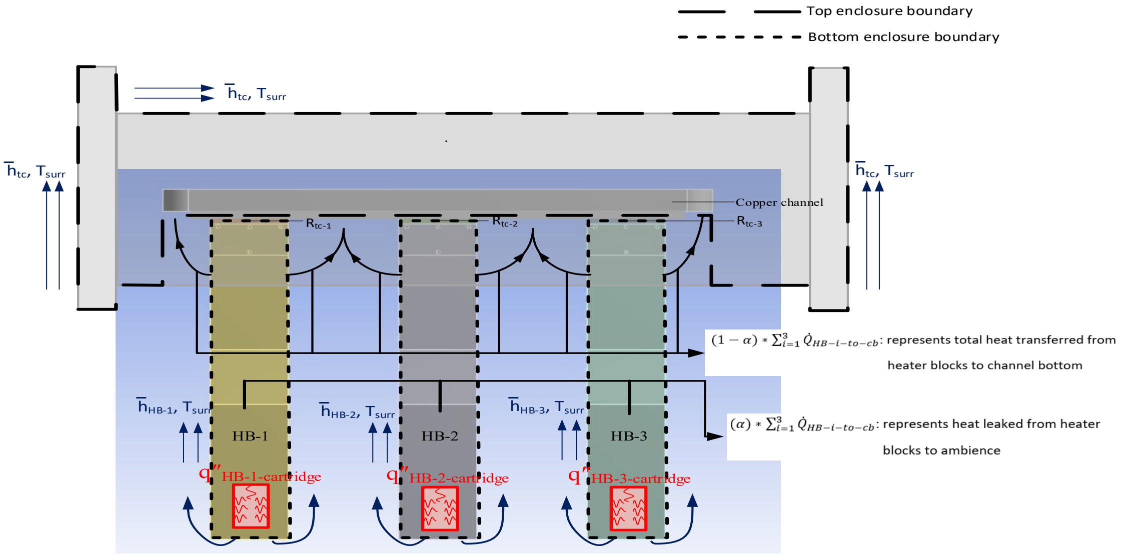

Figure B-3: Entire test section geometry with auxiliary parameters as defined in the above paragraph.

*$q"_{CB-i}$ is $\dot{Q}_{HB-(i)-to-CB}$ divided by the corresponding area of the air exposed channel bottom surface. As heat input of each heater block is different, $q"_{CB-i}$ varies for each channel bottom surface (these surfaces are defined in Figure B-7).

Step 1: Individual Heater Block Analysis:

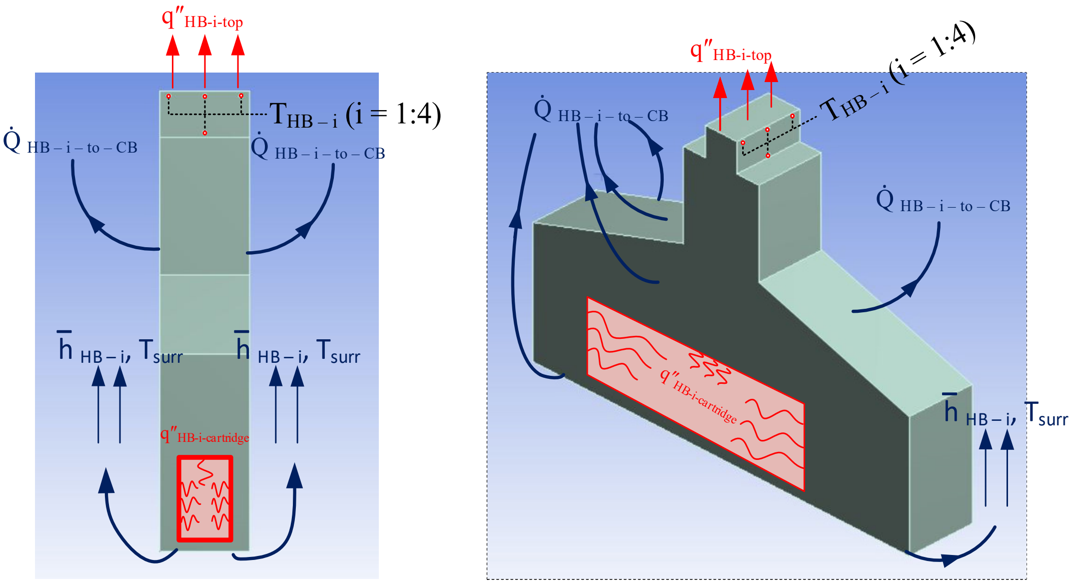

(a) **(b)**

Figure B-4: (a) Side view of the heater block with depiction of utilized boundary conditions**. (b)** Isometric view of the same

Experimentally known $q"_{HB-(i)-cartridge}$ and analytically calculated $q''_{HB-i-top}$ (from available temperatures T_{HB-i}, measured at four locations as shown in Figure B-4 (a and b) are used as known boundary conditions in this step to find out $\dot{Q}_{HB\text{-}(i)\text{-}to\text{-}CB}$. A combination of guessed heat transfer coefficient $\bar{h}_{HB-i}$ and a representative ambient temperature T_{amb} is used as boundary condition to the find the heat transfer from each heater block to channel bottom. Initial guess begins with choosing $\bar{h}_{HB-i} \approx 25$ W/m^{2}K. After observing the temperatures ($T_{HB\text{-}i}$) predicted by Ansys CHT simulation module, $\bar{h}_{HB-i}$ is changed iteratively until predicted temperatures are in close agreement (± 0.5 °C) with experimentally measure values, those being T_{HB-I} (i = 1:4).

This analysis provides us with two important outputs, heat leaked from each heater block i.e., $\dot{Q}_{HB-(i)-to-CB}$ (see Figure B-4 a and b) from all air exposed faces (top face is not exposed, it is in contact with channel bottom surface) and an appropriate $\bar{h}_{HB-i}$ for each case and each heater block. Having a reasonable $\bar{h}_{HB-i}$ from i = 1:3, provides a reasonable first estimate of $\bar{h}_{tc}$ (heat transfer coefficient applied on Top casing enclosure). As a first guess $\bar{h}_{tc}$is assumed to be average of three measures of $\bar{h}_{HB-i}$ i.e. “$(\sum_{i=1}^{3} \bar{h}_{HB-i})/3$. Iteration procedure for $\bar{h}_{tc}$ is explained at the ending of step 3.

Step 2: Finding thermal contact resistance between each heater block and copper channel

As a first estimate, the following are used:

$$R_{tc-(i)} = \Delta T / q'' \tag{B.1}$$

$$\Delta T = T_{HB-i} - T_{avg-cb-i} \tag{B.2}$$

$$q'' = \dot{Q}_{HB-i-top} / (\text{Top Area of heater block}) \tag{B.3}$$

(where $T_{avg-cb-i}$ is the average temperature of the channel bottom surface just above the corresponding heater block, for example, $T_{avg-cb-i}$ is the average of a_2,b_2 and b_4)

Step 3: Implementing initial guess of average heat transfer coefficient over the boiling surface using available copper channel bottom temperatures

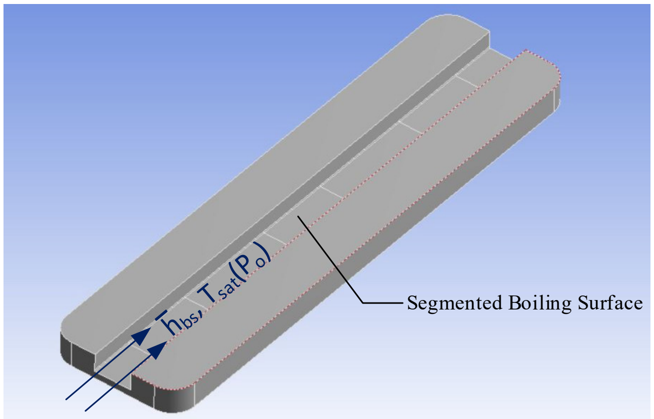

Figure B-5: Isometric view of the copper channel with $\bar{h}_{bs}$ and $T_{sat(Po)}$ defined as boundary conditions on the boiling surface as initial guess, initial guess strategy is given below. Note that the average heat-flux for the entire "bs" is given by:

$$\bar{q}''_w \equiv \bar{h}_{bs} * [\bar{T}_w - T_{sat(P_o)}] \tag{B.4}$$

Calculation strategy for guessing initial $\bar{h}_{bs}$: In the above equation $\bar{q}''_w$ is assumed to be the ninety percent of the total heat input (divided by channel top surface area). Ten percent ($\alpha = 0.1$ in Figure) of the total heat input from cartridge heaters is assumed to be leaking to the surroundings through top casing enclosure (see Figure B-6). $\bar{T}_w$ is guessed using computed average of channel bottom temperatures (shown using red circles in Figure B-7) available from experimental data. To begin with [($T_{\text{bottom wall avg}} - 1$)°C] is chosen as the first estimate of $\bar{T}_w$ assuming only 1°C drop from bottom surface to the top surface to calculate initial guess of $\bar{h}_{bs}$. Saturation temperature $T_{sat(p_o)}$ is also obtained from experimental data (since fluid is known to be pure water and representative pressures are nearly equal to the known inlet pressures p_o).

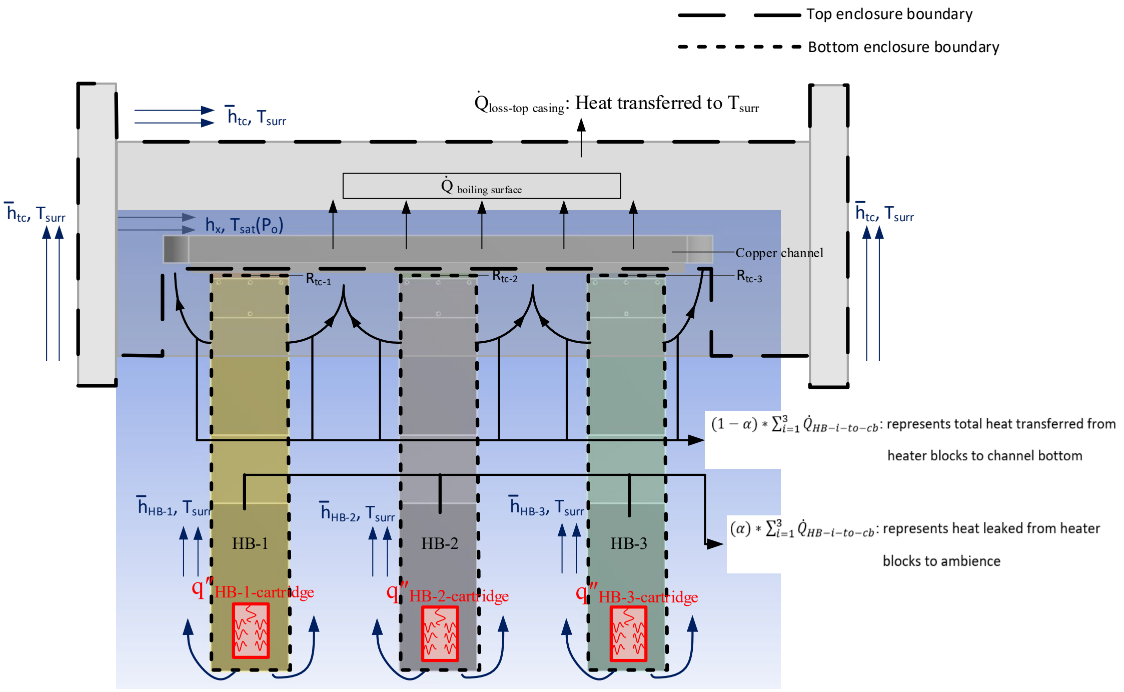

Figure B-6: Entire test geometry with all the boundary conditions shown.

Input: Initial specification for boundary conditions: (following a bottom to top approach for describing the boundary conditions, see Fig B-6)

- $q''_{HB-(i)-cartridge}$ applied on cartridge surfaces of each heater block available from experimental data.
- "$\bar{h}_{HB-i}$" and "T_{surr}" on the heater block surfaces, obtained from step 1.
- "R_{tc-i}" on the interface of heater blocks and copper channel bottom surface, (initial estimates from step 2).

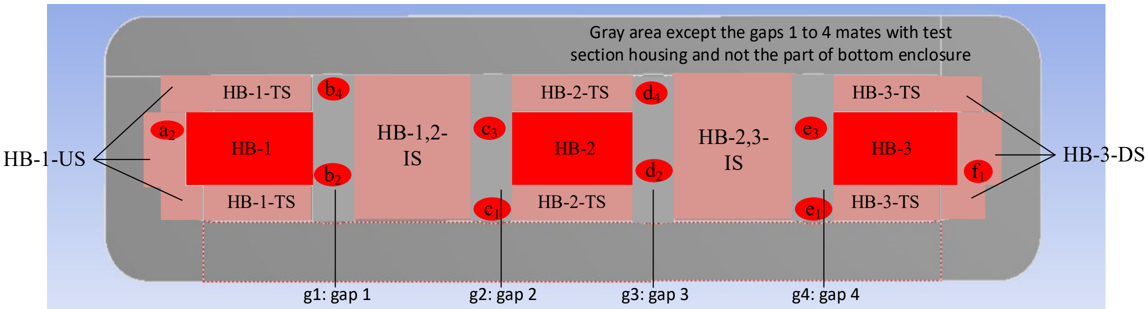

Figure B-7: Copper channel bottom surface, refer Figure B-8 for boundary conditions

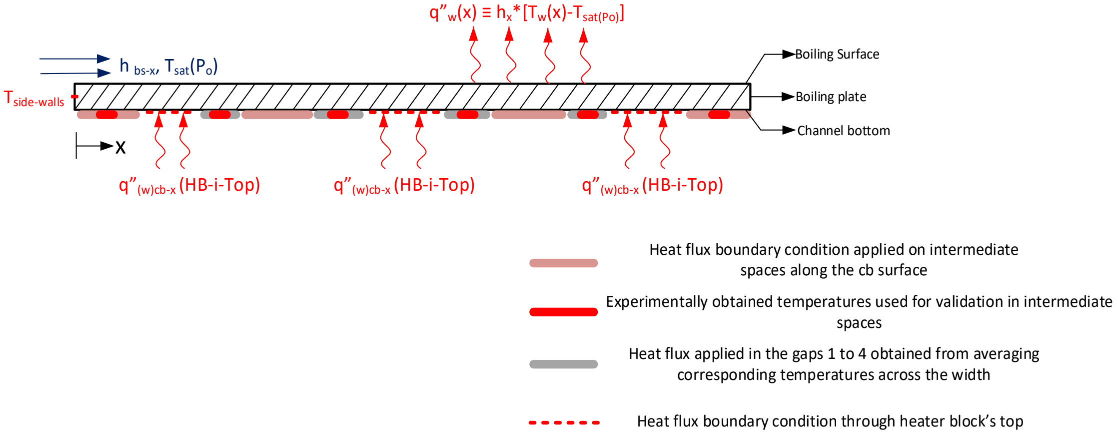

Figure B-8: Schematic of applied boundary conditions on all surfaces of copper channel

- Assuming leakage factor (α) to be zero i.e., 100% of the heat removed from three heater blocks ($\sum_{i=1}^{3} \dot{Q}_{HB-(i)-to-CB}$) is being applied as q''_{w-cb-i} on each exposed channel bottom surface corresponding to heater block (i). $\dot{Q}_{HB-(i)-to-CB}$ is divided by the corresponding area of the air exposed channel bottom surface and applied on HB(i) upstream, transverse and intermediate surfaces (defined as US, TS and IS respectively, see Figure B-7). For example, one third of the heat removed from heater block 1 is applied on HB-1 upstream (US), one sixth on each transverse surfaces(TS) and one third on the intermediate space(IS).

- Heat flux values in the intermediate spaces are obtained by using above-mentioned method. However, a different strategy is implemented to obtain heat flux values in the gaps (i = 1:4). Experimentally obtained temperatures available in a gap are averaged and applied in the corresponding gap, this enables ANSYS fluent to provide a post-processed heat flux value. The obtained or post processed heat flux values are applied in the gaps as a boundary condition in an iterative way until the corresponding ansys predicted gap temperatures are in reasonable agreement with the corresponding experimentally measured temperatures. For further reducing the error or achieving closer agreement with experimental temperatures, heat flux applied as a boundary condition on the intermediate spaces on the channel bottom surface (q''_{w-cb-i}) is reduced by a leakage factor (α) which will lead to further improvements in converged values (details of error minimization principle are given in step 5 of the current appendix). Hence both the heat flux obtaining steps can lead to complete knowledge of heat-flux boundary condition throughout the channel bottom surface.
- "$\bar{h}_{bs}$" on the boiling surface are obtained from equation B.4. – where $T_{sat}(p_0)$ is known from pressure measurement.
- "$\bar{h}_{tc}$" is initially assumed to be the "$(\sum_{i=1}^{3} \bar{h}_{HB-i})/3$" and a chosen value of "T_{surr}" is taken from an experimental measurement of the surrounding air inside the enclosure.

Output: By applying the above-mentioned boundary conditions and solving using ANSYS Fluent, we obtain the following:

- Channel bottom temperatures: a_2 to f_1 (colored red in Figure B-7) are computationally obtained and compared with measured values.
- Two flange temperatures (are also computationally obtained and compared with measured values). Two flange temperatures are located on top enclosure.

- $\mathrm{T}_{\mathrm{avg-cb-i}}$ (at the channel bottom surface are also computationally obtained and its average provides improved estimates of Rtc-i in equation B.2.
- $T_{HB\text{-}i}$ (are also computationally obtained and compared with measured values, which in turn used to obtain $R_{tc\text{-}i}$ using computationally obtained $\mathrm{T}_{\mathrm{avg-cb-i}}$.
- Heat-flux values $q''_{HB\text{-}i\text{-}top}$ obtained in step-1 through sub system of Figure B-1 are extracted from the solution. For the system in Figure B-3 and compared to ensure that convective values always yield compatible results.

How the above predicted/computed temperatures are used to arrive at a final and appropriate estimate of "$\bar{\mathrm{h}}_{\mathrm{bs}}$" on the boiling surface, "$\bar{\mathrm{h}}_{\mathrm{tc}}$" and $R_{tc\text{-}i}$ will be explained in the next few paragraphs.

Iterating for $R_{tc\text{-}i}$:

Iteration procedure for $R_{tc\text{-}i}$ (i = 1:3) is dependent on temperatures – "$T_{HB\text{-}i}$ and $\mathrm{T}_{\mathrm{avg-cb-i}}$". R_{tc}-is are altered by computing the $T_{HB\text{-}i\text{-}Top}$ temperatures predicted by ANSYS after every iteration of step-3. If the predicted temperatures are above experimental temperatures, then $R_{tc\text{-}i}$ must be reduced and vice versa. This is done for a few run cases in Table–1,2 after that is found that the same approximate constant $R_{tc\text{-}i}$ values hold for each run case in Table–1,2.

Iterating for "$\bar{\mathrm{h}}_{\mathrm{bs}}$":

Initial simulation result of the entire geometry provides average (first estimate) of channel bottom temperatures a_2 to f_1 (colored red in Figure B-7). If the estimate of the average of these temperatures (a_2 to f_1) is above the expected or experimental average, "$\bar{\mathrm{h}}_{\mathrm{bs}}$" must be increased to bring down the temperatures a_2 to f_1 and vice versa. In this way, by using experimental copper channel bottom temperatures, through an iterative process, we arrive at a reasonable estimate of average "$\bar{\mathrm{h}}_{\mathrm{bs}}$".

Iterating for "$\bar{\mathrm{h}}_{\mathrm{top-casing}}$":

"$\bar{\mathrm{h}}_{\mathrm{tc}}$" Which is, "$(\sum_{i=1}^{3} \bar{\mathrm{h}}_{\mathrm{HB-i}})/3$" and experimentally available "T_{surr}" are used as initial boundary conditions on the top casing. This also yields flange temperatures estimate from

ANSYS Fluent solutions. The obtained temperatures will vary from experimental temperatures since $\dot{Q}_{loss-top-casing}$ is not exactly 10% as per the assumption implemented using equation B.4 and it varies from case to case and iteration to iteration. According to the predicted temperatures, analytically altering "$\bar{h}_{tc}$" in an iterative process result in predicted temperatures, which are in close agreement with experimental flange temperatures. (± 0.5 °C).

Step 4: Implementing monotonically increasing heat transfer coefficient along the boiling surface

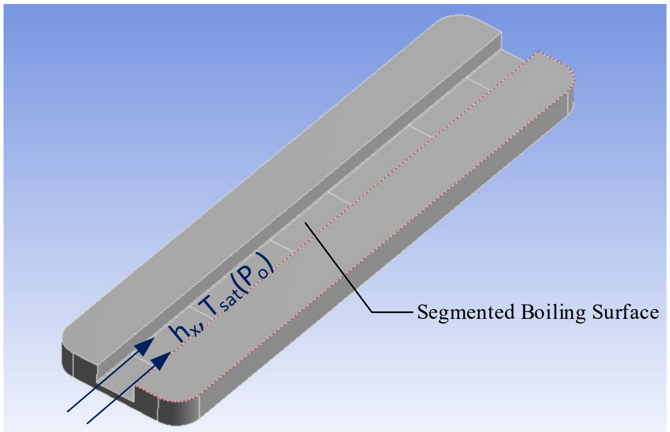

Figure B-9: Channel boiling Surface with segmentation done along the length of the channel

Procedure until step 4 provides us $\bar{h}_{bs}$ over the entire boiling surface. However, h_x correlation results presented by Kim and Mudawar, Dorao et al. etc., (shown in Figure B-13) indicate a monotonically increasing h_x trend along the length of the channel for the fluid and parameter ranges considered, so imposing an increasing trend makes more scientific sense. Also, plots of copper channel bottom temperatures indicate a decrease in temperature, lengthwise. This also bolsters that h_x must have an increasing trend. Hence, the boiling surface is segmented in ANSYS design modeler to implement a monotonically increasing h_x. A physics-based conjecture is that for this type of annular flows (not too thin), nucleation rates improve with distance despite some reduction in liquid thickness.

Step 5: Decreasing the heat input on the channel bottom surface and arriving at a justifiable heat input percentage using error minimization principle

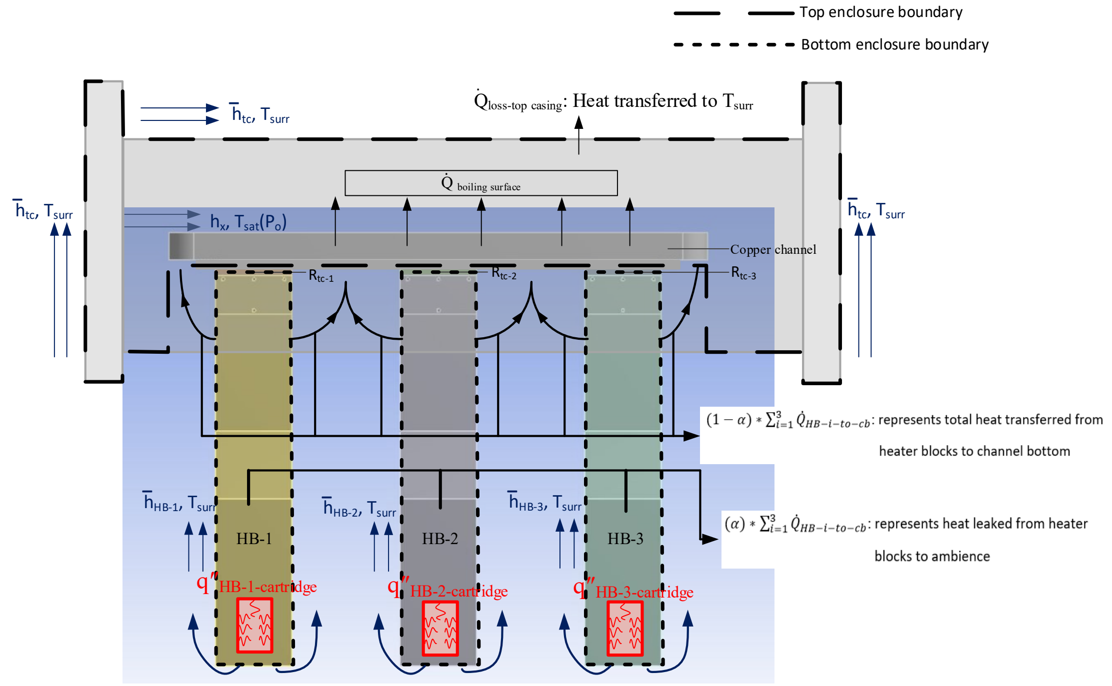

Figure B-10: Entire section geometry, with all the applied boundary conditions presented.

In the first few iterations up to step 3, α is zero i.e. 100% of $\sum_{i=1}^{3} \dot{Q}_{\mathrm{HB-(i)-to-cb}}$ was applied as heat flux boundary condition on upstream, transverse and intermediate spaces that are shown in Figure B-7. However, this assumption is incorrect since in reality, there will be an order of magnitude heat loss to surroundings while the heat is transferred through any mode of heat transfer. Hence, heat applied in the intermediate spaces of the channel bottom surface is uniformly reduced i.e., by varying leakage factor (α) from 0 to 0.5 for two cases shown in table [1,2]. This method is known as error minimization principle and it provides appropriate amount of heat loss from bottom casing enclosure to surroundings based on comparison between ansys predicted and experimentally available copper channel bottom surfaces. Note that, the applied heat reduction is done keeping the heat flux in the gaps as a constant. The heat input reduction in the intermediate spaces will lead to converged temperature values. The graph below indicates that the error is minimum when α is 0.1 i.e., heat input on the copper channel bottom surface is 90% of $\sum_{i=1}^{3}\dot{Q}_{HB-(i)-to-CB}$.

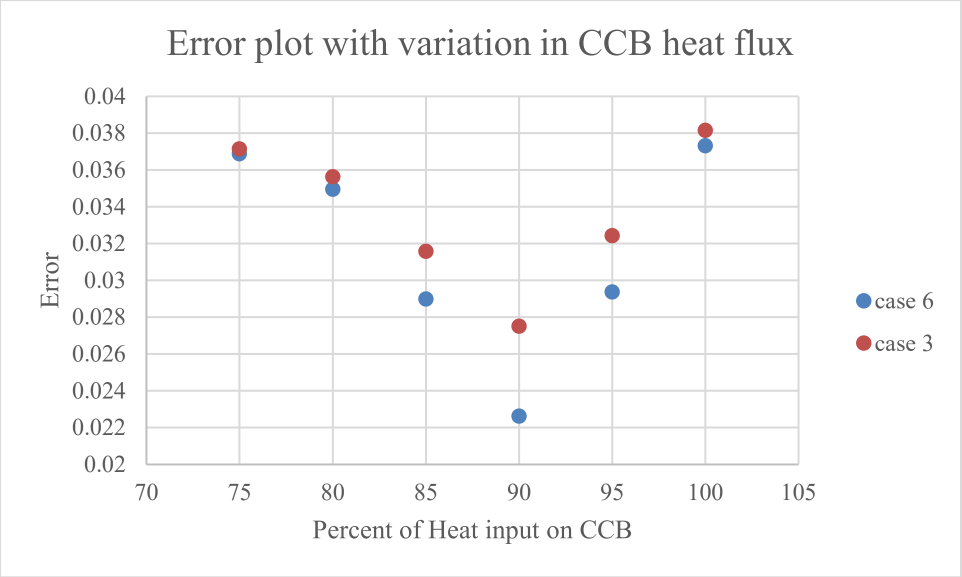

Figure B-11: Plot of error points with variation in heat input on channel bottom surface.

Formula for error calculation used above is: $\{\sum_{i=1}^{n} abs[\frac{{T_{exp(i)}}^2 - {T_{Ansys(i)}}^2}{{T_{exp(i)}}^2}]\}/n$

Where $T_{Ansys(i)}$ are the ten computationally obtained channel bottom temperatures: a_2 to f_1, two flange temperatures and twelve heater block temperatures. $T_{exp(i)}$ are the corresponding experimental temperature measurements.

Since the hypothesis is tested and proved for two cases, the rest of the cases are simulated with leakage factor (α) as 0.1 as a boundary condition on bottom casing enclosure. The error values are presented below figure B-12.

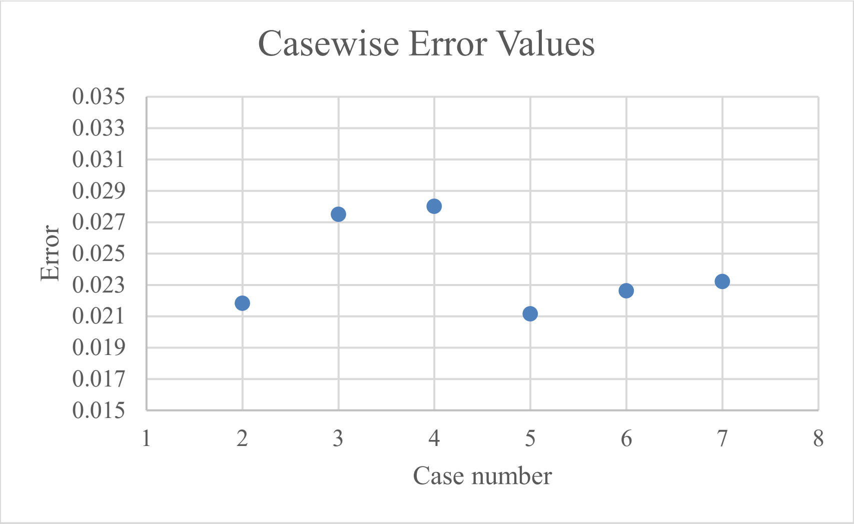

Figure B-12: Individual case error values for α as 0.1

The predicted h_x versus x plots and corresponding Nu_x versus x plots for specific case 7 of Soroush's Table-1 are shown in Figures. B-14 and 15 and for all the remaining cases are shown in Figures. 4.1. The error bars on these curves are obtained from uncertainty estimation procedures as described in experimental and simulation uncertainty section 3.4.

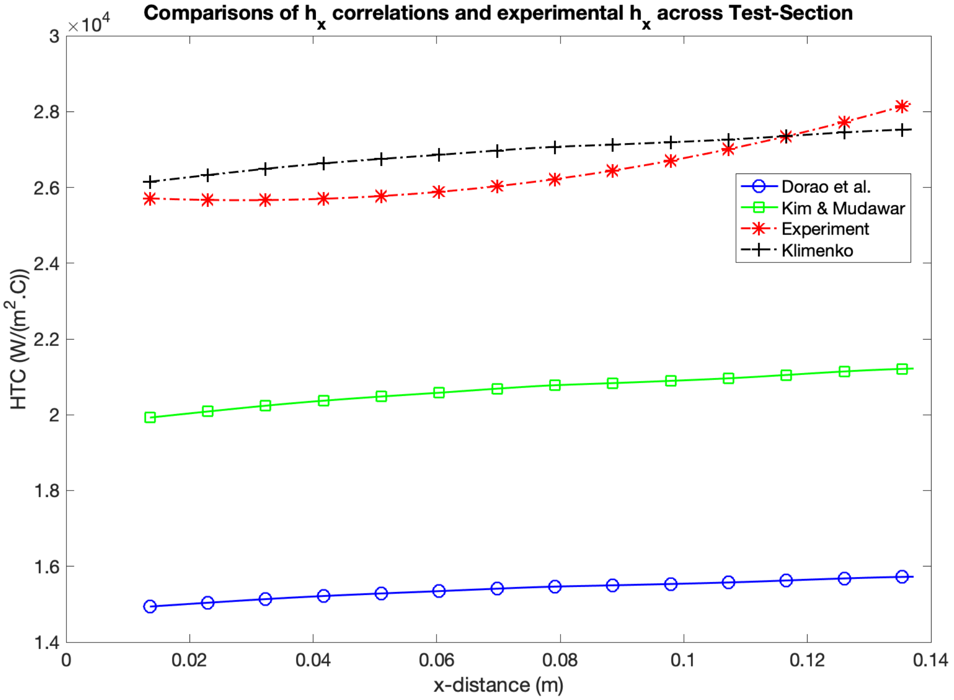

Figure B-13: Comparison of theoretical h_x correlation results with ANSYS and experimentally obtained h_x along the boiling surface.

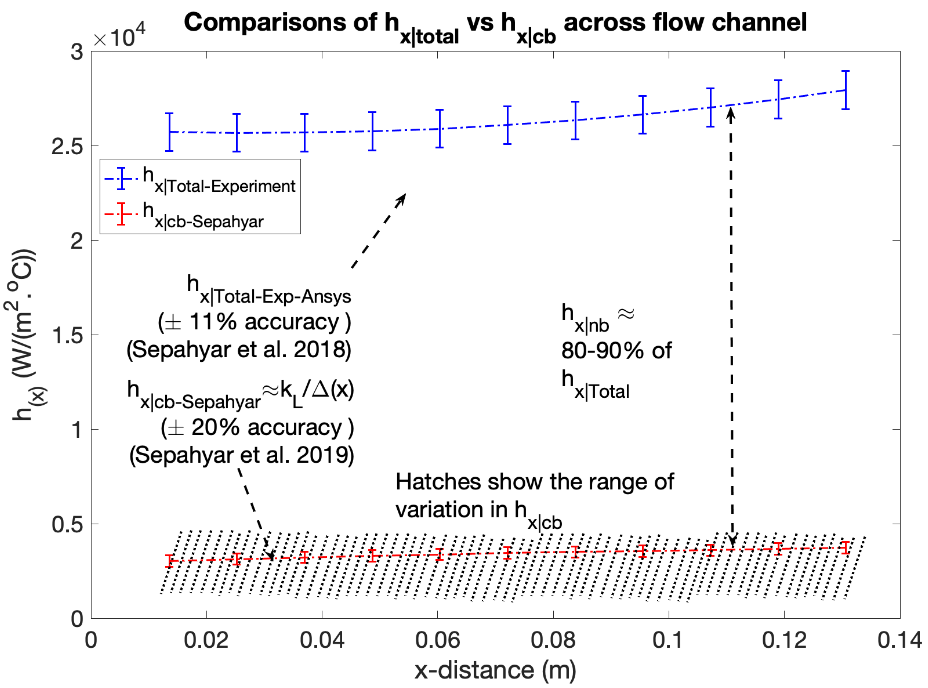

Figure B-14: Predicted h_x versus x plot with comparison between $h_{x|Total}$ versus $h_{x|cb}$ along with error bars.

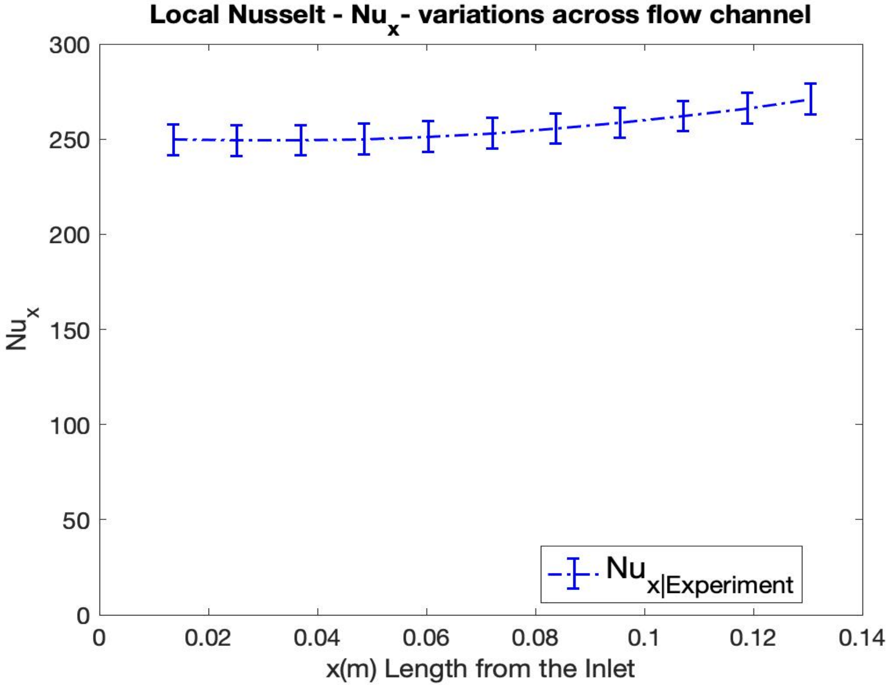

Figure B-15: Corresponding Nu_x versus x plot with calculated error bars.

C Energy Balance Comparison

In the two below tables a comparison of flow-based energy equation and net calculated energy on the boiling surface (the energy directly spent on the phase change) is indicated.

Table C-1: Comparison for Data Set 1

Case	$\dot{M}_{L_{in}}$	$\dot{M}_{V_{in}}$	$\dot{M}_{L_{out}}$	$\dot{M}_{V_{out}}$	$\bar{q}''_{W}$	$\dot{q}_{in-flow}$	$\dot{q}_{Exp-Modelling}$	% Error
Unit	[g/s]	[g/s]	[g/s]	[g/s]	[W/cm^2]	[W]	[W]	-
1	1.54	4.54	1.28	4.8	21.16	586.3	338.56	42.255%
2	1.72	4.58	1.4	4.9	32.81	720.96	524.96	27.186%
3	1.82	4.25	1.42	4.65	40	900	640	28.889%
4	2.22	3.69	1.89	4.02	42.83	742.5	685.28	7.706%
5	2.26	4.56	1.87	4.95	47.6	876.33	761.6	13.092%
6	2.47	4.36	2.06	4.77	46.96	920.86	751.36	18.407%
7	2.47	4.6	2.06	5	57.26	920.45	916.16	0.466%

Table C-2: Comparison for Data Set 2

Case	$\dot{M}_{L_{in}}$	$\dot{M}_{V_{in}}$	$\dot{M}_{L_{out}}$	$\dot{M}_{V_{out}}$	$\bar{q}''_{W}$	$\dot{q}_{in-flow}$	$\dot{q}_{Exp-Modelling}$	% Error
Unit	[g/s]	[g/s]	[g/s]	[g/s]	[W/cm^2]	[W]	[W]	-
1	1.55	2.55	1.18	2.92	32.7	832.5	503.58	39.510%
2	1.88	2.51	1.51	2.88	39.85	832.13	613.69	26.251%
3	1.91	2.66	1.5	3.07	48.88	921.68	752.752	18.328%
4	2.158	2.78	1.83	3.11	48.04	737.016	739.816	0.380%
5	2.16	2.87	1.82	3.21	53.39	763.3	822.206	7.717%
6	2.37	2.92	1.94	3.5	57.28	964.92	882.112	8.582%
7	2.35	3	1.98	3.37	65.7	829.54	1011.78	21.969%